CCLAB Composite Construction Laboratory

ÉCOLE POLYTECHNIQUE FÉDÉRALE DE LAUSANNE

Appendix C -Technical Report n° CCLab2000.1b/3

Experiments on Simple, Continuous and Bonded GFRP Beams

Julia de Castro San Román

Version: March 28th, 2005

Table of Contents

1 Introduction

1.1 Formulation of the Problem

Fiber-reinforced polymer (FRP) composites are used more and more in engineering structures thanks to their advantageous material properties such as high specific strength and insensitivity to frost and de-icing salts, and rapid component installation (Keller 2003). However, there are also some material properties that still hinder widespread acceptance of new FRP constructions by civil engineers familiar with traditional construction materials like steel or reinforced concrete. One of these disadvantages is the lack of ductility inherent to FRP materials. Ductile materials allow favorable redistribution of internal forces linked with increase in structural safety, dissipation of energy from impact or seismic actions and warning of a possible structural problem due to large deformations before failure. A second disadvantage is the difficult joining of structural FRP components caused by the brittle fibrous and anisotropic character of materials. The current practice of bolting is not material-adapted and leads, in most cases, to over-sizing of components (Keller 2003). Adhesive bonding is far more appropriate for FRP materials. The high stiffness of the relatively brittle epoxy adhesives currently used, however, leads to high shear and peeling stress peaks at bonded joint edges (Keller et al. 2004). Furthermore, the surface preparation and adhesive application process are very demanding. Simple non-destructive quality control possibilities do not yet exist. Therefore, in an engineering structure composed of FRP components and adhesive joints, the unexpected failure of a bonded joint cannot be excluded and must be considered in the structural concept.

To overcome these two drawbacks of bolted or epoxy-bonded FRP engineering structures, the author proposes a new concept for structures composed of brittle FRP components that include system ductility through the use of ductile adhesive joints and statically indeterminate structural systems. The proposed concept envisages adhesives with an initial elastic behavior sufficiently stiff to meet short and long-term serviceability requirements. When service and ultimate loads are exceeded, however, adhesive behavior should change and become plastic or at least highly nonlinear with a much lower stiffness. In the latter case, behavior is designated in the following as flexible and not ductile. Ductile or flexible joints can compensate for the lacking material ductility of FRP components by providing ductility of the structural system, called system ductility, which also offers the aforementioned advantages of ductility materials. In the case of joint failure, the redundant (statically indeterminate) system enables the development of alternative load paths and thus redistribution of section forces due to the other ductile or flexible joints. In this way, structural collapse can be prevented.

Furthermore, the elasto-plastic or highly nonlinear behavior of the adhesives hinders the occurrence of high stress peaks. Shear and peeling stresses are much more evenly distributed in the bonded surface, leading to less sensitive and more robust joints with regard to premature and unexpected failure. This concept was already introduced partially in Keller et al. (200?) to control stresses in the flanges of adhesively bonded sandwich girders.

To demonstrate the feasibility of the proposed concept of FRP structures with system ductility, experiments on continuous FRP beams with flexible adhesive joints were performed. The results of this research project are presented in this report.

1.2 Objectives

The main purpose was to investigate the mechanical behavior of GFRP continuous beams over two spans with an elasto-plastic connection in the mid-support and to compare it with traditional static systems such as the simple beam and continuous beam over three supports. The second aim was to experimentally define the full-section elastic and shear moduli of the GFRP beams. The third aim was to compare the actual experimentally-observed behavior of the new beam concept with that predicted using an analytical model based on GFRP orthotropic and adhesive properties.

1.3 Experimental Program

The experiment program consists of three beam series: a simple beam series (PS), a continuous beam over two supports series (PC) and a continuous beam with a flexible adhesive connection in the mid-support series (PH). The PH beams were built of two profiles connected with an adhesively bonded strap joint on the top and bottom flanges (Figure 1). Three different overlap lengths, 100, 200, and 300 mm, were tested in order to determine their influence on connection stiffness and consequently on beam behavior. The first two series included three specimens whereas the last series included four specimens, two of them, PH1 and PH2, being identical. Table 1 summarizes the beam series.

The bonded connection was manufactured using a soft and highly nonlinear adhesive that allows good load transfer in the joint, increasing failure load and development of large deformations compared with the commonly-used epoxy resin (de Castro 2005 b). However, its visco-elastoplastic behavior could affect the long-term behavior of the joint and therefore of the beam. For this reason, a long-term test over a week in serviceability conditions was carried out to determine the magnitude of creep deformations.

Bending experiments were carried out over 2002 and 2003 at the IS (Structural Engineering Institute) laboratory of the EPFL in Lausanne.

Table 1 Beam series

Series	Number of specimens	Static system	Overlap length l(mm)
PS	1,2,3	simple beam	-
PC	1,2,3	continuous beam	-
PH	1,2	elastoplastic hinge beam	200
	3		100
	4		300

2 Experiment Specimens

2.1 Dimensions

The beams consist of glass-fiber reinforced polymer tubular profiles with a square section. The square section is more adapted to pultruded material applications than the most commonly used I-shape section (Ashby 1991). The tubular section provides higher torsional stiffness and acts against lateral-torsional bucking of the compression flange, unlike the commonly-used I-section.

A 240x240x12 mm square tube section was chosen, the largest square tube section produced by Fiberline Composites A/S (DK). Beam dimensions are shown in Table 2, the cross-section is illustrated in Figure 1(b). The section has a nominal depth, d, of 240 mm and a nominal thickness, t, of 12 mm. The span length, L, considered was 3600 mm, i.e., the span to depth (L/d) ratio was 15. This is a lower ratio than for traditional materials like steel and reinforced concrete, which is between 20 and 30, because of the lower stiffness of GFRP composite materials.

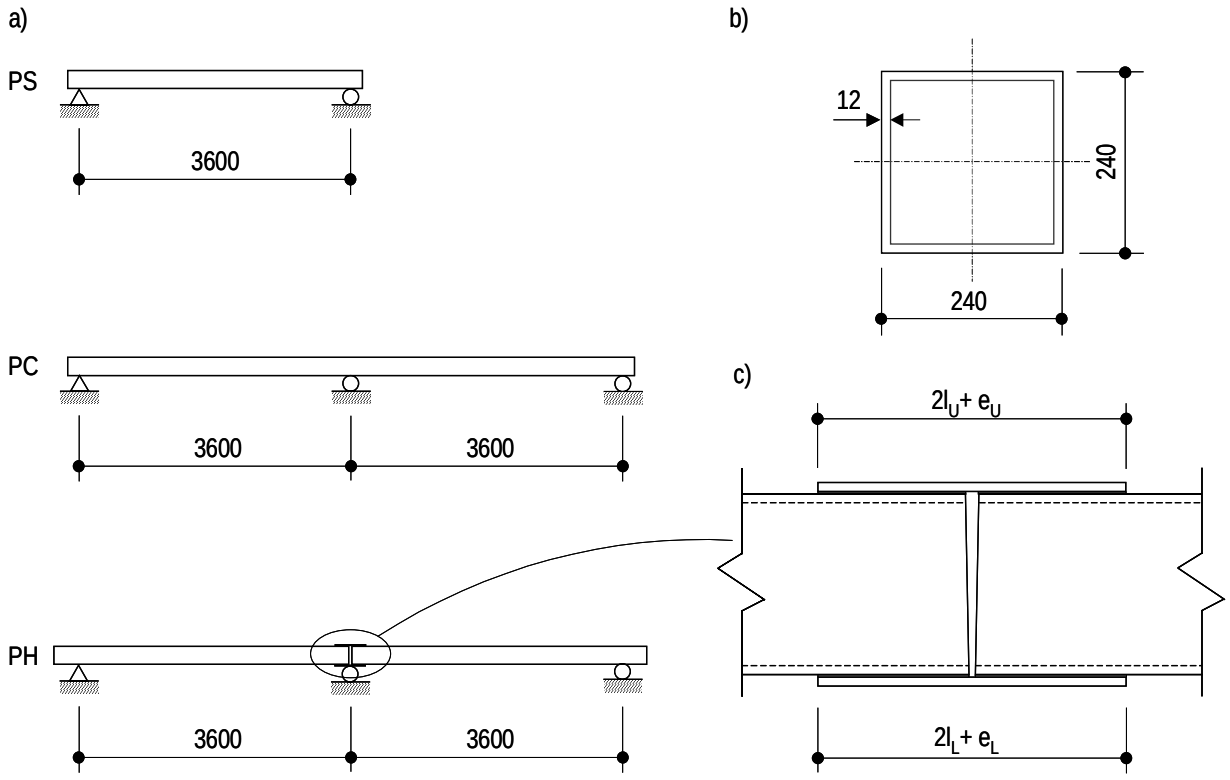

Figure 1 (a) Beam series; (b) Idealised beam section; (c) Joint detail

The width, thickness and 90° corner angle of the actual cross-section were measured at the end and middle of the profiles and corresponded with nominal dimensions. Web and flange surfaces were warped as illustrated in Figure 2; the deviation was lower than 1 mm and agrees with flatness tolerances

(Anon 1995). It probably occurred in the manufacturing process and may be due to thermal shrinkage and the differential cooling between outer and inner surfaces during curing.

The manufacturer supplied the beams of the required length. The delivered profiles were cut in the factory using a "floating" suspended saw that did not guarantee a perpendicular cut (Figure 1(c)) (Anon 2003). This did not affect beams PS1-3 and PC1-3 but modified the initial design of beams PH1-4 which had incorporated a constant gap between the two profiles.

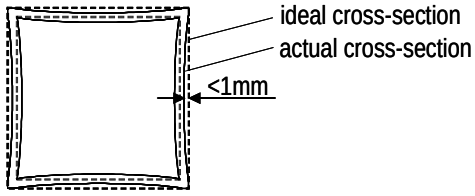

Figure 2 Flatness imperfection

Beams PH1-4 are illustrated in Figure 1(a). They were constituted from two single-span tubular 3850 mm long tubular beams, 3850 mm long, connected at mid-support at the location of maximum negative bending moment, with an adhesively-bonded strap joint on the top and bottom flanges. The bonded joints were able to transfer bending moments over the mid-support but no shear forces. Both PH1 joints were composed of two 120x12 mm laminates, whereas the upper PH2-4 joints were formed of two 120x12 mm laminates and the lower joints one 240x12 mm laminate (Figure 3). The laminates were cut from the square tubular profiles and delivered with the required width and 1000 mm length. They were cut to the desired length using a diamond circular saw in the LMR (Rock Mechanics Laboratory) of the EPFL. The strap joints had different overlap lengths, l, ranging from 100 to 300 mm, i.e., the span-to-joint length (L/l) ratio was 12 to 36. On beams PH1, PH2 and PH4, the upper and lower joint overlap lengths were the same. While on beam PH3, the bottom joint overlap length was twice as long as the upper one to avoid a likely pressure failure in the support area. As previously mentioned, the gap between the two profiles was initially designed to be constant. Because the delivered profiles were cut slantwise, however, the upper gaps, e_U, were larger than the lower gaps, e_L (Table 2). The gap must allow rotation of the two profiles without touching the bottom flanges. The choice of adhesive thickness was a compromise. A thin layer as for steel joints or traditional composite joints, 0.05-0.5 mm, is not feasible because of profile flatness tolerances. In addition, the gages placed inside the joint and their wires required a certain thickness (see 3.2.5). The adhesive thickness chosen was therefore 2 mm.

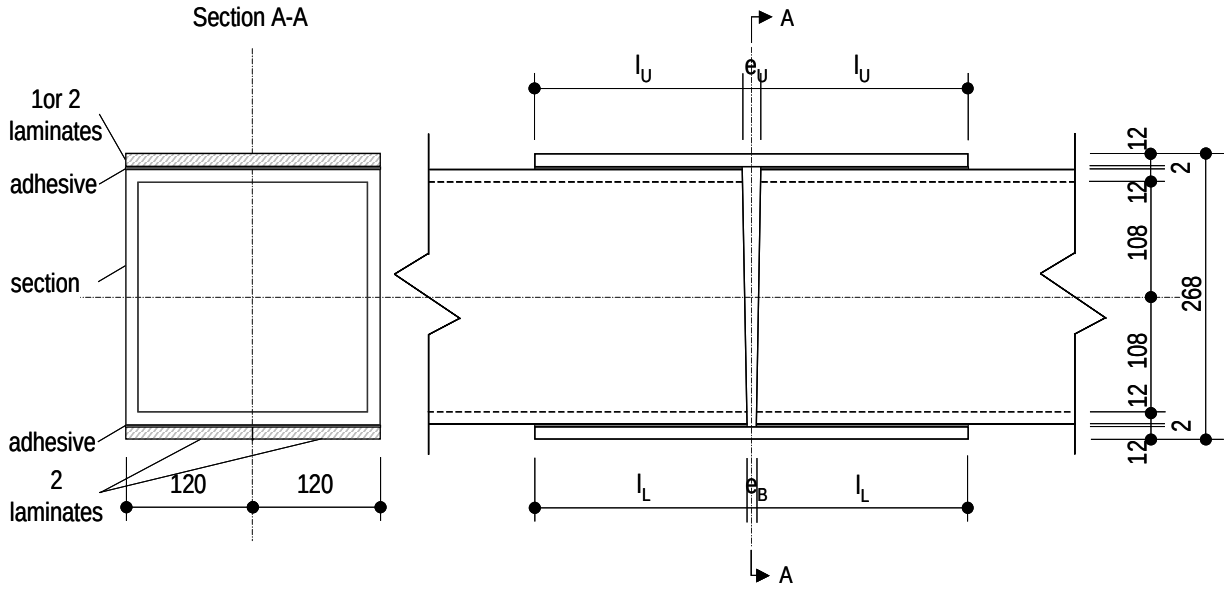

Figure 3 Adhesively-bonded connection of beams PH1-4

Table 2 Beam dimensions

Beams	Span L	Length	Upper overlap length l_U	Lower overlap length l_L	Upper gap e_U	Lower gap e_L
	[mm]	[mm]	[mm]	[mm]	[mm]	[mm]
PS1-3	3600	3900	-	-	-	-
PC1-3	2x3600	7500	-	-	-	-
PH1	2x3600	7700	196	200	16	8
PH2	2x3600	7700	195	199	18	10
PH3	2x3600	7700	100	198	20	12
PH4	2x3600	7700	300	304	18	10

2.2 Materials

2.2.1 GFRP Beams and Laminates

The beams and laminates used in this investigation were pultruded glass-fiber reinforced polymers (GFRP) manufactured by Fiberline Composites A/S (DK), using E-glass G666P and an isophtalic polyester P4506.

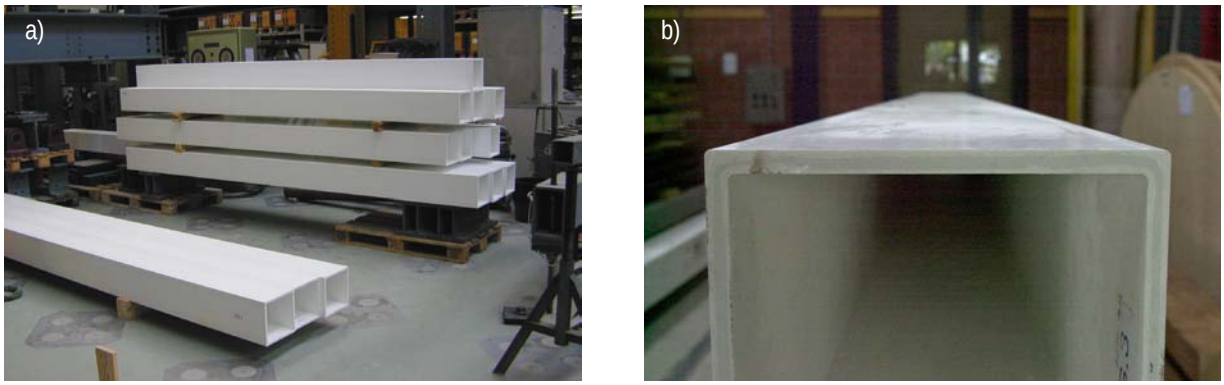

Figure 4 GFRP square tubular beams (a) global view, (b) cross-section

Structural profiles are composed of a succession of layers of (Figure 5):

- roving mix;
- mat/weave;
- surface veil.

The roving mix layer consists of a combination of unidirectional fibers in the longitudinal direction (the *x* direction) which is the profile's main loading direction. It provides the longitudinal strength. It contains a ratio of 4:1 of straight to blown glass fibers. The mat/weave reinforcement provides a shear resistance and contributes to improve bolt bearing capacity and transversal bearing strength (Anon 2003). It consists of a combination of chopped strand mat (CSM) and woven glass mat (0°/90°) stitched together with a special process where hundred of needles are punched through the two mats. The needles have small hooks that push filaments from one mat to the other hereby combining them (Anders Korsgaard explanation from Fiberline Composites S/A (DK)). The thin polyester surface veil (40 g/mm^2) was added on the outside to provide protection to the fiber reinforcement against ultra-violet degradation and corrosive attacks.

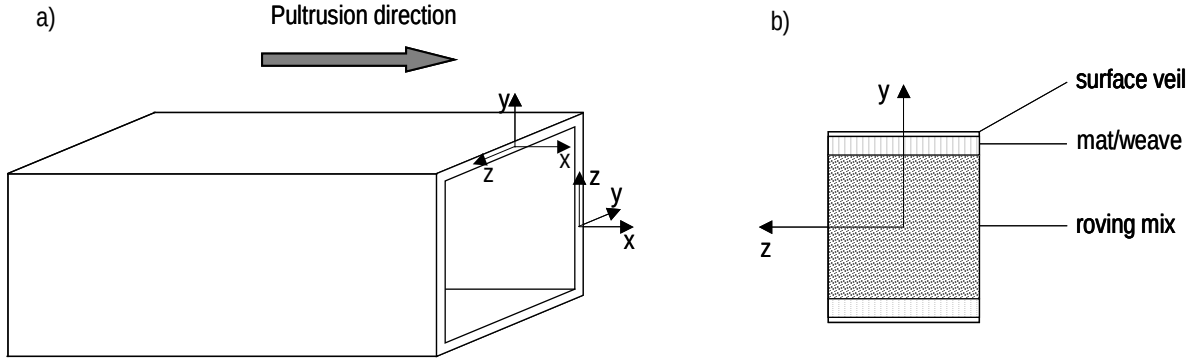

Figure 5 (a) Local axis; (b) Diagram of beam fiber architecture (not to scale)

A resin burn-off in a furnace at 450° was conducted to define the fiber architecture and fiber fractions listed in Table 3. Figure 6 shows the succession of the five layers. The ends of the overlaps of the combined mats were visible on the outer and inner surfaces at approximately 30 mm from the section edges. The fiber fractions were determined by weighing the specimen before and after resin burn-off. The volume fractions were calculated using an E-glass density of 2.56 g/cm^3 (value given by the supplier). Calculations assumed there were no internal voids, which was confirmed by investigation using a microscope of cross-sections of similar profiles delivered by the same supplier (Tirelli 2003). The analysis showed very good fiber embedment without any voids.

Table 3 Fiber architecture and fractions by volume and weight of GFRP profiles (see Figure 6)

	Reinforcement	Architecture	% by vol.	% by weight
A	Rovings (UD)	4:1 straight and blown	30	42
B	2 Combined mats:	600	15	21
	- CSM [g/m^2]	300		
	- woven 0°/90°	150/150		
C	2 Combined mats:	1050		
	- CSM [g/m^2]	450		
	- woven 0°/90°	300/300		
	Total		45	63

Profiles are manufactured by pultrusion (Figure 7), an automated process for the production of straight or curved profiles with constant section and high fiber content. The fibers are pulled through a heated die at a specific temperature and speed, where they are impregnated with the resin. The resin is then polymerized and the composite cured in the final profile geometry. Lastly, profiles are cut into the desired lengths with a "floating" suspended saw. This pultrusion process guarantees constant quality.

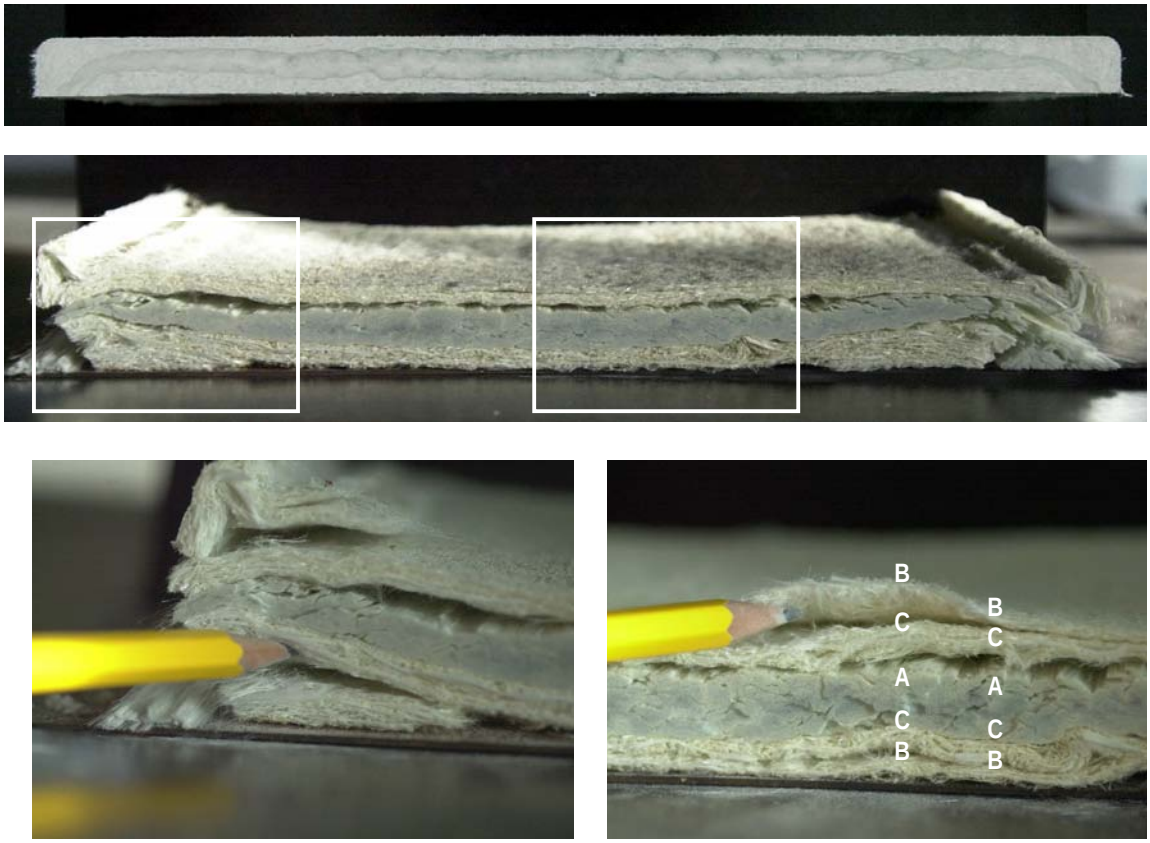

Figure 6 Fiber architecture of a 240x240x12 mm profile section after a resin burn-off test

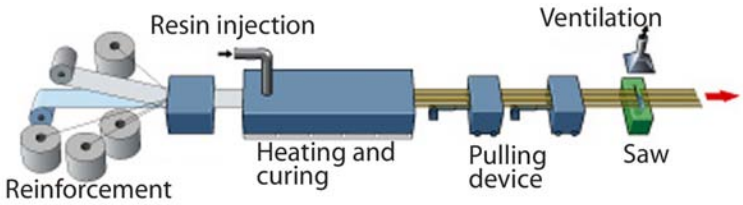

*Figure 7 Pultrusion process (*http://www.fiberline.com*)*

Profiles exhibit orthotropic behavior due to their different fiber architecture in the longitudinal, transversal and in-thickness directions. Their stiffness matrix is characterized by nine elastic coefficients, only five of which are available in the pultruder's design manual (Table 4).

Table 4 GFRP material properties from the pultruder's design manual (Anon 2003)

E_x [MPa]	E_z [MPa]	G [MPa]	ν_{xz} [-]	ν_{zx} [-]
23000	8500	3000	0.23	0.09

2.2.2 Adhesive

The adhesive used in this experimental study was the acrylic-based two-component SikaFast 5221 structural adhesive, based on ADP (Acrylic Double Performance) technology, developed by SIKA AG. ADP technology offers a new generation of fast-curing elastic adhesives designed to substitute welding and mechanical-fastening techniques. The adhesive choice was based on preceding experiments on bonded GFRP double-lap joints using epoxy, polyurethane and acrylic adhesives (de Castro 2005 a). It is a highly nonlinear and flexible adhesive allowing good load transfer in joints, increasing failure load and development of large deformations. The SikaFast 5221 adhesive is designated ADP adhesive in this experimental report.

Figure 8 ADP (SikaFast 5221) in a cartridge (250 ml), used for small series, and the appropriate static mixer tube

The following table presents some technical data; more information is available at www.sika.ch.

Table 5 ADP adhesive technical characteristics

Technical characteristics	ADP (SikaFast 5221)
Chemical base	two-component ADP technology adhesive
Supplier	Sika
Glass transition temperature T_g[1]	50 °C (+23°C, 1 day cured)
Consistency	thixotropic
Cure	ambient temperature
Working time [2]	9 min at +23°C
Application temperature (environment and supports)	+10°C to +40°C
Surface treatment	sanding and degreasing applying of activator and primer

[1] supplier data
[2] period after mixture of components during which joint must be assembled, similar to open time

To determine the mechanical properties of adhesives, different tests were carried out in collaboration with the adhesive supplier and partner, SIKA AG. The adhesive test program consists of a series of 4-5 test specimens per adhesive type:

- tensile tests in accordance with EN ISO 527-2 (1996), quasi-static, destructive testing;
- compressive tests in accordance with ASTM D 695-96 (1996), quasi-static, destructive testing;
- shear napkin-ring tests designed at the EMPA (Schmid and Kieslbach 2001), based on the former EN ISO 11003-1, destructive testing;

The compression and tensile tests were carried out on bulk specimens on August 30, 2001 in the laboratory of SIKA AG, Zurich, Switzerland. Results are summarized in report CCLab2000.1b/1 (de Castro 2005 a). Figure 9 illustrates the shear stress-strain curve that can be describe as bilinear, with two different shear moduli G_1 and G_2, whereby G_2 is approximately 11 times lower than G_1. The resulting adhesive properties are listed in Table 6, where τ_u is the shear strength and γ_u the shear strain at failure.

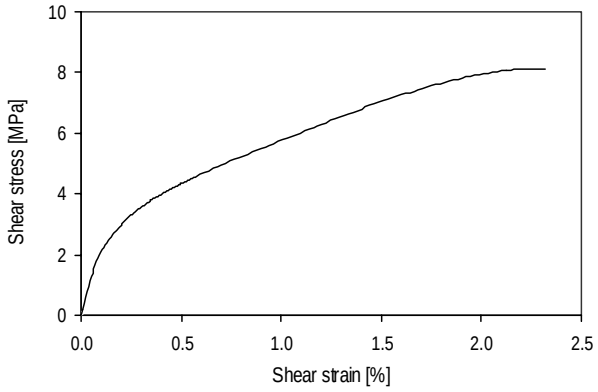

Figure 9 ADP adhesive shear stress-strain behavior

Table 6 ADP adhesive shear properties

τ_u [MPa]	γ_u [%]	G_1 [MPa]	G_2 [MPa]
8.9	2.3	0.033	0.003

2.3 Manufacture and Quality Control

2.3.1 Manufacture

The PH beams are made of two simple beams connected on the top and bottom flanges with two strap joints. The joints were manufactured in three main stages:

- surface treatment;
- bonding;
- cure.

The joint's resistance and durability depend on the adhesive and surface treatment. Surface treatment eliminates the layers of greases and release agents as well as low-cohesion layers (dust, oxides) and improves anchorage between adhesive and adherends by increasing the latter's roughness. In this study, surface treatment of the GFRP beams and laminates started with degreasing, sanding and cleaning the future bonded area (Figure 10). Isopropanol or acetone solvents compatible with the polyester, the composite material resin, were used to degrease surfaces. A Bosch GDA280E sander with 80-grit abrasive paper was used to remove the polyester and surface veil until the mat appeared at a depth of approximately 0.1 mm. This mechanical treatment was applied until the shiny surface disappeared, taking care not to damage the first fiber layer. The bonded areas were degreased again with the solvent to remove deposited abrasive particles. The ADP adhesive required the application of two additional products: an activator and primer number 215 from SIKA (AG) (de Castro 2005 b). They were applied according to the supplier's (SIKA AG) specifications.

Figure 10 Surface treatment (a) sanding and (b) degreasing

Bonding was prepared according to the supplier's specifications. The two components were mixed using the appropriate static mixer tube. The uncured adhesive was then spread on the beam. Four glass balls of 2 mm diameter were placed on each bonding area to guarantee the adequate adhesive layer thickness. The laminates were then laid and pressed. Their position was verified with a rule and their horizontality with a water level. Bonding time was restricted because of the ADP adhesive's short open time, 9 min at 23°. Due to the large areas to be bonded and high ambient temperature, 26±2° during PH2-4 manufacture, the bonding process was accelerated. Figure 11 illustrates some of the bonding steps.

Weights were placed to produce pressure during curing time. After one day of cure, the beam was delicately turned over and the second laminates were bonded following the same process. The beams were cured under ambient laboratory conditions, nine weeks at 22±2° for PH1 and five weeks at 26±2° for PH2-4. The initial planned curing time for PH1 was also five weeks, but since the set-up was not available, the cure was longer. This could not have affected joint behavior as the adhesive had reached its maximum stiffness before the five weeks originally planned between manufacturing process and test.

Figure 11 Bonding process (a) adhesive application, (b) glass ball positioning, (c)horizontality check, (d) weight application

Figure 12 Adhesively-bonded connection of beam PH2

2.3.2 Quality Control

Several quality checks were performed during joint manufacture and before testing to obtain constant performances and improved reliability. These checks complied with the Quality Assurance in Adhesive Technology (1998) resulting from the EUREKA Project EU716. This document presents control tools and techniques to fulfill established joint requirements. As suggested, a specific checklist document was developed describing all joint manufacturing steps (Siebrecht and Vallée 2001).

During the manufacturing process it was crucial to verify:

- adhesive: the product's conformity, storage conditions, open time, mixture reactivity, viscosity;
- activator and primer: the product's conformity, storage conditions, open time, dry time and thickness;
- surface: moisture and ambient temperature, operation times, solvent.

After bonding, final inspections must be performed using non-destructive testing techniques to identify any joint defects. Information concerning defect types, their causes and adequate control techniques for their detection are presented in report CCLab2000.1b/2 (de Castro 2005 b). Porosity and voids could be detected by basic visual and sound inspections and/or by advanced and expensive testing techniques commonly called non-destructive evaluating (NDE) techniques. In this experimental study, the final inspection consists of basic controls constituting visual and acoustic examination. Visual inspection consisted of the examination of adhesive surround. Sound inspection consisted of tapping the bonded area with a rule. These basic inspections are fast and economical techniques but they are also limited and subjective.

After testing, a visual inspection of failed specimens must be carried out in order to check the presence of defects. Only beam PH3 failed in the adhesively-bonded connection. No defects (porosity and voids) were detected in the adhesive layer but bad adhesion areas were observed (Figure 66(a)), indicating premature joint failure.

3 Experimental Procedure

3.1 Test Set-up and Loading Equipment

Beams were simply supported on rollers with a span length of 3.6 m and subjected to bending tests via one or two hydraulic jacks with a capacity of 500 kN per jack and maximum displacement of 300 mm. Beams PS1-3 were first subjected to a four-point bending test to determine beam properties and then to a three-point bending test. During three-point bending experiments the simple beams PS1-3 were loaded at the third point from one edge, 1.2 m, and during four-point bending experiments, at the third points from each edge as shown in Figures 13(a) and (b). Beams PC1-3 and PH1-4 were loaded at the third points from the mid-support, 1.2m, as shown in Figures 13(c) and (d) respectively. The PS2 experiment set-up is illustrated in Figure 15 and the PH2 experimental set-up in Figure 16. Load-application points were determined in such a way that, for the continuous beam configuration, the ratio of the maximum negative moment to the support, M^-, divided by the maximum positive moment in the span, M^+, was maximal in order to clearly demonstrate the effect of the flexible joints in the bonded beams. On the other hand, this ratio was chosen as being close to the ratio of the uniform load distribution, which is $M^-/M^+=1.79$ (integrating bending deformations and ignoring shear deformations). Given these considerations, a load application point at one third of the span on the support side of each span resulted in a ratio of $M^-/M^+=1.88$ (ignoring shear deformations).

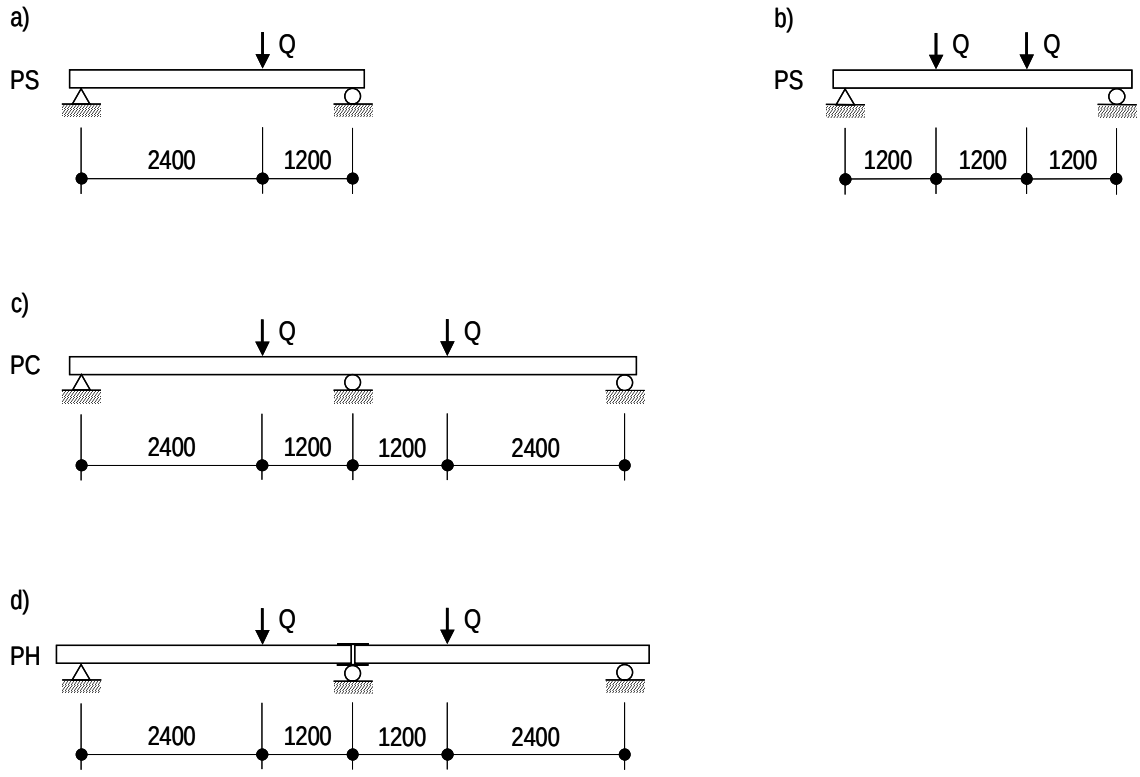

Figure 13 Loading locations

In order to assure uniform load transfer from jacks to beam, a wood plate and neoprene layer were installed between them. Wood plates were 27 mm thick, 260 mm wide and 300 mm long. Neoprene layers were 5 mm thick and had the same width and length as the wood plates. The concentrated loads were applied in a 300x240 mm area.

Details of the support layout are shown in Figure 14. The simple supports were provided using steel rollers between steel plates. These plates were 120 mm wide and 200 mm long and connected to larger steel bearing plates to prevent bearing failure. Bearing plates were 15 mm thick, 300 mm wide and 400 mm long. For the same reasons as for loading sections, 27 mm thick wood plates were installed between beam and supports. On beams PH1-4 an additional 14 mm thick wood plate was installed at the end supports to compensate for the greater depth in the mid-support section. A neoprene layer was added on beams PC2-3 and PH1-4 to assure uniform supporting pressure because of the failure in the mid-support of PC1. In addition, the edges of the wood plates in the mid-support were slightly chamfered with a 10 mm radius to further reduce stress concentrations. In the first beams tested (PS1-3 and PC1) beams were connected to supports to prevent lateral displacements. Bearing plates were loosely bolted together in such a way that simple support conditions were maintained (Figure 15). This layout seemed unnecessary and was therefore not used for the following beams.

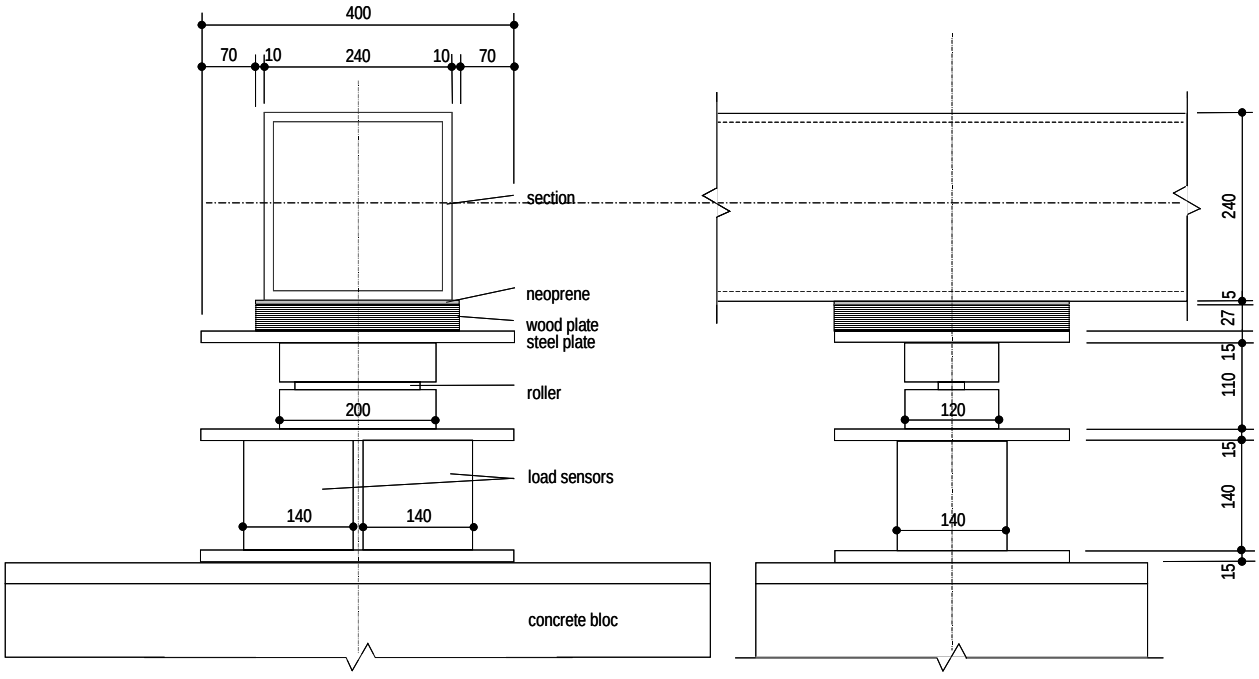

Figure 14 Mid-support

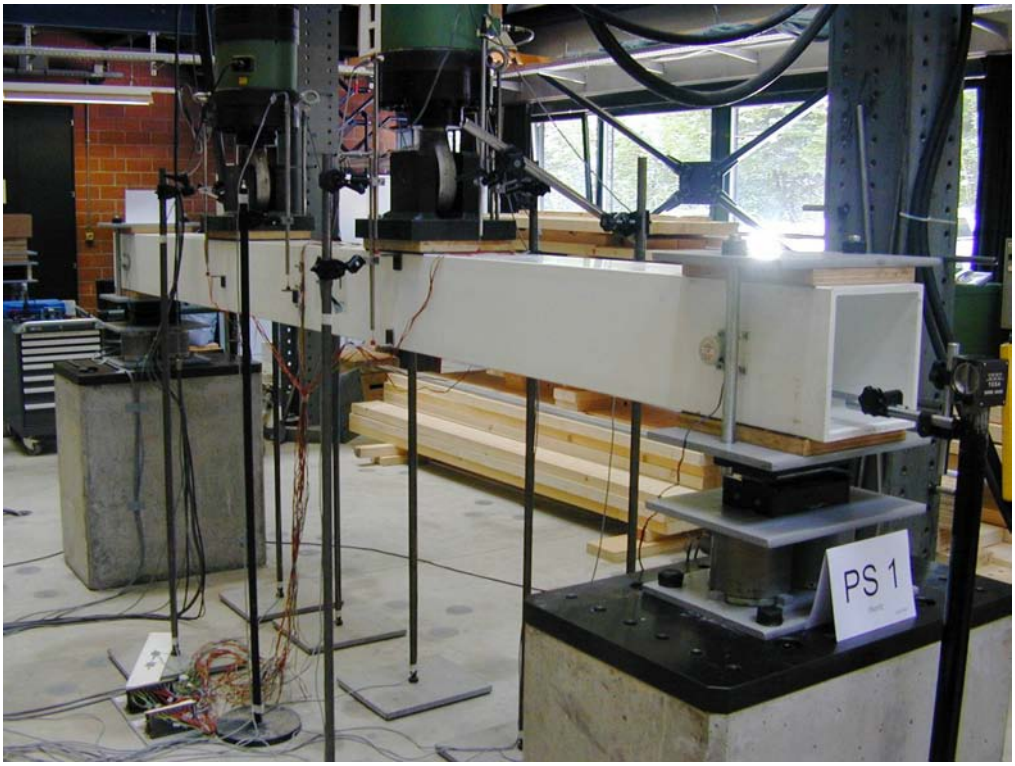

Figure 15 Four-point set-up of beam PS1

Figure 16 Set-up of beam PH2

3.2 Instrumentation and Measurements

All experiments except the creep experiment were performed with automatic measurements every 2-3 s. The data-acquisition unit was an HBM UPM 60 with 60 channels for beams PS1-3 and PC1 and an HBM UPM 100 with 100 channels for beams PC2-3 and PH1-4 (Hottinger Baldwin Messtechnik GmbH, Darmstadt, D). A data-acquisition program was developed in LABVIEW programming language for this experimental study. This program allowed the test evolution to be followed and data acquisition to be verified on different graphs. The recorded data were:

- load and displacement of each jack with a load and a displacement cell;
- force at each support with load sensors;
- displacement at several sections with displacement transducers;
- rotation of two sections close to the supports with electronic clinometers;
- axial strain of some profile sections measured with strain gages;
- axial strain of bonding overlap measured with strain gages (for beams PH1-4).

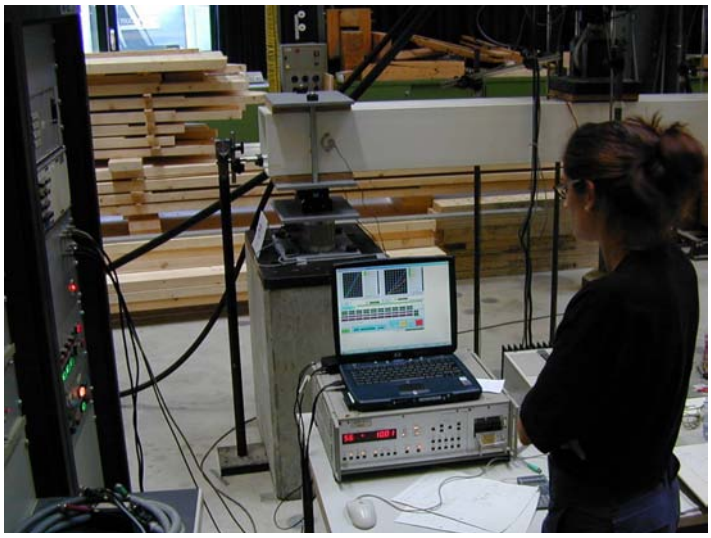

Figure 17 Data acquisition unit

3.2.1 Load Sensors

Four load sensors were used to measure distribution of supporting reactions along the two edge supports of beams PS1-3 while beams PC1-3 and PH1-4 had six load sensors at the edge and mid-supports (Figure 18). This instrumentation was not really useful for the isostatic beams PS1-3 but it was necessary for the statically indeterminate beams PC1-3 and PH1-4 to determine the bending moment diagram. Their designations and locations are indicated in the Appendix. A pair of sensors was installed under each roller support on the support axis. Comparison of East and West load sensors indicated asymmetry of the beam or loading. But because a beam is still stabilized when supported by at least three points, a greater

number of points could lead to different measurements on East and West load sensors. The average of East and West measurements will be considered the global support reaction.

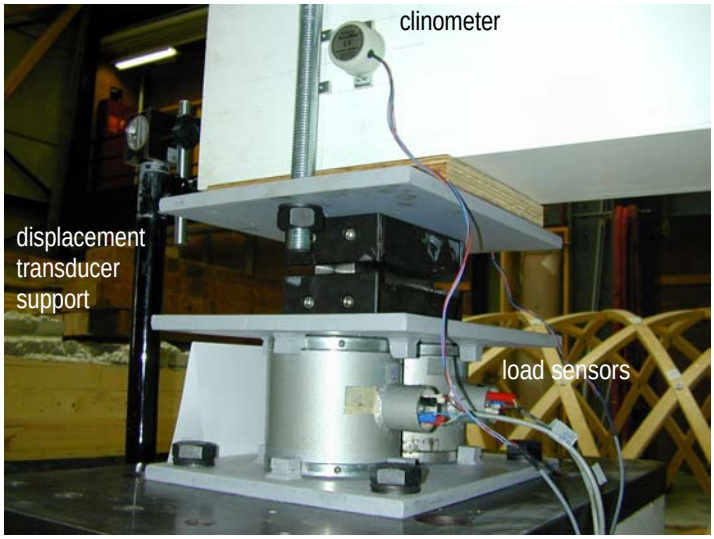

Figure 18 Support instrumentation, beams PS1-3 and PC1-3

3.2.2 Displacement Transducers

Displacement transducers were used to measure vertical displacement in the span, vertical settling displacement on support sections and horizontal displacement at the end of the beams. Labeling and location of displacement transducers are indicated in the Appendix.

Displacement transducers used in the span were mainly placed on the centerline of both webs to measure vertical displacements at the mid-span and third points. On beam PS1, two displacement transducers were placed at the loading location in the three-point bending experiment to identify local buckling and additional ones were placed at 200 mm from the loading axis on the top flange. On beams PS2-3 and PC1, further transducers were placed in the centerline of the bottom flange at the mid-span and third points for redundancy and consistency reasons.

Displacement transducers used on the edge support were placed inside the profile, on the centerline of the bottom flange, whereas the two transducers used on the mid-support were placed on the top flange at 20 mm from both edges. They were placed close to profile corners so that they were less influenced by local buckling deformation. Mechanical transducers were used on beams PS1-3 and PC1.

Comparison of East and West measurements revealed any load eccentricity and comparison of the two span measurements revealed structural symmetry. The average of East and West measurements will be considered the axial displacement.

Two displacement transducers were placed at each end of beams PC2-3 and PH1-4 to measure horizontal displacements at the ends and thus estimate rotation at edge supports. The measurements were not satisfactory because the ends moved in horizontal and vertical directions. They are not presented in this report.

3.2.3 Clinometers

Four electronic clinometers were installed to record the end rotations of beams PS1-3 and PC1-3 and the mid-support rotation of beams PH1-4. Their designation and location are indicated in the Appendix. For practical and consistency reasons, they were positioned on the centerline of the web at 50 mm from the support axis on each side of the beam (Figure 18). Comparison of East and West clinometers indicated asymmetry of the beam or loading eccentricity. The average of the East and West measurements will be considered the section rotation.

3.2.4 Strain Gages on Profile Sections

IIn order to measure strains at different locations, two kinds of axial strain gages were installed on the beams, the 6/120LY13 and 1.5/120LY13 produced by Hottinger Baldwin Messtechnik GmbH (Darmstadt, D). Connecting areas were degreased and gage locations were precisely defined and marked before gages were attached with the appropriate adhesive.

Twenty 6/120LY13 gages were installed on each beam. The 6/120LY13 has a 6mmx2.8mm measuring grid, a 13mmx6mm measuring grid carrier and an electric resistance of 120 **Ω**. These twenty gages are referred to as "profile gages". Their designation and position are indicated in the Appendix. The gages were placed in different locations on the PS beams, whereas their positions were similar for beams PC1-3 and PH1-4.

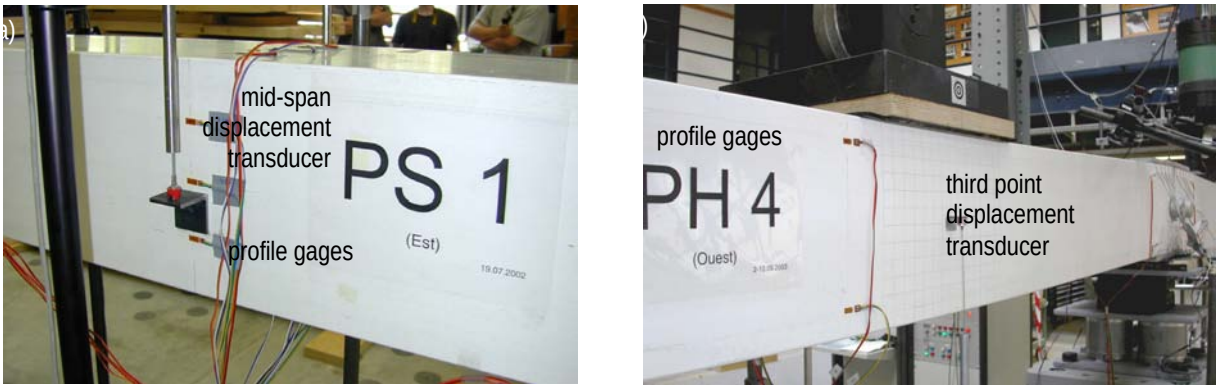

Figure 19 (a) Mid-span section of beam PS1; (b) Loading section of beam PH4

For beams PS1-3, gages were placed to measure axial strains in the longitudinal direction and the 45° direction. They were mounted in one, two or three of these sections: the mid-span section and the sections located at 200 mm from third points, depending on the beam. Therefore gages were not affected by stress concentration around load-application points. The longitudinal gages on both webs were used to measure axial strain distribution along the height of the section and to find the actual neutral axis as it usually differs from the centerline, due to the non-homogenous material (Nagaraj and GangaRao 1994).

The longitudinal gages on the flanges were used to measure axial strain distribution across the width in order to check uniform distribution or shear lag caused by shear deformations. Longitudinal gages were also used to find the longitudinal elastic modulus. Two gages were used on beams PS2,3 to measure strain at 45° in order to find the shear modulus. These gages were placed in the centerline of the mid-span section where shear stain and stress reach maximum values.

On beams PC1-3 and PH1-4, gages were installed in four sections: two per span, and on both webs. They were placed to measure axial strains in the longitudinal direction at 200 mm from the mid-support axis and 200 mm from the loading axis for the same reason as previously explained. Most gages were at 30 mm from the edge and several of them were at 60 mm in the compression area to identify the onset of local buckling. The axial strains indicated the bending moment in defined sections and thus the bending moment diagram.

Comparison of East and West measurements revealed any load eccentricity and comparison of the two span measurements revealed structural symmetry. The average of the East and West measurements will be considered the axial strain.

3.2.5 Stain Gages on Bonding Overlap

Forty 1.5/120LY13 gages were installed on each adhesively bonded connection of beams PH1-4. The 1.5/120LY13 has a 1.5mmx1.2mm measuring grid, a 6.5mmx4.7mm measuring grid carrier and an electric resistance of 120 Ω . These gages are referred to as "joint gages" because they were placed on the joint bonded area.

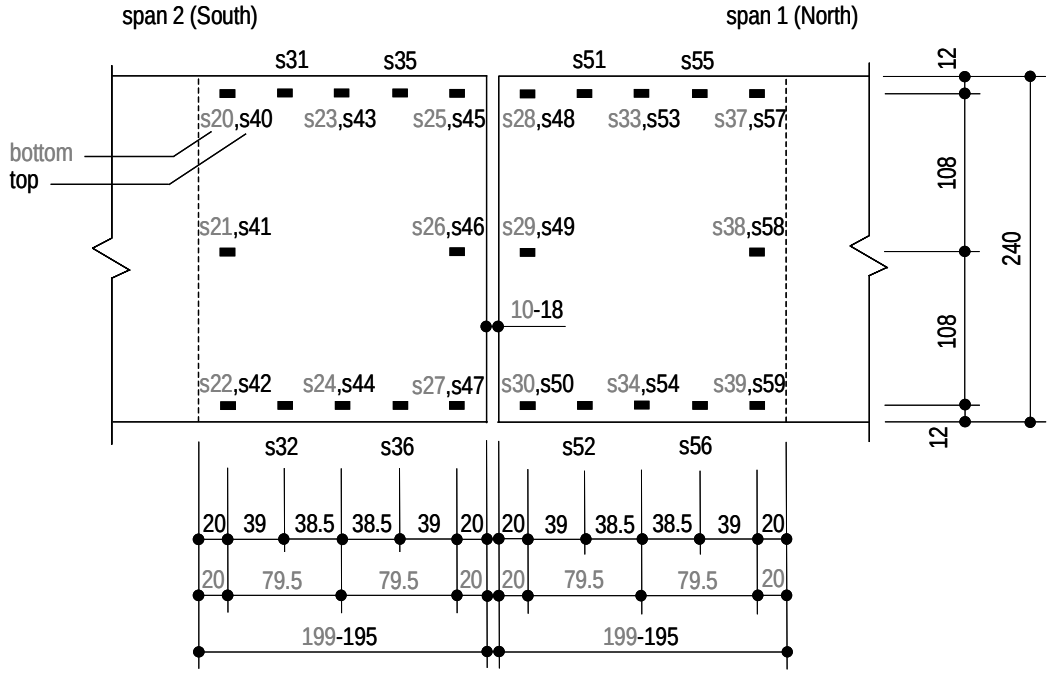

Figure 20 Gage locations on beam PH2

These gages were attached to the top and bottom flanges of the two tubular profiles at different locations, depending on the beam (Figure 21(a)). Figure 20 illustrates their designation and location on beam PH2. For other beams, gages designations and positions are indicated in the Appendix. Except for PH1, which had twenty gages in the upper and lower joints, twenty-four gages were installed in the tensile joint, i.e. the upper joint, and sixteen in the compressive joint, i.e. the lower joint. Gages were arranged on three or five sections along the overlap length and on three lines along the beam width. On beam PH3, due to the small overlap length, gages close to the edge were out of line. The gages placed on different sections were used to measure axial strain distribution along the overlap length where the load transfers from beam to laminates. Gages placed on the three lines, i.e. in the middle of the width and close to the edge, revealed the 2- or 3-dimensional effect of the joint. The East and West strain measurements revealed any loading eccentricity in direction y.

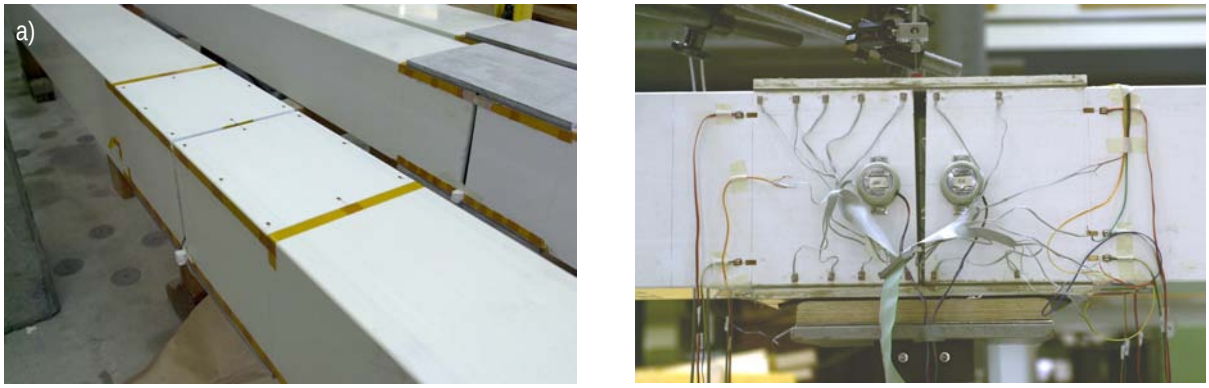

Figure 21 (a) Gage locations on the lower joint of beam PH2; (b) Mid-support instrumentation during experiments on beam PH1

Table 7 lists the beams instrumentation and Table 8 summarizes the instrumentation accuracy and the number of measurements per instrumentation category.

Table 7 Beam instrumentation

Beams	Load sensors	Displacement	Clinometers	Profile gage number	Joint gage number
PS1-3	4	12,10,10	4	20 (s0-19)	-
PC1-3	6	17, 16,16	4	20 (s0-19)	-
PH1-4	6	16	4	20 (s0-19)	40 (s20-s59)

Table 8 Measurements and accuracy

	Instruments	Number of measurements	Measurement range	Accuracy
Load	load cell of jacks	1 (PS) / 2 (PC, PH)	± 500 kN	± 1 %
	load sensors	4 (PS) / 6(PC, PH)	± 1000 kN	± 1 %
Displacement	displacement cell of jacks	1/2	± 250 mm	± 1 %
	displacement transducers (vertical direction, span)	8/9/15/12	± 100 mm	± 1 %
	(vertical direction, mid-support)	0/2	± 10 mm	± 1 %
	(vertical direction, edge supports)	0/2	± 5 mm	± 1 %
	manual displacement transducers (vertical direction, edge supports)	0/2	± 250 mm	± 1 %
Rotations	Accustar clinometer	4	±60°	± 1 ‰
	displacement transducers (horizontal direction, edge supports)	0/4	± 10 mm ± 20 mm	± 1 %
Strain	6/120LY13 HBM gages	20	± 5 %	± 2μm
	1.5/120LY13 HBM gages	0/40	± 5 %	± 2μm

3.3 Loading Program

Table 9 gives an overview of all experiments carried out. For each beam, it includes the type of experiment (three or four-point bending for simple beams and five-point bending for the others), type of loading (cycle, creep, failure), applied force for each cycle or creep experiment, type of loading (load- or displacement-controlled) and loading rate.

In the first phase, each beam was subjected to several loading cycles at different load levels to observe beam behavior and check that instrumentation was operating correctly. Cycles were mostly performed load-controlled at a rate of 0.5 kN/min. For beams PS1-3, each cycle included a 1 min plateau after loading and a 5 to 10 min plateau after unloading. For beams PC1-3 and PH1-4, each cycle included a 5 min plateau after loading and unloading. For beams PH1-4, maximum load levels corresponded to the first cracking sound, when loading was stopped to identify any permanent large deformation. In the second phase, beams were loaded up to failure, under displacement-control at 2.3 mm/min (PS1-3), 1.2 mm/min (PC1-3) and 1.5 mm/min (PH1-4). Displacement-controlled rates corresponded to the load-controlled rates of the first phase.

With regard to the very flexible adhesive used, a 7-day creep experiment was performed on beam PH2 between the cycle and loading-up-to failure phase. The applied load was 40 kN per loading point, corresponding to an immediate mid-span deflection-to-span ratio of 1/400. This ratio is in the order of magnitude of admissible deflection ratios at serviceability limit state (e.g. according to Eurocode).

Figures 22 and 23 show the loading procedure for beams PS2 and PH2 respectively.

Table 9 Overview over the performed experiments

Beam	Type of bending	Type of experiment	Force (kN)	Loading	Rate
PS1	four-point bending	cycles	5,10,20, 40,50	load-controlled	5 kN/min
	three-point bending	failure	-	displacement-controlled	2.3 mm/min
PS2	four-point bending	cycles	5,10,20, 40,50	load-controlled	5 kN/min
	three-point bending	failure	-	displacement-controlled	2.3 mm/min
PS3	four-point bending	cycles	5,10,20,50	load-controlled	5 kN/min
	three-point bending	cycles	112 (1) (first crack)	displacement-controlled	2.3 mm/min
	three-point bending	failure	-	displacement-controlled	2.3 mm/min
PC1	concentrated load per span	cycles	5,10,20,50,100	load-controlled	5 kN/min
		failure	-	displacement-controlled	1.2 mm/min
PC2	concentrated load per span	cycles	5,10,20,50, 100	load-controlled	5 kN/min
		failure	-	displacement-controlled	1.2 mm/min
PC3	concentrated load per span	cycles	5,10,20,50,100	load-controlled	5 kN/min
		failure	-	displacement-controlled	1.2 mm/min
PH1	concentrated load per span	cycles	5,10,20,40,50, 80,100	load-controlled	5 kN/min
		failure	-	displacement-controlled	1.5 mm/min
PH2	concentrated load per span	cycles	5,10,20, 50, 80,100	load-controlled	5 kN/min
		creep	40 (2)	load-controlled	5 kN/min
		cycles	100,130	load-controlled	5 kN/min
		failure	-	displacement-controlled	1.5 mm/min
PH3	concentrated load per span	cycles	5,10,20,40,50, 80,120	load-controlled	5 kN/min
		failure	-	displacement-controlled	1.5 mm/min
PH4	concentrated load per span	cycles	5,10,20,50,80, 120,150	load-controlled	5 kN/min
		failure	-	displacement-controlled	1.5mm/min

The beams were tested in a laboratory environment at 22°C (PS1-3, PC2-3 and PH1), 26°C (PC1) and 28°C (PH2-4).

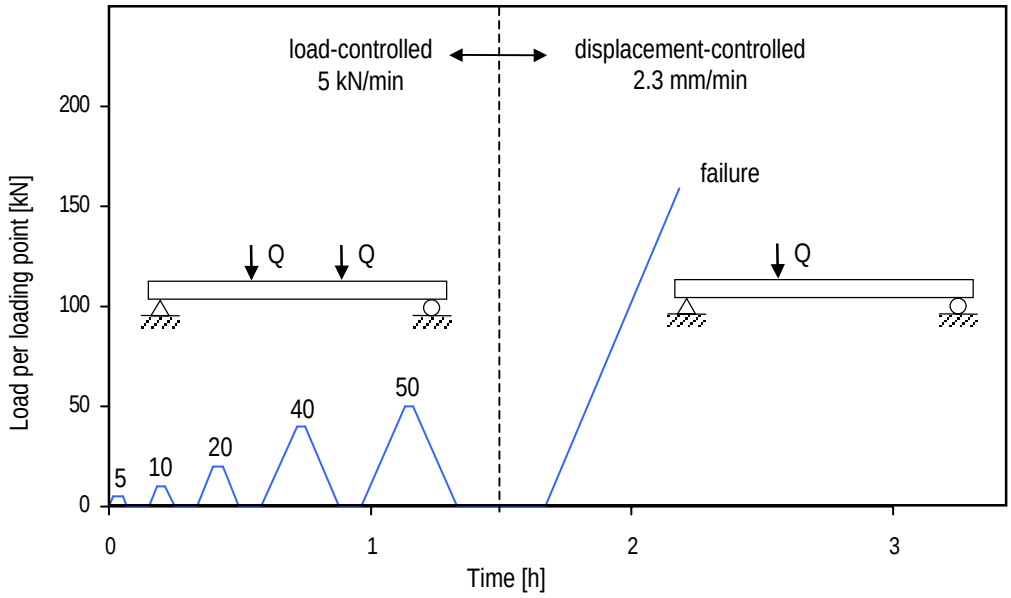

Figure 22 Loading procedure, beam PS2

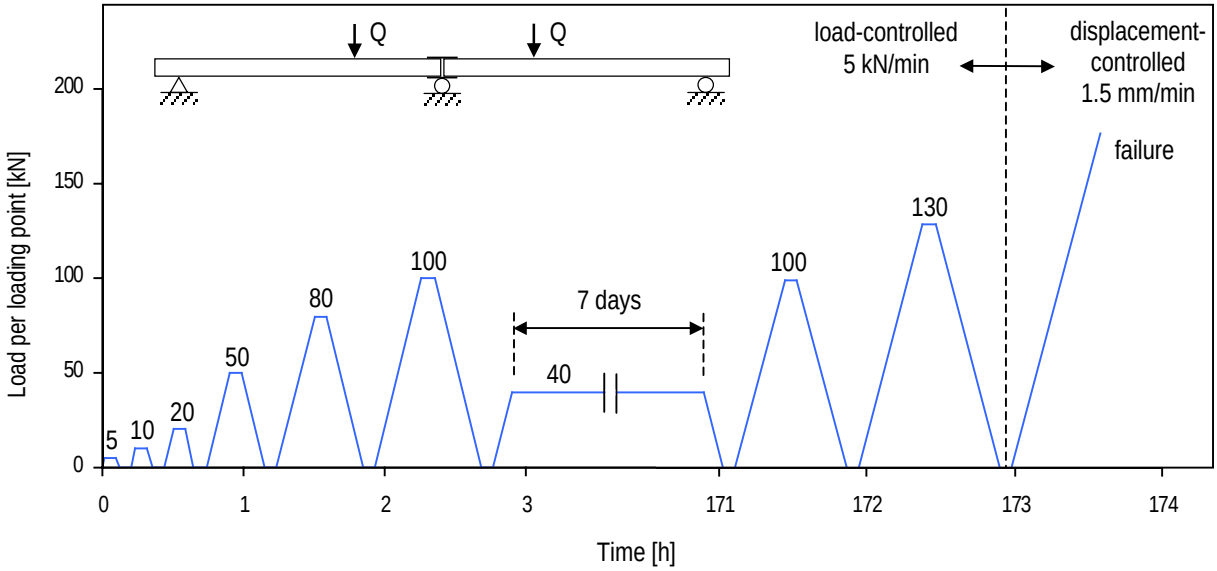

Figure 23 Loading procedure, beam PH2

4 Experiment Results and Discussion

4.1 Simple Beams

4.1.1 Load-Displacement Relationship

4.1.1.1 Four-Point Bending Experiments

The beams were subjected to four or five cycles of loading up to 50 kN with a 1 min plateau after loading and a 5 to 10 min plateau after unloading. Vertical displacements at mid-span of beam PS2 are plotted in Figure 24. Load-deflection curves were similar; stiffness remained constant over cycle loads. Behavior was linear-elastic but loading and unloading curves were not identical; unloading deflections were higher than loading deflections. The unloading to loading deflection ratio increased during the unloading process - the increase was 5% at 40 kN and reached 17% at 10 kN for beam PS2. However beams recovered their initial position after the 5 to 10 min plateau in unloaded state, which is certainly due to the material's visco-elastic behavior.

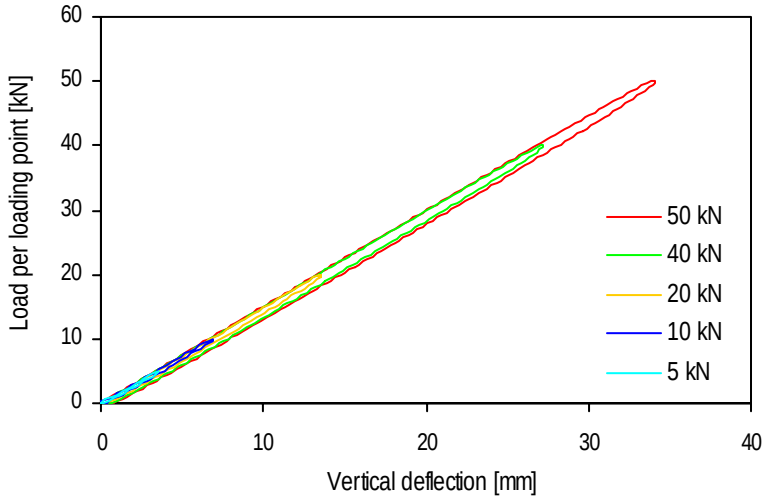

Figure 24 Load-deflection results at mid-span for beam PS2

The deflections were measured in the centerline with two displacement transducers, one per web, and the average value was calculated. Displacements measured on the support were 2-3% of the mid-span deflection, so these were disregarded in deflection estimations. The load is the average value of the measured loads of the two jacks. The variation between jack loads and average load were lower than 1% for PS1, 0.4% for PS2 and 0.3% for PS3. The load sensors installed on the supports confirmed the load measured on the jacks and indicated the asymmetry of the beam and loading. The load supports in the North and South were identical to 50% of the global load. Except for beam PS1, the West side was more loaded than the East; the variation was lower than 5% for beam PS2 and 8% for beam PS3. Displacement transducers also indicated higher displacement on the West side than the East; the variation was lower than 5% for beam PS2 and 4% for beam PS3.

The vertical deflections at mid-span and third points and fit curves at different load levels are plotted in Figure 25 for PS1-3.

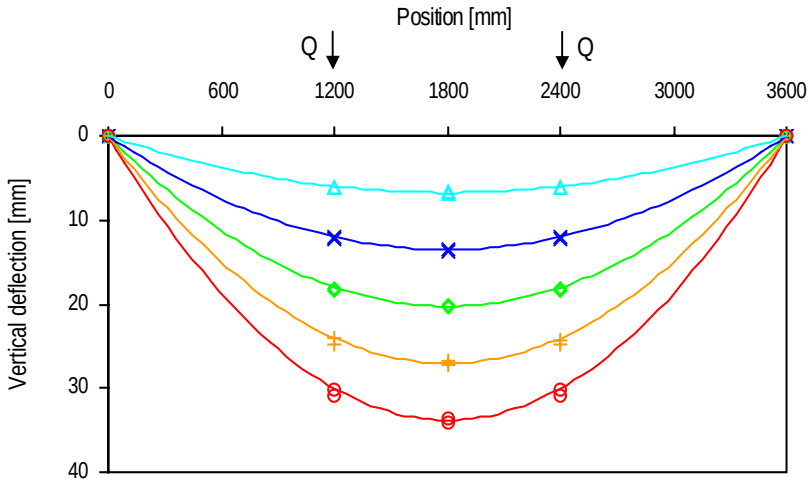

Figure 25 Deflections in longitudinal direction at 10, 20, 30, 40, 50 kN for beams PS1-3

Figure 27(b) and (c) shows the vertical displacements at mid-span and third points for the 50 kN loading cycle of beams PS2 and PS3. The first three curves in the legend are the calculated average values of measured deflections in the centerline of the webs and the other three are the measured deflections on the lower flange. At third points the deflections on the lower flange were approximately 5% lower than deflections in the webs, whereas at mid-span deflection on the lower flange was approximately 3% higher than deflection in the webs. Thus, at third points, the lower flange deformed in a convex way, while at mid-span it deformed in a concave way (Figure 26). Because of the deformation compatibility and the section's corner stiffness, the webs cambered in the opposite way. These secondary deformations are typical of thin-walled beams (Barbero et al. 1991, Zureick et al.1998) and are due to the concentrated applied load.

Figure 27(a) shows the vertical displacements at mid-span and third points for the 50 kN loading cycle of beams PS1. The first four curves in the legend are the measured deflections on the top and bottom of the webs at the North third point and the others are the calculated average values of deflections measured in the centerline of the webs at mid-span and the South third point. The deflection difference measured between the top and bottom of the webs increased during loading and reached 11% and 7% on the East and West webs respectively. This deformation also occurred during the third-point bending experiments where deflection variation reached 18% and 14% respectively.

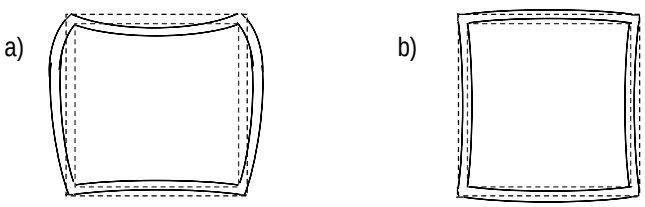

Figure 26 Cross-section deformations at (a) third points and (b) mid-span

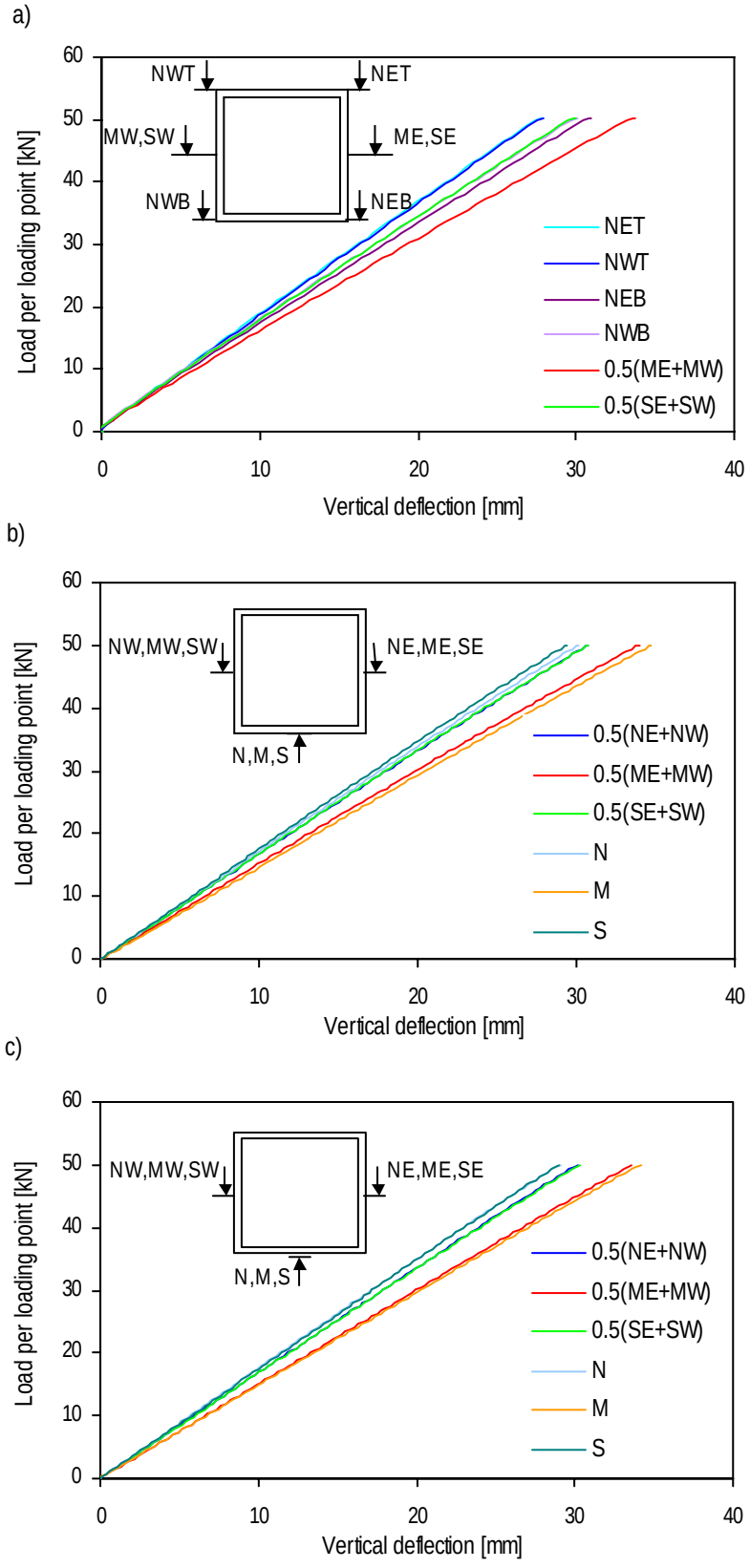

Figure 27 Load-deflection results at mid-span and third-points at 50 kN for beams (a) PS1, (b) PS2, (c) PS3

4.1.1.2 Three-Point Bending Experiments

Beams PS1 and PS2 were subjected to a three-point loading up to failure. Beam PS3 was first subjected to a loading cycle over 113 kN (approximately 72 % of failure load), the first cracking sound, then to loading up to failure (Figure 30).

The load-deflection curves at the load-application axis of the three simple beams are shown in Figure 28. The behavior of the beams was identical and linear-elastic up to 100 kN (approximately 65% of failure load), then it exhibited a slight stiffness reduction. At this load level, the slight stiffness decrease coincided with the onset of buckling of the compressed top flange of the beams. Three buckled half-wavelengths developed in the top flange, one below and one on either side of the load-application area (Figure 29). Stiffness decreased progressively up to 130 and 140 kN, approximately 90% of failure load, then the beams presented a greater loss of stiffness which remained almost constant up to failure load. A fourth buckled half-wavelength developed in the top flange on the South side reaching the mid-span. The observed local deformations could be retraced with the strain gages distributed across the width of the top flanges (see 4.1.3). Furthermore the webs buckled outwards below the jack owing to compressive stresses. Due to deformation compatibility the bottom flange was distorted. Figure 41 (e) gives a schematic illustration of the observed local deformations of the beams. Following buckling in beams PS1 and PS3, the top flange failed on the South side of the loading patch. The cracks across the flange width extended to a part of the webs. Simultaneously, longitudinal cracks appeared on beam PS1 30 mm below the upper edges, at the location of the overlap ends of the combined fiber mats (see 2.2.1). The failure of beam PS2 occurred through buckling of the webs under the load application area. Longitudinal cracks formed on both webs at 30 mm below the upper edges, the location of the overlap ends of the combined fiber mats, and at a quarter of the height, which is probably the location with the highest curvature. Figure 32 shows the failure modes.

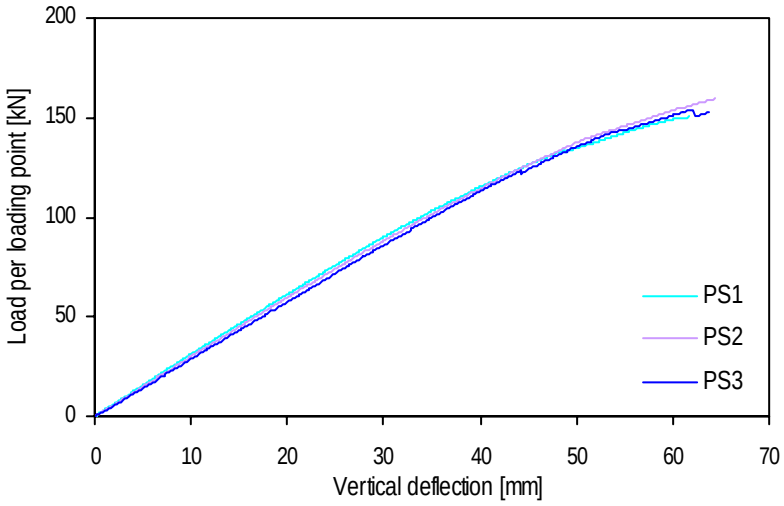

Figure 28 Load-deflection results at loading section for beams PS1-3

The failure loads and deflections at the loading section of beams PS1-3 are summarized in Table 10. The average failure load was 155 kN and the average deflection 66 mm, which corresponds to approximately 1/55 of span length.

Figure 29 Buckling deformation in beam PS3

As previously mentioned, beam PS3 was first subjected to a loading cycle up to 113 kN (approximately 72% of failure load), subsequently it was loaded up to failure. The load-deflection curves on the load-application axis of beam PS3 are plotted in Figure 30. The load-deflection curves were similar. Beam behavior was linear-elastic and stiffness remained constant.

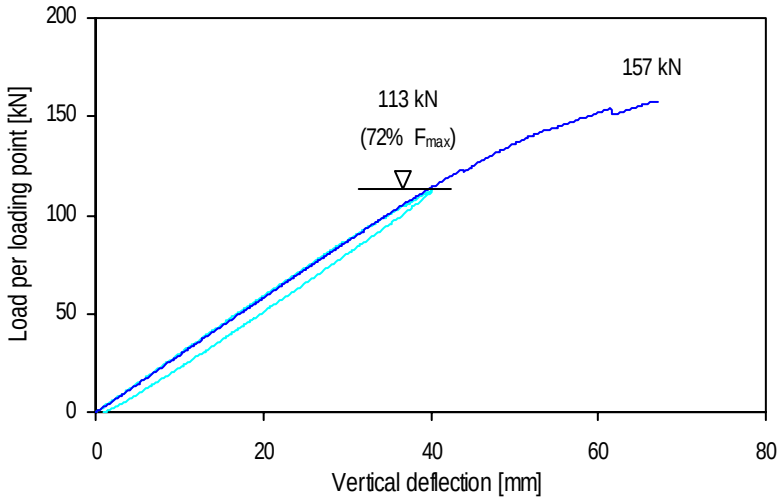

Figure 30 Load-deflection results at loading section for beam PS3

The vertical deflections at mid-span and third points and fit curves at different load levels are plotted in Figure 31 for PS1-3. The displacements measured on the support were lower than 4% of loading- section deflection, so they were disregarded in deflection calculation. The load was measured by the load cell in the jack. The variations between jack loads and average value were 2% for PS1 and 1% for PS2 and PS3. The load sensors installed on the supports confirmed the load measured on the jack and indicated the asymmetry of the beam and loading. Loads at the Northand South supports were 0.67 (2/3) and 0.33 (1/3) respectively of the total load, in agreement with static calculation. Except for beam PS1, load

distribution between the four load sensors was quite uniform. The deflections at mid-span and on the load-application section were similar and maximum deflection was between these two sections.

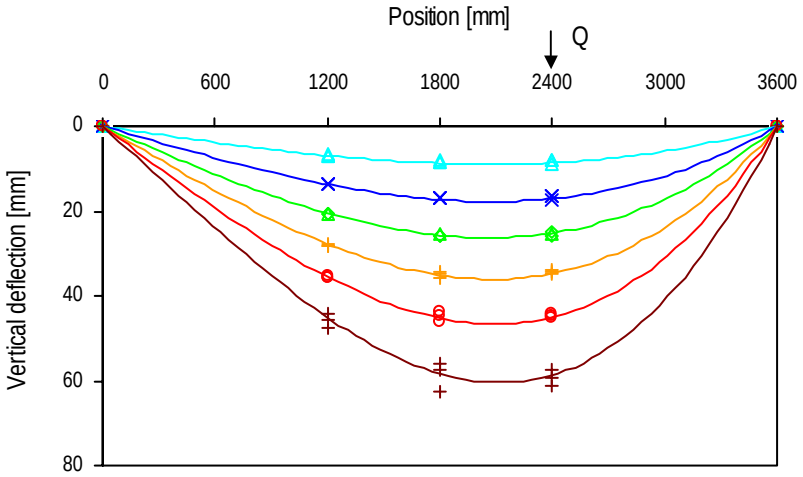

Figure 31 Deflections in longitudinal direction at 25, 50, 75, 100, 125, 150 kN for beams PS1-3

Table 10 summarizes the load at the onset of buckling Q_b, ultimate load at failure Q_u, bending moment at buckling M^+_b, bending moment at failure M^+_u, axial stress at buckling σ_b, axial stress at failure σ_u, rotation at failure at the North edge support (the support closer to the jack) $\theta_{M,u}$, rotation at failure at the South edge support $\theta_{E,u}$, loading-section deflection at buckling $w_{F,b}$, loading-section deflection at failure $w_{F,u}$ and loading-section deflection to span ratio at failure $w_{F,u}$ /L. The onset of local buckling load was determined with strain measurements at 200 mm from the loading point. Axial stresses at the flanges were obtained with the elastic flexure formula σ_x=M/I.y where I is the moment of inertia and y is the distance from the neutral axis.

Table 10 Experimental data for beams PS1-3

Beam	Q_b [kN]	Q_u [kN]	M^+_b [kNm]	M^+_u [kNm]	σ_b [MPa]	σ_u [MPa]	$\theta_{M,u}$ [°]	$\theta_{E,u}$ [°]	$w_{F,b}$ [mm]	$w_{F,u}$ [mm]	$w_{F,u}$ /L [-]
PS1	106	150	84	119	104	148	2.80	2.24	36	65	1/56
PS2	116	159	92	126	114	157	2.90	2.35	41	64	1/55
PS3	-	157	-	124	-	155	-	-	-	69	1/52
m	111	155	88	123	109	153	2.85	2.30	39	66	1/55
s	7	5	6	4	7	5	0.07	0.08	4	3	

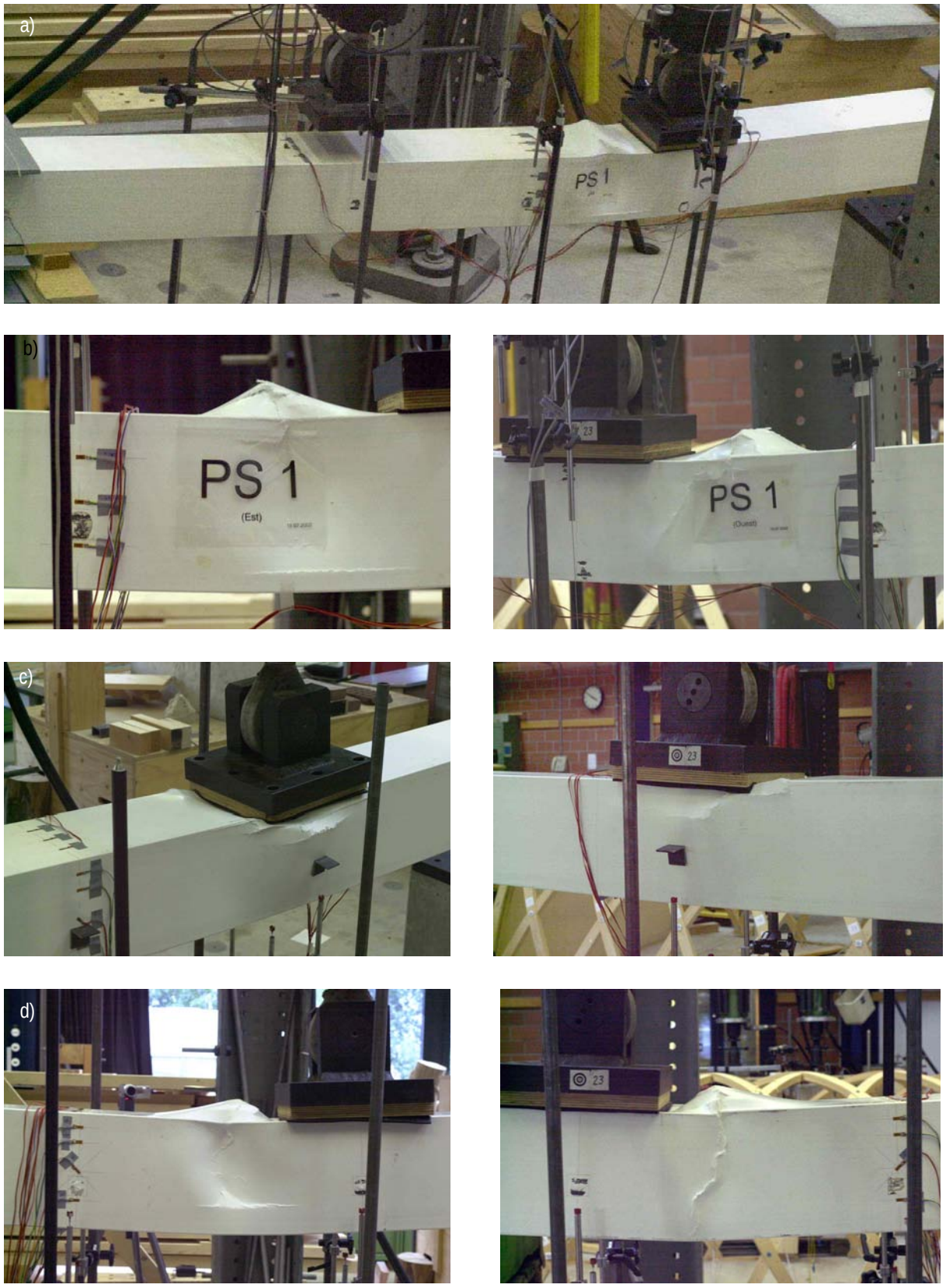

Figure 32 Failure of beams PS1-3 (a) global view of PS1; East and West sides (b) PS1, (c) PS2, (d) PS3

4.1.2 Load-Rotation Relationship

4.1.2.1 Four-Point Bending Experiments

The support rotations of beam PS1 are plotted in Figure 33. The rotations were measured in the centerline with two clinometers, one per web, and the average value was calculated. The two supports had the same rotations. They exhibited linear-elastic behavior. Since the load-rotation curves are not smooth, interpolating curves have been determined for the South and North rotations. Variation between the fitted curves is lower than 0.5%. Figure 34 illustrates deflections at mid-span and third points and support rotations at 50 kN.

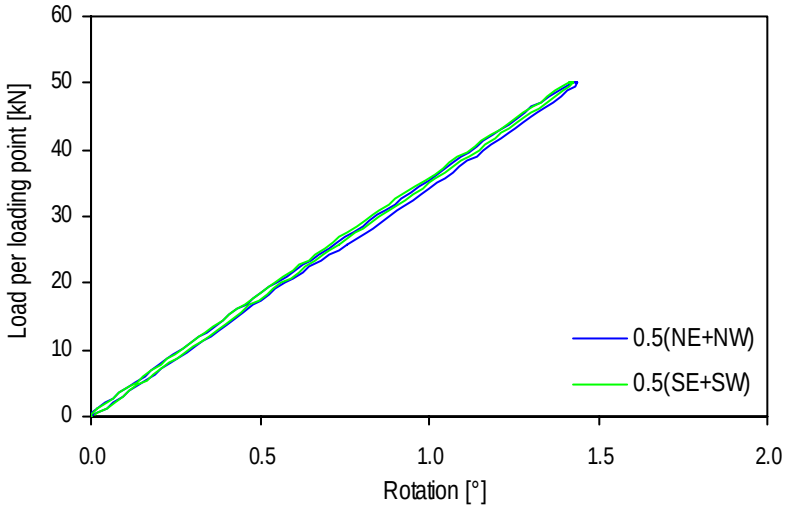

Figure 33 Load-rotation results at supports at 50 kN of beam PS1

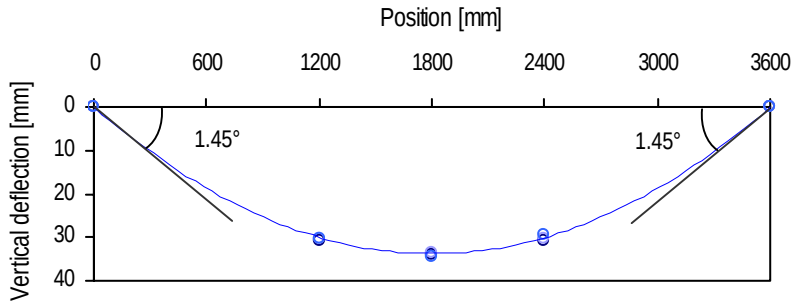

Figure 34 Deflections in longitudinal direction and support rotation angles at 50 kN of beams PS1-3

4.1.2.2 Three-Point Bending Experiments

The average support rotations of beam PS1 are plotted in Figure 35. Load-rotation curves were approximately bilinear with a stiffness reduction of between 120 and 140 kN as for deflection curves. The North support rotation was 1.25 higher than the South rotation, corresponding to the estimation

made using engineering rotation equations from the beam theory (ignoring shear deformations). Figure 36 illustrates deflections at mid-span and third points and support rotations at 50 kN.

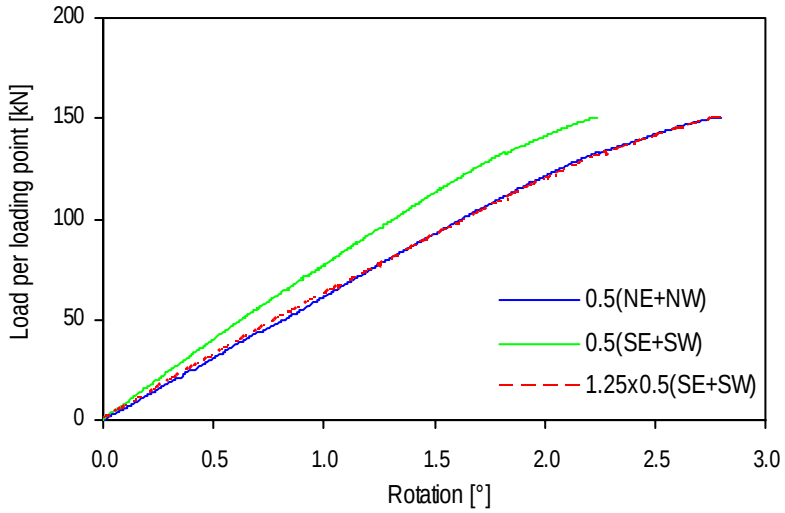

Figure 35 Load-rotation results at supports of beam PS1

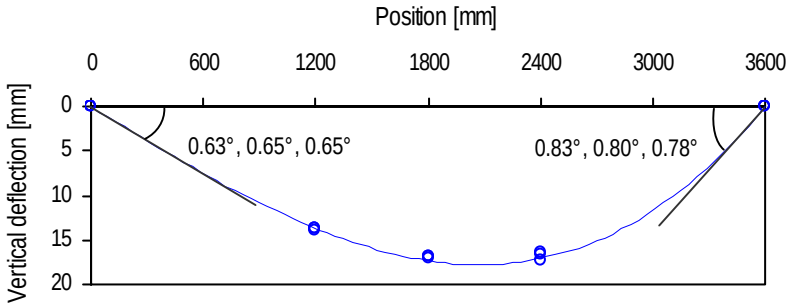

Figure 36 Deflections in longitudinal direction and support rotation angles at 50 kN of beams PS1-3

4.1.3 Strain Measurements

4.1.3.1 Four-Point Bending Experiments

The axial strain gages at mid-span and 200 mm from the loading axis showed linear behavior (Figure 37(a)). The strains were uniformly distributed across the width so no reduction due to shear lag effect was observed (Figure 38). The strains remained linear across the section height and low variations existed between the East and West webs (Figure 39). Compression strains were generally higher than tensile strains. The neutral axis of beam PS1 was 1 or 2 mm below the centerline, which is less than 2% of the mid-height. Results indicated unequal compression and tension moduli and/or the non-homogenous properties of the material due to the non-uniform fiber distribution. The unequal moduli indicate a higher value in traction than compression.

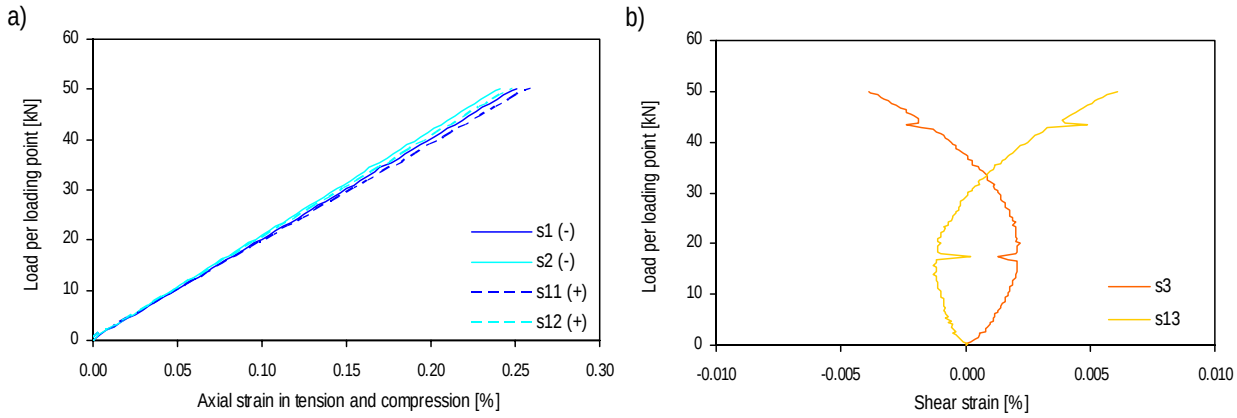

Figure 37 (a) Load-axial strain curves of gages at mid-span of beam PS1; (b) Load-shear strain curves of gages at mid-span of beam PS2

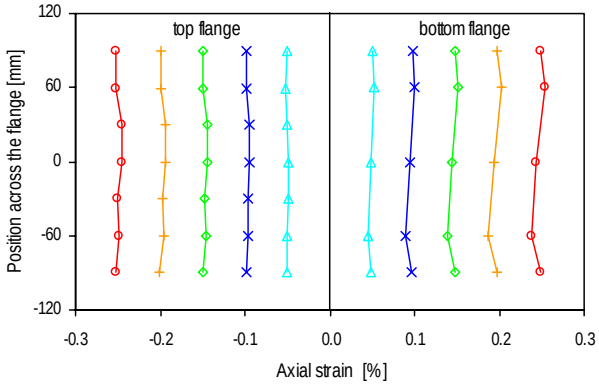

Figure 38 Axial strain distribution across the width of the top and bottom flanges at mid-span at 10, 20, 30, 40, 50 kN of beam PS3

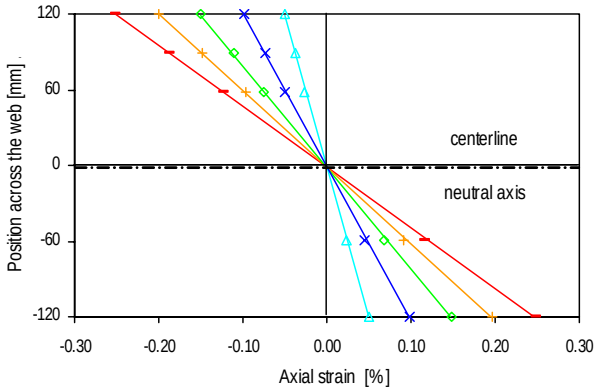

Figure 39 Axial strain distribution across the West web height at mid-span at 10, 20, 30, 40, 50 kN of beam PS3

Strain gages placed at 45° at mid-span of beams PS2 and PS3 indicated strains close to zero behavior as expected (Figure 37(b)).

4.1.3.2 Three-Point Bending Experiments

Axial strain in the tension-stressed bottom flange at mid-span and 200 mm from the third-points increased linearly up to failure (Figure 41(a)), whereas axial strain in the compression-stressed top flange at mid-span and 200 mm from the loading axis began to decrease nonlinearly from a certain load level due to local buckling deformations observed during experiments (Figures 41(b), (c) and (d)). Gages installed at 200 mm from the loading axis indicated a strain reduction due to the convex buckled half-wavelength at 106 kN for beam PS1 and 116 kN for beam PS2, approximately 70% of failure load, while gages at mid-span indicated a strain increase due to the concave buckled half-wavelength between 133 and 143 kN, approximately 90% of failure load (Figure 41(e) section B-B and section C-C respectively). As shown by the bending moment diagram, the three buckled half-wavelengths located under the loading and in both sides developed at approximately the same time. Comparison of load-displacement curves with load-strain curves shows that the initial slight loss of stiffness of the beams corresponded to the development of these three buckled half-wavelengths and the last loss of stiffness corresponded to the buckled half-wavelength developed at mid-span. Gages installed in the centerline of the flange were deformed earlier and more than those closer to the edge (Figure 41(c)). Figure 41(e) gives a schematic illustration of the observed local deformations on the beams.

The strain gages placed at 45° at the mid-span centerline of beams PS2 and PS3 indicated shear deformations (Figure 40). These gage measurements were also influenced by buckling deformations at high load levels.

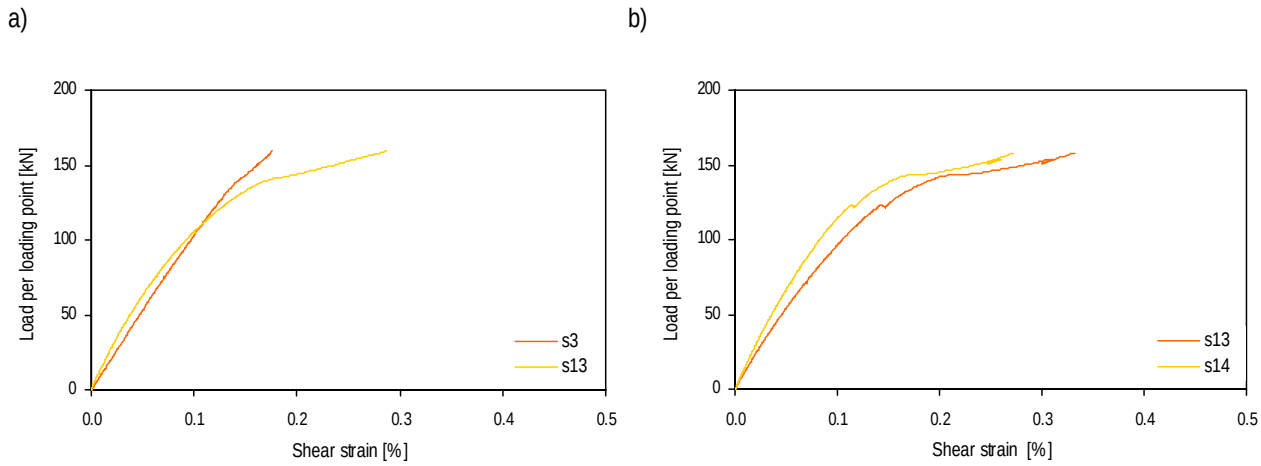

Figure 40 Load-strain curves of gages at 45° at mid-span of beams (a) PS2, (b) PS3

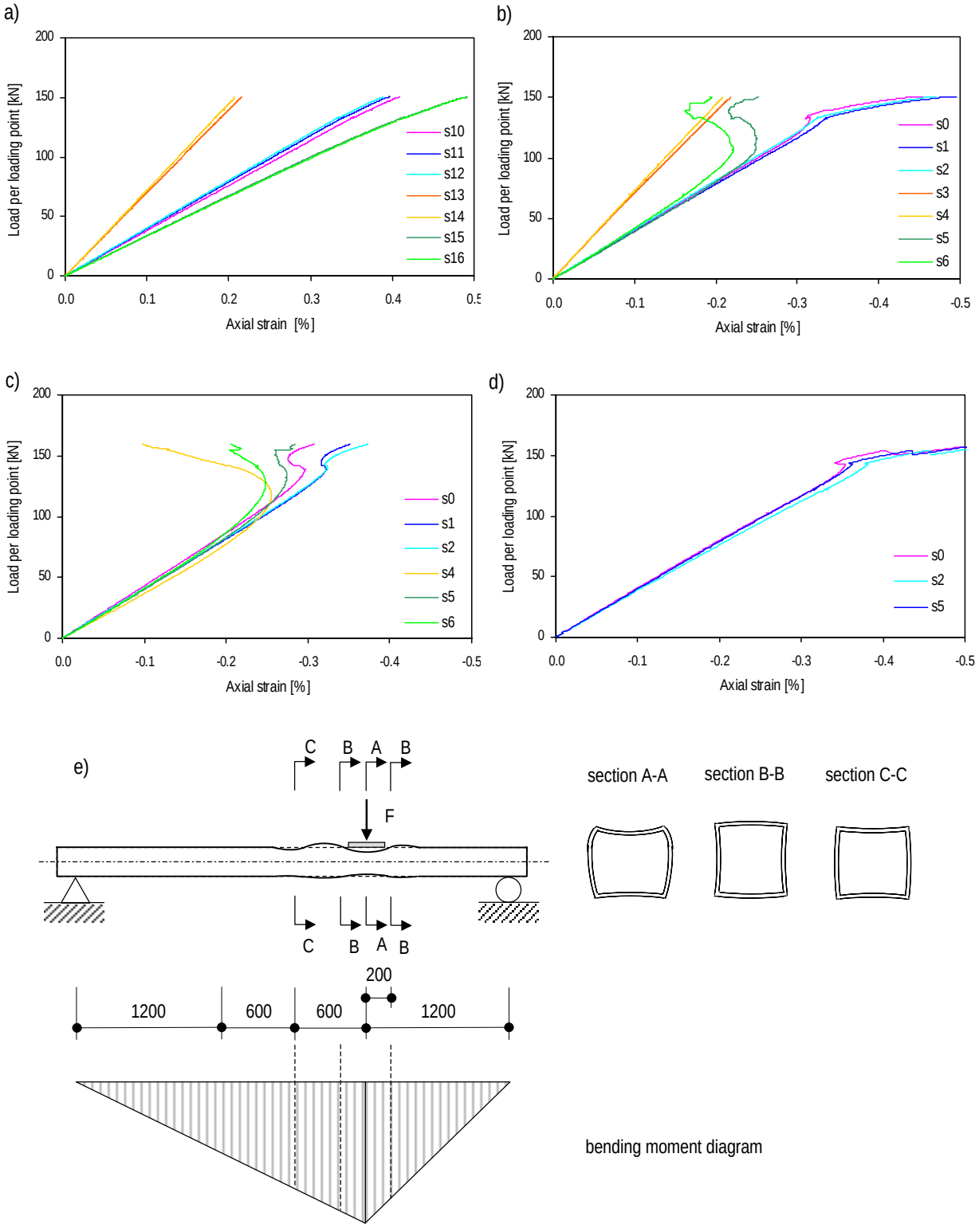

Figure 41 Load-axial strain curves of gages (a) in tension on beam PS1; in compression on beams (b) PS1, (c) PS2, (d) PS3, (e) Schematic illustration of local deformations

Figure 42 shows the strain distribution across the web height at 200 mm from the loading axis at 50 kN of beams PS1 and PS2 and the estimated strain distribution using the beam theory.

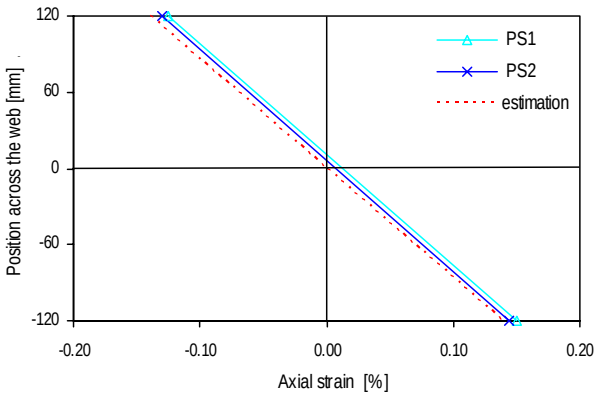

Figure 42 Axial strain distribution across web height at 50 kN for beams PS1 and PS2 at 200 mm from loading axis

4.1.4 Full-Section Elastic and Shear Moduli

The full-section elastic and shear moduli were determined experimentally using the deflections, rotations and strain data with three methods.

Method 1

The deflection at mid-span of a simply-supported beam subjected to a four-point bending loaded in the third points is expressed by:

$$w_m = \frac{23QL^3}{648EI} + \frac{QL}{3GKA} \tag{1}$$

and the deflection at the third points under the loading is:

$$w_F = \frac{5QL^3}{162EI} + \frac{QL}{3GKA} \tag{2}$$

Flexural stiffness EI is the product of elastic modulus E and inertia moment I and shear stiffness GKA is the product of shear modulusG, shear coefficient K and cross section area A. The shear coefficient is determined from the transverse shear strain energy (virtual works method) and accounts for the non-uniform distribution of transverse shear stresses through the cross-section (Gere and Timoshenko 1984). The shear coefficient depends on cross-section geometry and material mechanical properties (Dharmarajan and McCutchen 1973). The author used Odmivar's formula (1998) for estimating the shear coefficient K (=0.42) of thin-walled square tubes and corrected it to take into account actual non-uniform shear distribution across the wall thickness. Applying the appropriate formula from Roark (Young 1989) the shear coefficient is reduced by the thick-walled correction factor (=0.91). The resulting shear coefficient 0.38.

The deflections were measured and span length L is known. The full-section elastic and shear moduli can be calculated as follows:

$$E = \frac{QL^3}{216I} \cdot \frac{1}{(w_m - w_F)} \tag{3}$$

$$G = \frac{QL}{KA} \cdot \frac{1}{(23w_F - 20w_m)} \tag{4}$$

Method 2

The relationship between the end rotation and the load is:

$$\theta = \frac{QL^2}{9EI} + \frac{Q}{GKA} \tag{5}$$

so, the elastic modulus can also be computed as follows:

$$E = \frac{QL^2}{9I} \cdot \frac{1}{\theta} \tag{6}$$

then the shear modulus can be calculated from equations (2) and (3) as

$$G = \frac{QL}{3KA} \cdot \frac{1}{\left(w_m - \frac{23PL^3}{648EI}\right)} \tag{7}$$

Method 3

In the four-point bending experiments, the beam part between the two loading points was in pure bending state. Thus, the axial strains measured at mid-span were free of shear influence and could be used to compute the elastic modulus.

$$\begin{cases} \sigma_x = \dfrac{M}{I} \cdot y \\ \sigma_x = E \cdot \varepsilon_x \end{cases} \tag{8}$$

(9)

where M is the bending moment (M=FL/3), σ_x is the axial stress and ε_x is the axial strain at distance y from the neutral axis. The elastic modulus can be calculated as follows:

$$E = \frac{QL}{3I} \cdot \frac{y}{\varepsilon_x} \tag{10}$$

In the three-point bending experiments, the mid-span was subjected to a bending and shear load. Since axial strain at the centerline is nearly zero, the strain at 45° to the axis is only affected by shear deformations and could be used to compute the shear modulus (Frey 1994 and 1998).

$$\begin{cases} \tau_{yz,max} = \dfrac{3Vz^2}{16I} \end{cases} \tag{11}$$

$$\tau_{yz,max} = G\gamma_{yz} = 2G\varepsilon_{yz,max} \tag{12}$$

where *V* is the shear at mid-span (V=Q/3) , $\tau_{yz,max}$ is the shear stress, $\gamma_{yz,max}$ is the shear strain and $\varepsilon_{yz,max}$ is the related axial strain at the centerline where shear deformation reaches the maximum value, z is the distance between flange axes. The shear modulus can be calculated as follows:

$$G = \frac{Qz^2}{32I} \cdot \frac{1}{\varepsilon_{yz,max}} \tag{13}$$

Table 11 summarizes the calculated full-section moduli. The elastic and shear moduli were estimated using the three different methods, which explains the variability in results. The deflection and rotation-deflection methods are based on strain energy and considered measurements of four-point bending experiments. The third method is based on stress and strain relationships; E is determined with longitudinal strain measurements at mid-span from the four-point bending experiments and G with strain measurements at 45° to the longitudinal axis at mid-span from the three-point bending experiments. The average value was computed in the 10-50-kN load interval.

Table 11 Experimentally-determined full-section moduli

Beam	Deflections		Rotations/Deflections		Strains	
	E [MPa]	G [MPa]	E [MPa]	G [MPa]	E [MPa]	G [MPa]
PS1	30484	2490	30050	3196	30432	-
PS2	31793	2303	29754	3266	30645	4155
PS3	34001	1618	29690	3517	29940	4364

Figure 43 shows the experimentally-determined full-section moduli of beam PS2 using Method 1.

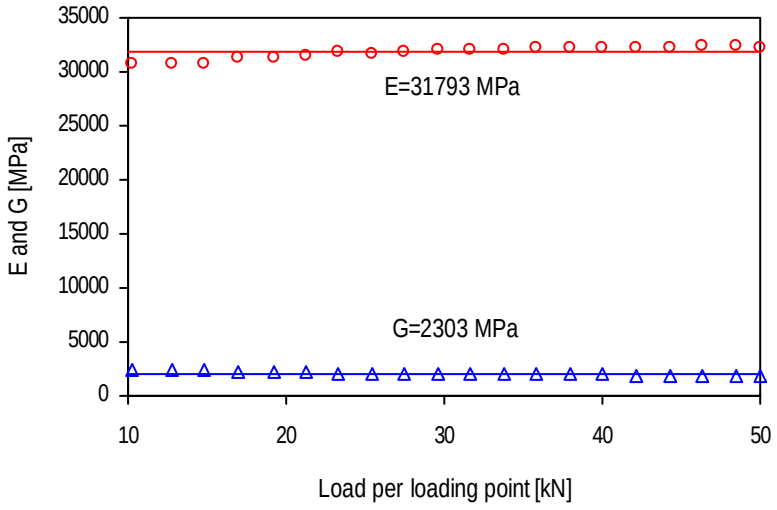

Figure 43 Experimentally-determined full-section moduli (with deflections) of beam PS2

Zureick et al. (1994) warned that calculation of E and G using the deflections must be done carefully since the experimental values of deflections at mid-span and third points are similar. E and G values are very sensitive to the variation of (w_m-w_F) and ($23w_F$-$20w_m$). This estimation method does not seem the most appropriate. A load location closer to the support will probably lead to higher deflection differences at mid-span and loading points and thus better modulus evaluation.

Furthermore, it must be noted that g is very sensitive to E value variations using the rotation-deflection method. A variation of ± 5 % in E (equal to 30000 MPa) leads to a G variation of +60 % and -25 %. G estimated with strain gage measurements is 42% higher than that estimated with rotation-displacement measurements. The first method estimated the "material modulus" whereas the second estimated the "full-section modulus".

A G estimation error has less effect than an E estimation error since shear deflections are lower than bending moment deflections (Table 12). For the four-point bending experiments, shear deflection at mid-span and third points corresponds to 14% and 17% respectively of global deflection. Thus calculation of shear deflection with the G value from the rotation method and the G value from the strain method, which is 42% higher, results in a respective variation of only 6% or 7% in global deflection.

The shear-to-elastic-modulus ratio is approximately 0.10; this value is lower than that of linear-elastic isotropic materials such as steel (0.38) and stone (0.43). For this reason, orthotropic GFRP materials exhibit larger shear deflections than isotropic materials. Ignoring the shear deformation in measurement analysis leads to a lower "apparent" elastic modulus (Mottram 1991).

Table 12 Shear and bending influence in total deflection (%)

Beam	Four-point bending		Three-point bending	
	Shear	Bending	Shear	Bending
PS1	17	83	19	81
PS2	13	87	16	84
PS3	13	87	17	83

4.2 Continuous Beams

4.2.1 Load-Displacement Relationship

Beams were first subjected to five cycles of loading up to 100 kN with a 2 or 3 min plateau after loading and unloading. Subsequently they were subjected to a loading up to failure. Vertical displacements at the North load-application point (displacement cell of the jack) of beam PC3 are plotted in Figure 44. Load-deflection curves were similar; stiffness remained constant over cycle loads up to 50 kN and slight stiffness reduction was perceived at 55 kN on the cycle up to 100 kN, approximately 35% of failure load. This was probably due to the initial crushing of the wood plates at supports. The loading up to failure also indicated a slight stiffness reduction compared to the cycle up to 100 kN. Beam behavior was linear-elastic but loading and unloading curves were not identical; unloading deflections were higher than loading deflections. The unloading deflection to loading deflection ratio increased during the unloading process, the decrease was 13% at 80 kN, 36% at 50 kN and 93% at 20 kN for beam PC3 (deducting the "plateau value" after the 3 min plateau at 100 kN). However the beams recovered their initial position at the end of the unloaded state. As for beams PS1-3, this was certainly due to the material's visco-elastic behavior.

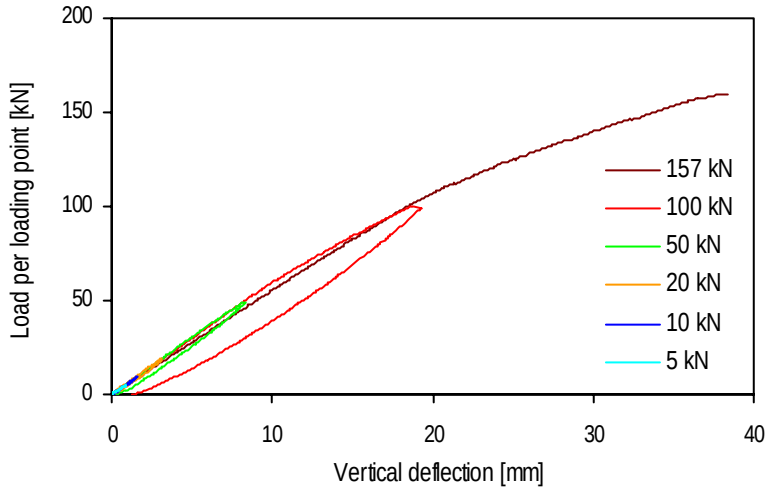

Figure 44 Load-deflection results at North loading section for beam PC1

The load-deflection curves of the three continuous beams are shown in Figure 45. The average values of the load at the two jacks and of the deflection in the two loading sections are indicated. The measured values on both spans matched well; variations were at the most 2% for PC1 and PC3 and 1% for PC2. The behavior of the three beams was identical and linear-elastic up to 100 kN (approximately 70% of failure load), then a loss on stiffness corresponding to 30% of initial stiffness was observed. As for the simple beams PS1-3, the stiffness decrease coincided with the onset of buckling of the most compressed flanges and webs located, for continuous beams, at the mid-support (Figure 46). Three buckled half-wavelengths developed in the bottom flange, one under and one on each side of the mid-support area (Figure 54(c)). The local deformations were also detected by strain gages but in a less perceptible way

than for beams PS1-3, where gages were located in the flanges instead of the webs (see 4.2.3). Webs buckled due to compressive stresses in the support area. Due to deformation compatibility the top flange was distorted. Lower secondary deformations than for beams PS1-3 were observed in the loading area. Following buckling, the beams failed at the mid-support; Figure 51 shows the failure modes. Longitudinal cracks formed in the bottom flange and the webs approximately 30 mm above the lower edges, the region of the overlap ends of the combined fiber mats (see 2.2.1). The wood plate at the support smashed into the beam. Beam PC3 exhibited an additional crack at 60 mm above the lower West web edge, probably the location with the highest curvature and therefore the highest strain in the beam's transversal direction. Beam PC2 presented a crack in the East web at 60 mm above the lower edge but none at 30 mm.

The failure loads and deflections at the loading-application section of beams PC1-3 are summarized in Table 13. The average failure load was 146 kN and average deflection at the loading section was 32 mm, which corresponds to approximately 1/116 of span length. The failure loads were slightly below the values of the simple beams and deflections represented approximately 50% of simple beam values.

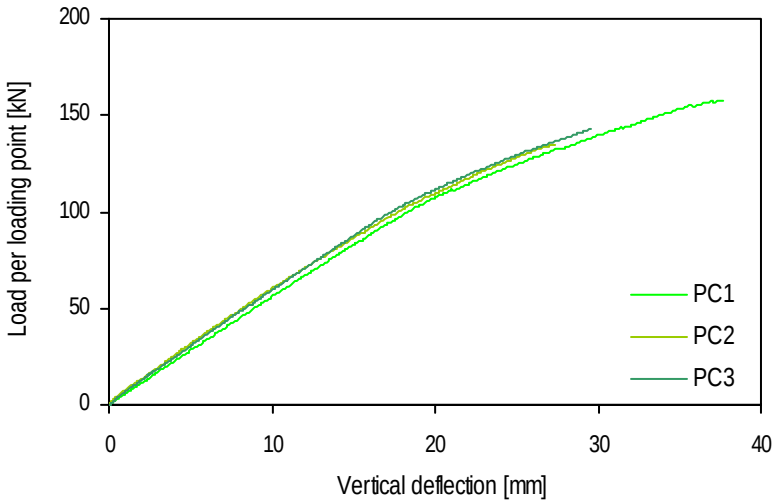

Figure 45 Load-deflection results at North loading section for beams PC1-3

The deflections at the loading section were measured in the centerline with two displacement transducers, one per web, and an average value was calculated. Displacements measured at the edge supports of beam PC1 were small compared to those measured at load-application points, and they were therefore disregarded in deflection calculations. On beams PC2 and PC3 displacements at edge supports were also negligible, whereas displacements at the mid-support were approximately 30% of load-application point deflections (Figures 47(a) and (b)), probably due to the softer support set-up compared to PC1 (see Section 3.2). Thus they were considered for the beam axis deflection estimation as illustrated in Figure 47(c). Displacement measured at the mid-support top flange should be the same as beam centerline displacement but this assumption is not altogether correct since the former included wood-plate crushing deformations and secondary deformations of the section. The decrease of the mid-support

displacement slopes shown in Figure 47(b) corresponds to the previously mentioned beam stiffness reduction also detected with the span transducers and clinometers (see 4.2.2).

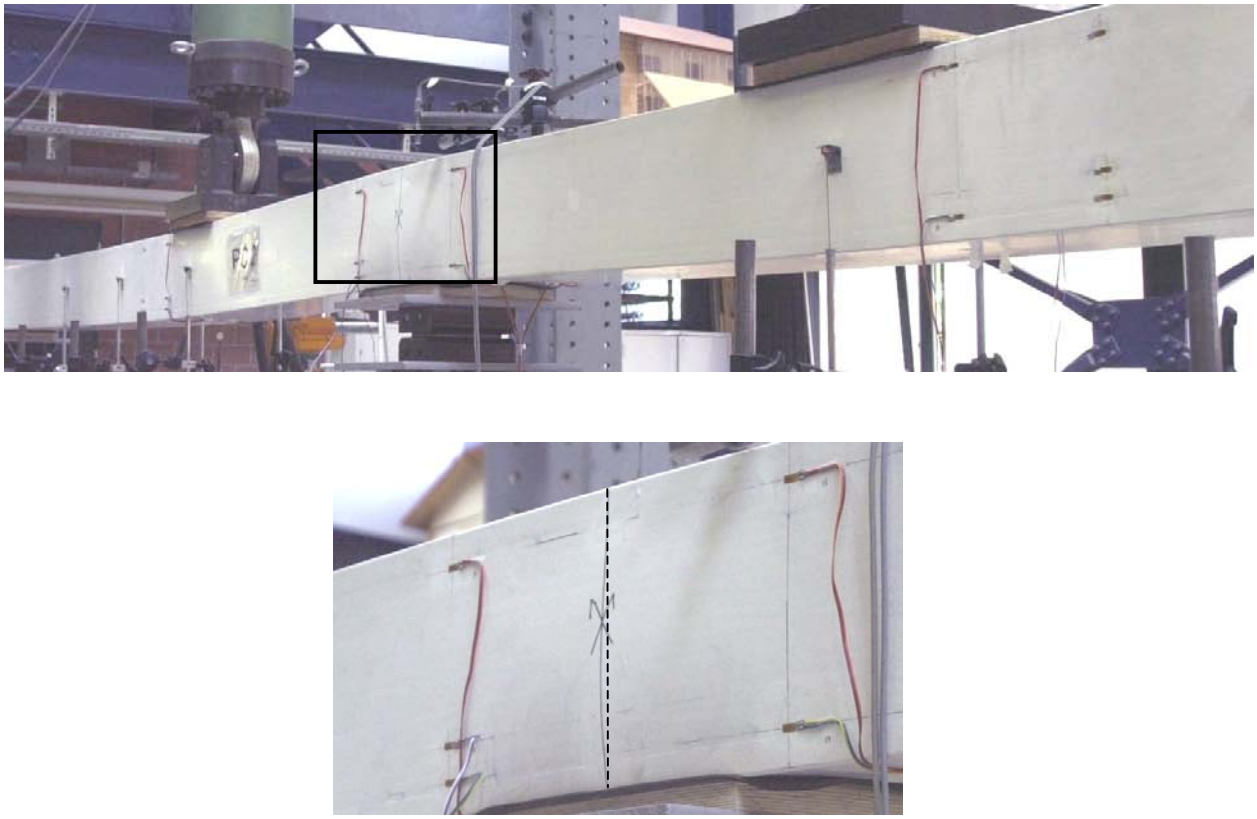

Figure 46 Buckling deformation at mid-support of beam PC2

Displacement transducer measurements of beams PC1 and PC2 indicated higher displacement in one web than in the other but variations were lower than 5%. Beam PC3 exhibited greater differences, the East side was more loaded than the West side, and variations reached 20%. Figure 50 shows vertical displacements at mid-span and third points and fit curves at different load levels for PC1-3. The variations between webs indicated a slight torsion of the continuous beams. Span 1 (North span) of beam PC1 presented slightly higher deflections than span 2 (South span), the maximum variation being 5%. For beams PC2 and PC3, deflections at mid-span and load-application points were quite similar, the variation being lower than 3%, but deflections at the external third points were rather different, deflection on span 1 being higher than span 2 and the variation reaching 13%. Comparison of beams PC2 and PC3 with beam PC1 indicated that the measurements on span 1 of beams PC2 and PC3 were abnormal. As this difference was observed in all beams tested with the same set-up – beams PC2, PC3 and PH1-4 – it could be attributed to the set-up. An additional displacement transducer calibration indicated that it was not an instrumentation problem.

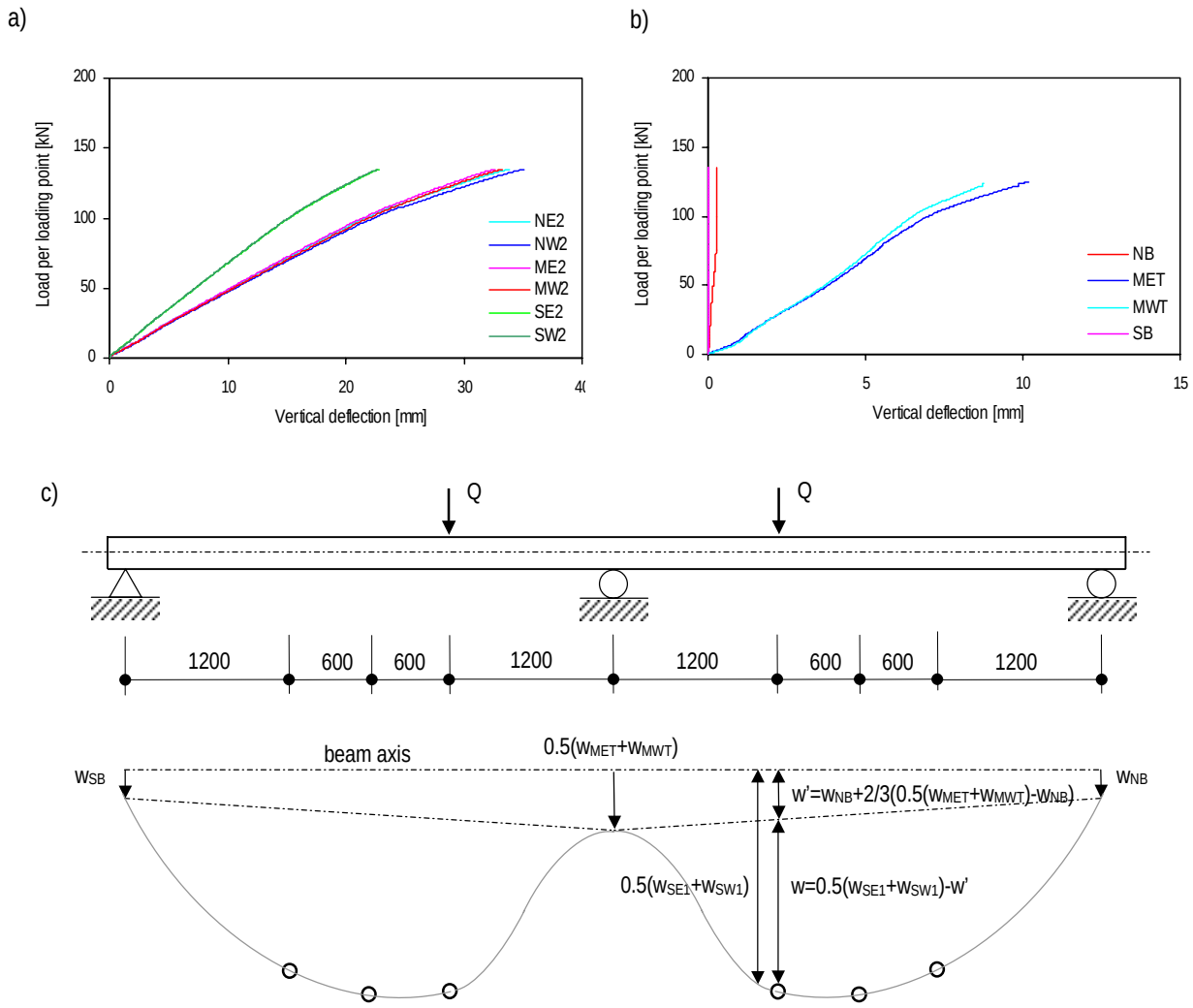

Figure 47 Load-deflection results for beam PC2 at (a) mid-span and third points in span 2 (South), (b) edge supports and mid-support; (c) Schematic illustration of deflection estimation

The load is the average value of the loads of the two jacks. Variations between jack loads and average value were at the most 1% for PC1 and PC3 and 2% for PC2. The load sensors installed on the supports confirmed the load measured on the jacks and indicated the asymmetry of the beam and loading. Variations between total load of load sensors and total load of jacks were at the most 3% for PC1 and PC2 and 4% for PC3. The load at the edge supports and mid-support changed with loading. Figure 48 shows the ratio of bending moment at mid-support to bending moment at loading point of beams PC1-3 from 10 kN up to failure. Bending moments are determined from the support reactions. The ratio was quite constant at the 50-100 kN load interval and decreased with increasing load. At 100 kN, bending moment at mid-support decreased and bending moment at loading points increased due to the mid-span stiffness reduction caused by local buckling. The ratio behavior of beam PC3 up to 50 kN could not be explained. The load at edge- supports and mid-support at the 50-100 kN load interval were 0.16 and 2×0.84 0.84 of the jack load for PC1 and PC2 and 0.17 and 2×0.8.83 of the jack load for PC3 respectively. These values were slightly different to those estimated with FEA calculation which includes

shear deformations and gives 0.15 (4/27) and 2×0.85 (2×23/27). Except for beam PC3, load distribution between East and West load sensors was quite constant; the variation was lower than 36% of the average value for beam PC1, 30% for beam PC2 and 54% for beam PC3. Variation at mid-support was lower than at edge-supports.

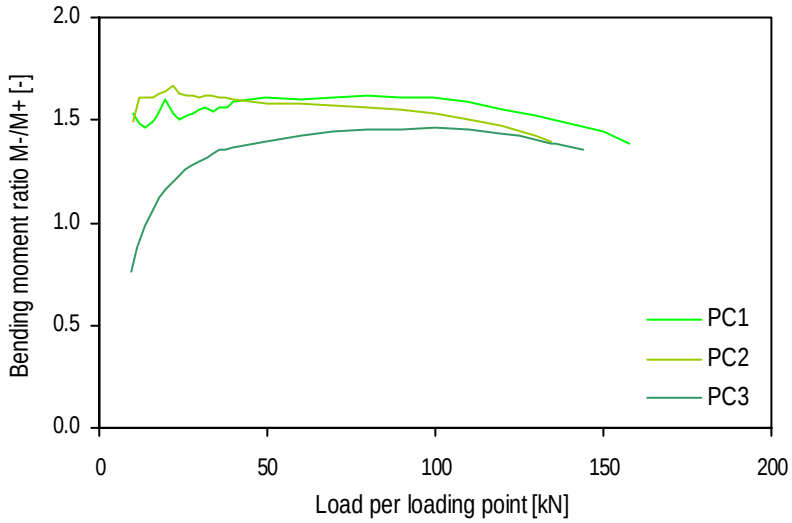

Figure 48 Ratio of bending moment at mid-support to bending moment at loading point of beams PC1-3

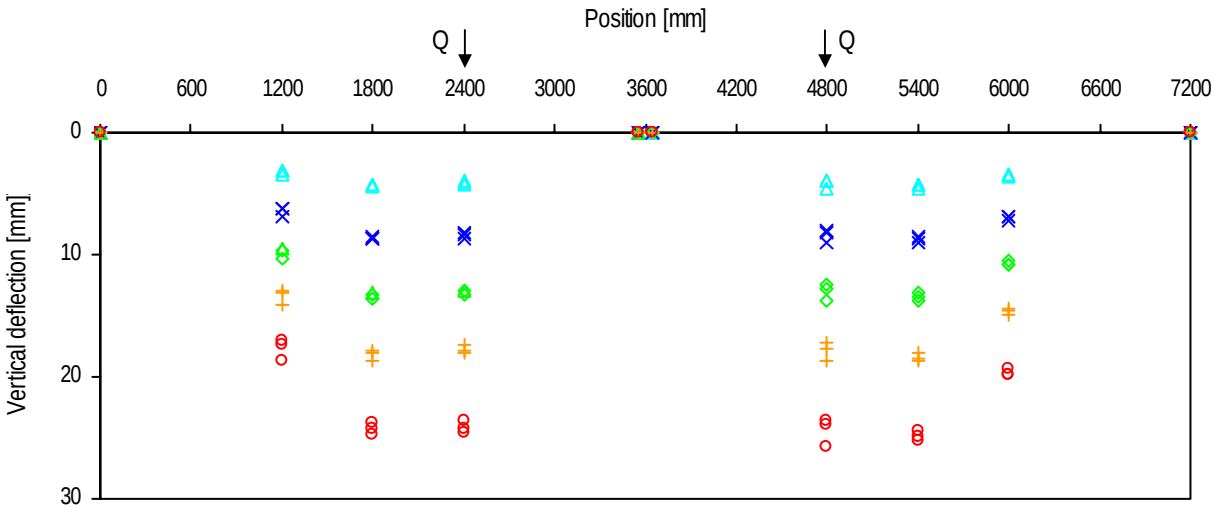

Figure 49 Deflections in longitudinal direction at 25, 50, 75, 100, 125 kN for beams PC1-3

Table 13 summarizes the ultimate load at failure Q_u, bending moment at failure in the loading section M^+_u, bending moment at failure at the mid-support M^-_u, axial stress at failure in the loading-section σ^+_u, axial stress at failure at mid-support σ^+_u, rotation at failure at edge supports $\theta_{E,u}$, loading-section deflection at failure $w_{F,u}$ and loading-section deflection to span ratio at failure $w_{F,u}$ /L. The bending moment is estimated from the support reactions at failure load, which were slightly different from those previously indicated at the 50-100 kN load interval (Figure 48). Axial stresses at flanges were obtained with the elastic flexure formula σ_x=M/I.y where I is the moment of inertia and y is the distance from the neutral axis.

Table 13 Experimental data for beams PC1-3

Beam	Q_u [kN])	M^+_u [kNm]	M^-_u [kNm]	σ^+_b [MPa]	σ^-_b [MPa]	$\theta_{E,u}$ [°]	$w_{F,u}$ [mm]	$w_{F,u}$ /L [-]
PC1	158	68	87	85	108	1.28	38	1/95
PC2	136	55	80	69	99	1.17	27	1/133
PC3	145	63	80	78	100	1.19	30	1/120
m	146	63	81	77	103	1.21	32	1/116
s	11	5	6	8	5	0.06	6	

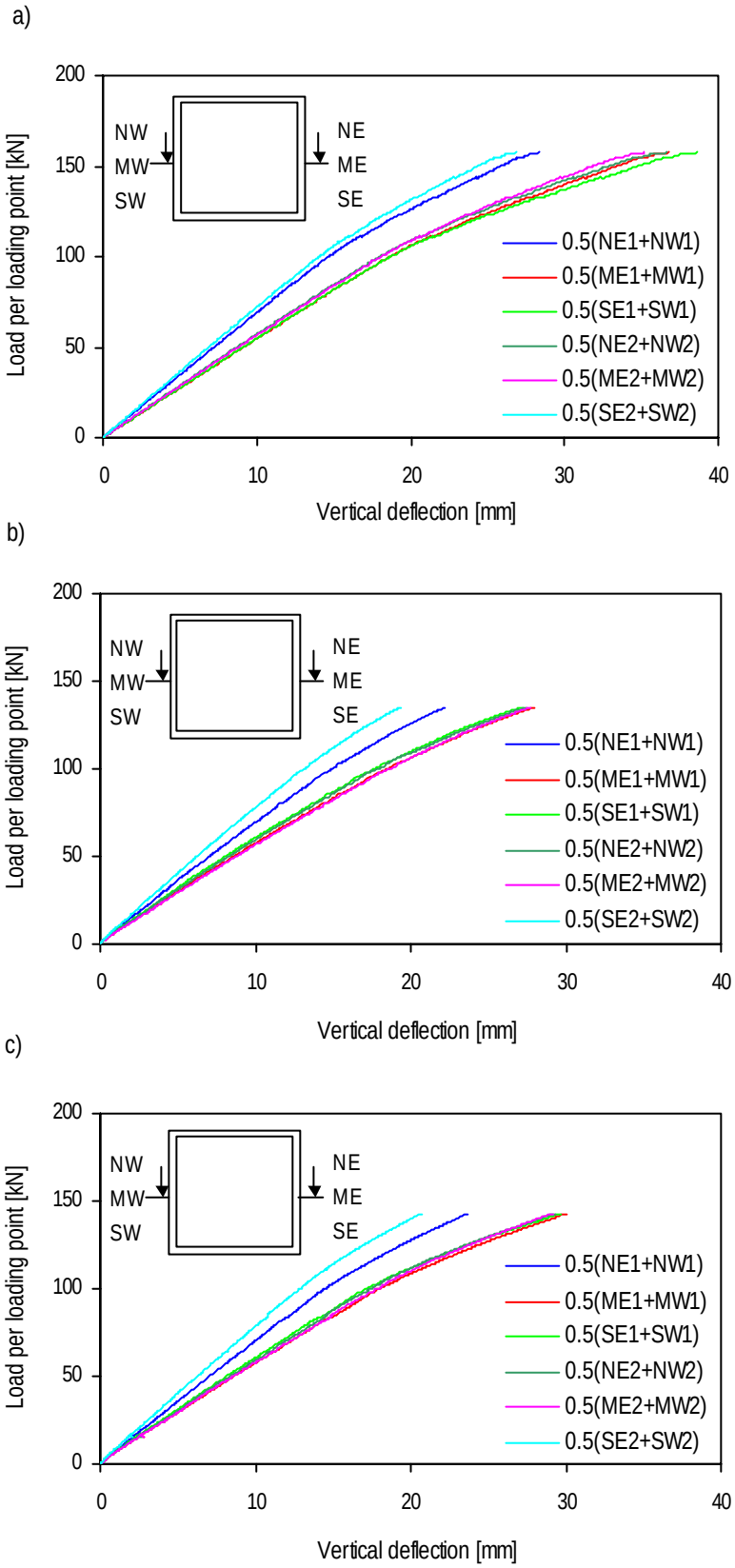

Figure 50 Load-deflection results at mid-span and third points for beams (a) PC1, (b) PC2, (c) PC3

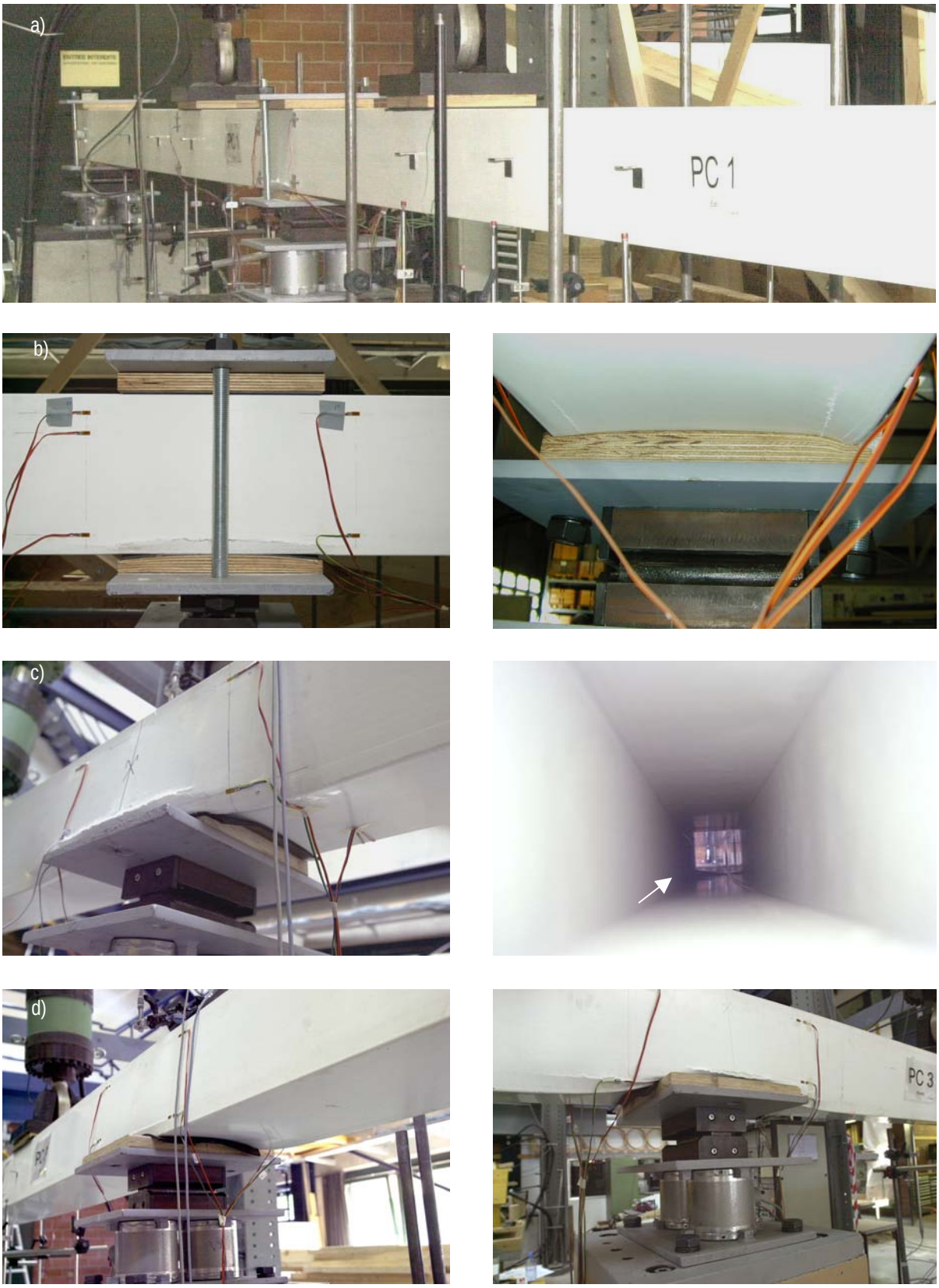

Figure 51 Failure of beams PC1-3 (a) global view of PC1; East and West sides (b) PC1, (c) PC2, (d) PC3

4.2.2 Load-Rotation Relationship

The edge rotations of beam PC2 are plotted in Figure 52. Rotations were measured in the centerline with two clinometers, one per web, and the average value calculated. The two edges had identical rotations. Mid-support rotations were supposed to be null due to the symmetrical loading. Load-rotation curves were bilinear with a stiffness reduction at 105 kN, approximately 77% of failure load, as for the load-deflection curves. The variation between North and South span measurements was lower than 5% for PC1, 4% for PC2 and 5% for PC3. Figure 53 illustrates deflections at mid-span and third points and edge rotations at 50 kN load level. Beam PC1 exhibited lower rotations than beams PC2 and PC3, probably due to its slightly different set-up.

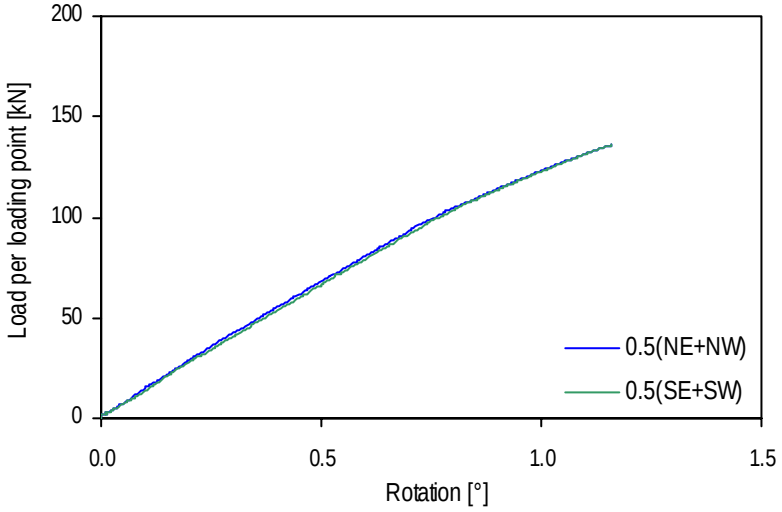

Figure 52 Load-rotation results at edge supports for beam PC2

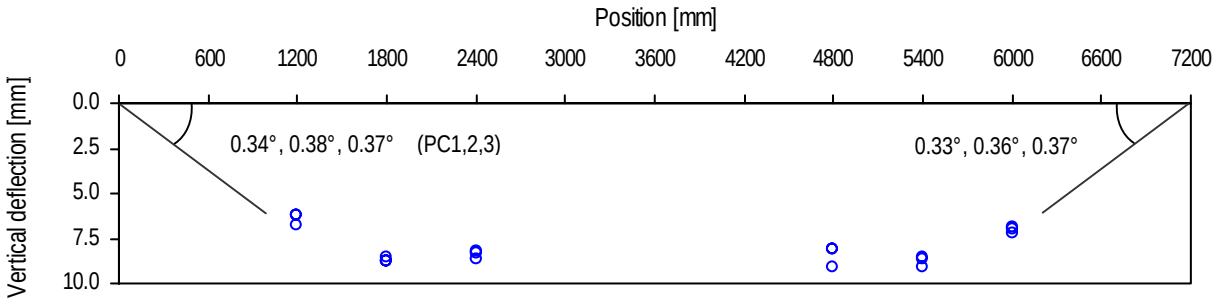

Figure 53 Deflections in longitudinal direction and rotation angles at 50 kN for beams PC1-3

4.2.3 Strain Measurements

Measurements from gages located at the same position on different spans (North and South) and webs (East and West) were not always identical, contrary to measurements of beams PS1-3. This was probably due to the statically indeterminate system which causes some torsion. These variations were also noticed on displacement and load measurements (4.2.1).

As previously observed in simple beams PS1-3, strains measured in the compressive area of the webs were higher than those in the tensile area, thus the neutral axis of the beams was above the centerline. This was attributed to the unequal compression and tension moduli and could also be affected by the stiffness reduction in the compressive area of the cross-section due to secondary deformations.

Strain gages at 200 mm from the mid-support axis showed linear behavior up to 100-110 kN (approximately 70% of failure load), then a slight variation in deformations was observed until failure load due to buckling deformations (Figure 54(a)). Variations were lower than those noticed on beams PS1-3 where gages were located in the flange instead of the webs. Gages in the compressive area (bottom) indicated a strain increase, whereas gages in the tensile area (top) indicated a strain reduction due to the concave buckled half-wavelength (Figure 54(c) section B-B). Figure 54(c) gives a schematic illustration of the observed local deformations on the beams. The strain gages at 200 mm from the loading axis, in the compressive area (top) as well as in the tension area (bottom), indicated a deformation increase certainly due to the mid-support section stiffness reduction (Figure 54(b)).

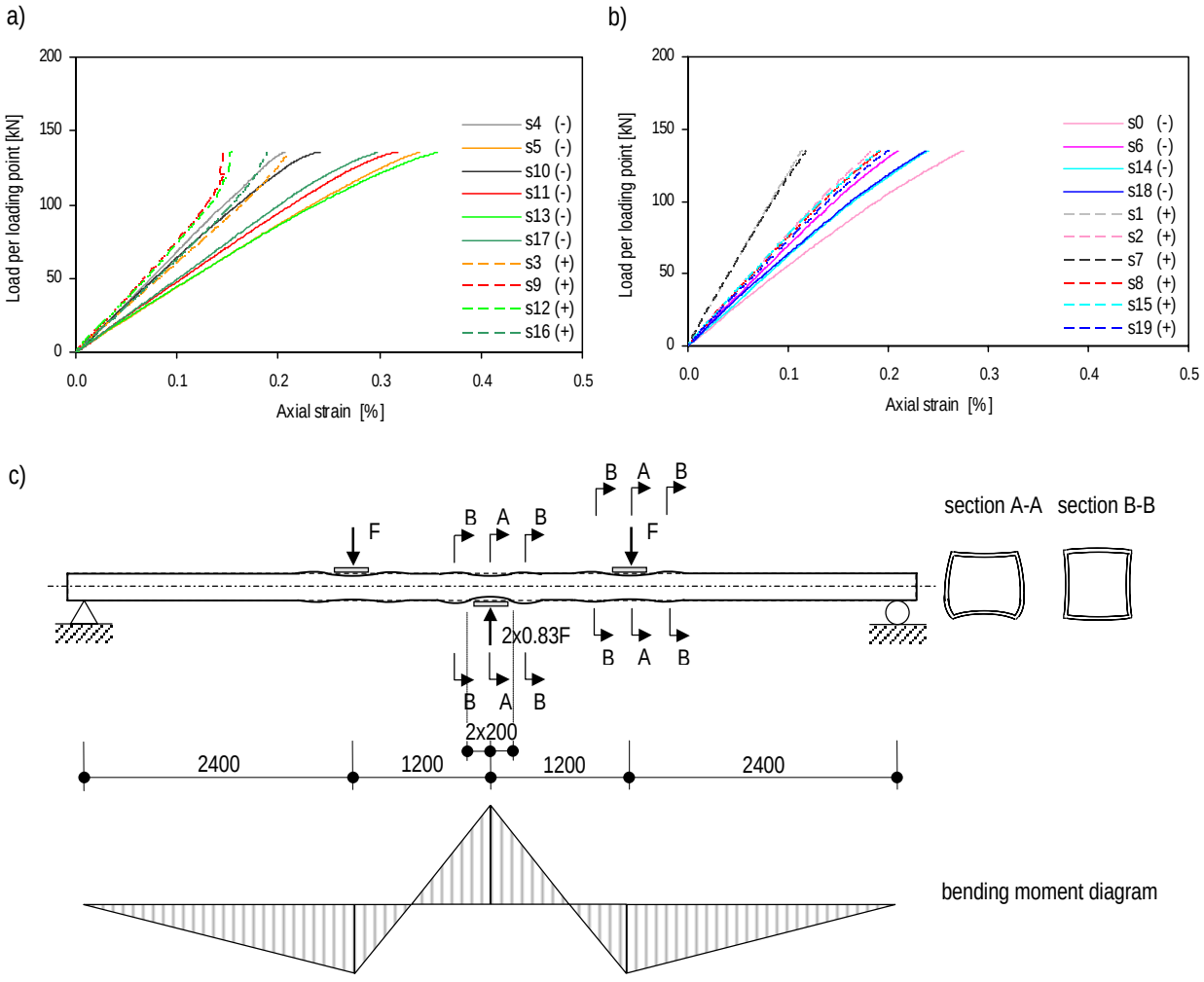

Figure 54 Load-axial strain curves from gages of beam PC2 at 200 mm from (a) mid-support axis, (b) loading axis; (c) Schematic illustration of local deformations

Figure 55 shows strain distribution across the web height at 200 mm from the mid-support axis and loading axis at 50 kN of beams PC1-3 and estimated strain distribution using the beam theory. The bending moments are estimated from the support reactions from FEA calculations. Edge-support reaction and mid-support reaction were 0.15 and 2×0.85 respectively of jack load. The first is lower than measured values (0.16 for PC1 and PC2 and 0.17 for PC3), which explains an estimated strain lower than the measured strain.

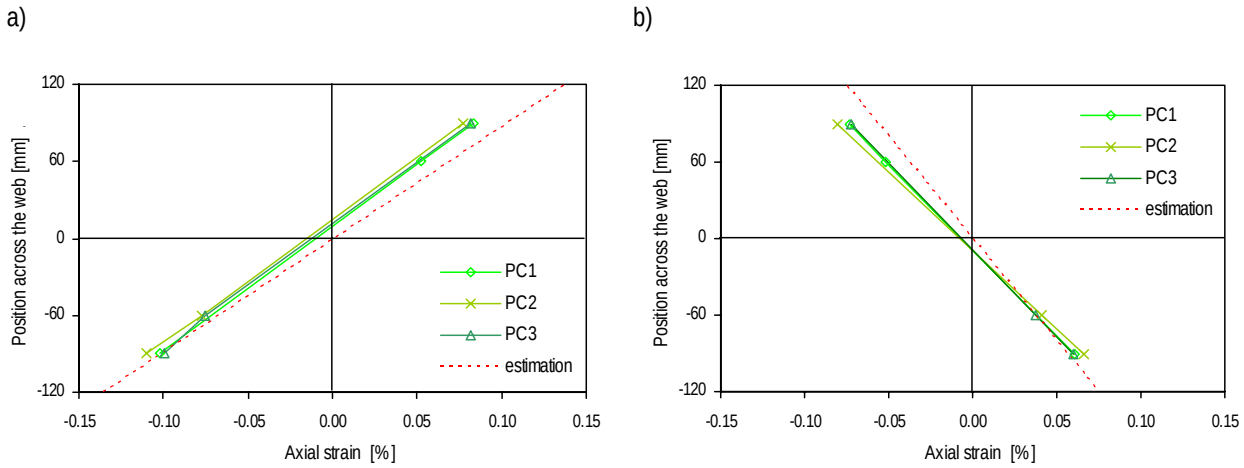

Figure 55 Axial strain distribution across web height at 50 kN for beams PC1-3 at 200 mm from (a) mid-support axis, (b) loading axis

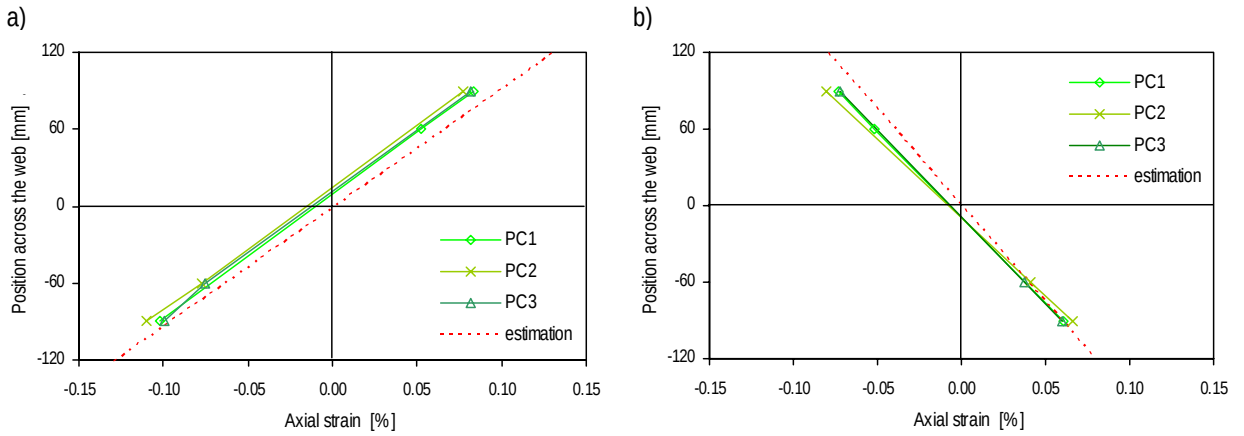

Figure 56 Axial strain distribution across web height at 50 kN for beams PC1-3 at 200 mm from (a) mid-support axis, (b) loading axis

4.3 Elasto-plastic Hinge Beams

4.3.1 Load-Displacement Relationship

Beams were first subjected to seven cycles of loading up to 100-150 kN with a 5 min plateau after loading and unloading. Subsequently they were subjected to loading up to failure. An additional creep experiment was performed on beam PH2. Vertical displacement at the North load-application point (displacement cell of jack) and rotation at mid-support of beam PH2 are plotted in Figures 57(a) and (b) respectively. Load-deflection curves were similar; stiffness remained constant over cycle loads up to 80 kN and slight stiffness reduction was perceived as from the cycle up to 100 kN, while no changes were observed in load-rotation curves. Beam behavior up to approximately 120 kN was linear-elastic but loading and unloading curves were not identical; unloading deflections were higher than loading deflections. The unloading to loading deflection ratio increased during the unloading process; the decrease was 13% at 100 kN, 37% at 50 kN and 76% at 20 kN for beam PH2 (deducting the "plateau value" after the 5 min at 130 kN). Variations for beams PC1-3 were of a similar order of magnitude. As for beams PC1-3, variations were certainly due to the profiles and adhesive viscosity. Beams PH1, PH3 and PH4 exhibited analogous behavior.

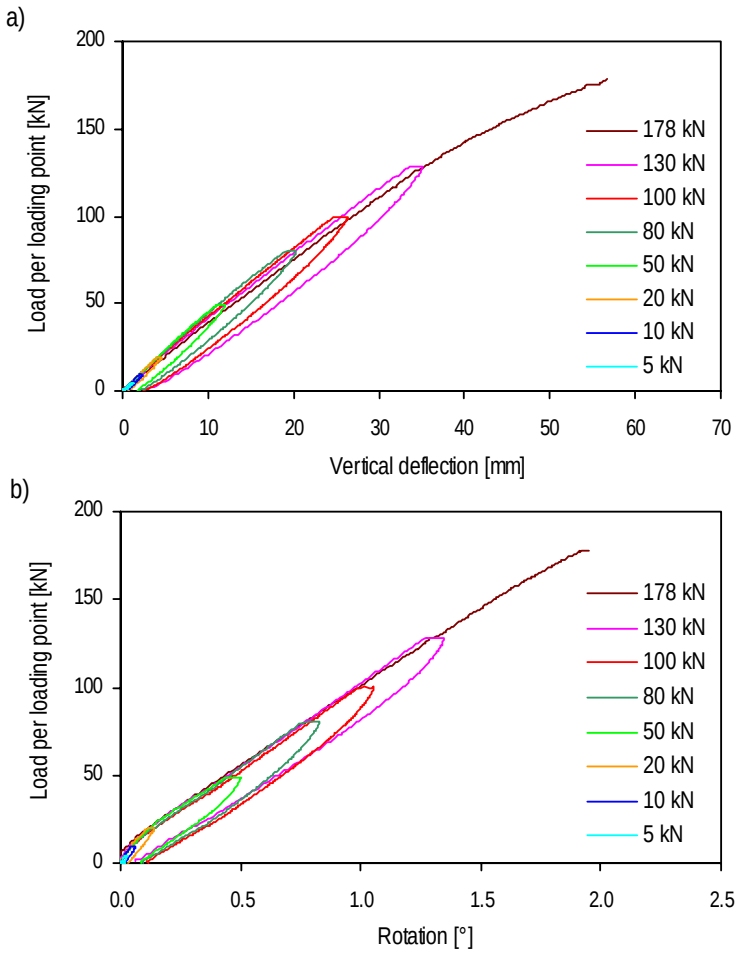

Figure 57 Beam PH2 (a) load-deflection results at North load-application point,(b) load-rotation at mid-span

Load-deflection curves of beams PH1-4 are shown in Figure 58. Average values of the load of the two jacks and deflection in the two loading sections are indicated. The measured values on both spans matched well, variations were at the most 1% for PH1, PH3 and PH4 and 2% for PH2. Failure loads and deflections in the loading- application section of beams PH1-4 are summarized in Table 15.

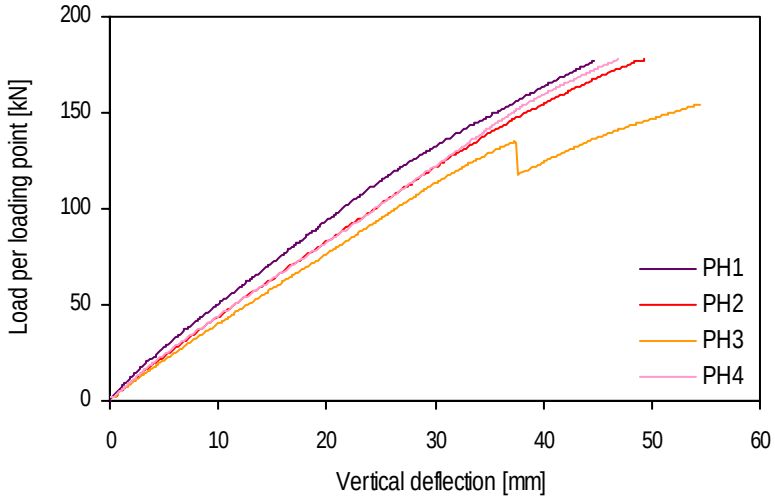

Figure 58 Load-deflection results at loading section for beams PH1-4

4.3.1.1 Bonded Beams PH1 and PH2 (200 mm Overlap)

Beams showed tri-linear behavior. In a first phase up to approximately 125 kN (70% of ultimate failure load), behavior was bilinear, as for the ADP adhesive. In the load range up to approximately 20 kN load per jack, the initial stiffness decreased to 73% and 78% respectively, and subsequently remained constant. In the second phase, exceeding 125 kN, stiffness began to decrease further, coinciding firstly with the onset of buckling of the top flanges and webs below the loading patches and then the bottom flanges and webs at mid-support. Three buckled half-wavelengths developed in loading areas and one above the mid-support (Figure 74). Figure 59 shows the deformed beam PH1 at onset of failure. The negative curvature over the mid-support due to the continuity effect resulting from the bonded joint is clearly visible. Below the South jack (left), the buckling of the web is also visible. Beam failures occurred in the webs below one of the jacks (PH1 South jack, PH2 North jack), similar to what was observed for the simple beams. Longitudinal cracks formed 30 mm below upper edges, the area of the end of the mat overlap. Additional longitudinal cracks formed on the top flange of beam PH2. No damage or failure was observed in the bonded joint. Figure 65(a), (b) and (c) shows the failure modes.

Beam PH1 was slightly stiffer than beam PH2. This could be explained by the different temperature in the laboratory during the manufacturing process or during the experiments (PH1 22°, PH2 28°). The high temperature in the laboratory during the manufacturing process could affect the curing process and joint quality. The adhesive's open time is short (9 min at 23°C, and less at 28°C) and the laminates were probably placed when the adhesive had started to cure. The high temperature in the laboratory during experiments may affect joint stiffness due to adhesive's viscosity.

Failure loads and deflections in the loading section of beams PH1 and PH2 are summarized in Table 15. Failure loads were 180-178 kN and deflections in the loading section were 45-50 mm, corresponding to approximately 1/80-1/74 of span length.

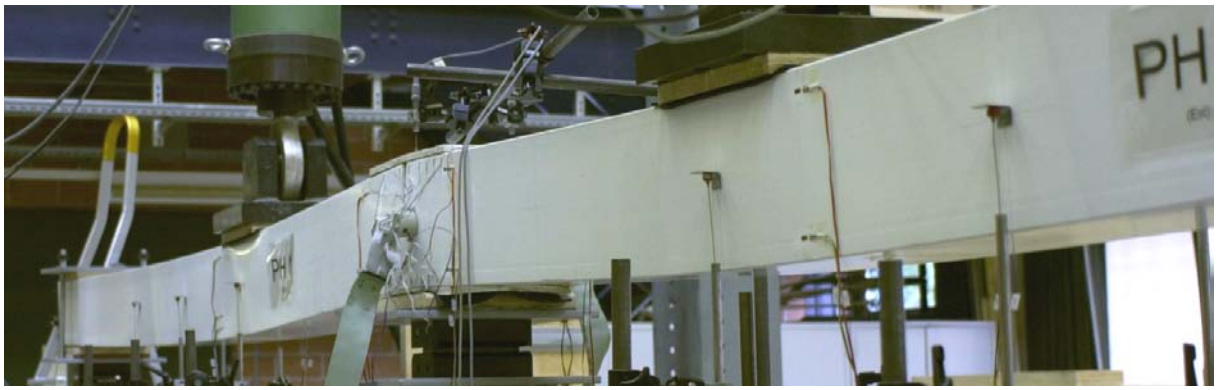

Figure 59 Loading of beam PH1

4.3.1.2 Bonded Beams PH4 (300 mm Overlap)

Beam PH4 showed almost the same load-deflection behavior as beams PH1 and PH2. In the first phase, deflections matched those of beam PH2 while rotations matched those of beam PH1 (see 4.3.2). In the load range up to approximately 25 kN load per jack, the initial stiffness decreased to 78%. In the buckling phase (above 155 kN per jack), stiffness loss was less pronounced than in beams PH1 and PH2. Failure occurred through buckling of the webs below the North jack and was similar to failures of beams PH1 and PH2, in the area of the end of the mat overlap. Figure 65(d) shows the failure mode. The bonded joint remained undamaged.

The failure load and deflection in the loading section of beam PH4 are summarized in Table 15. The failure load was 178 kN and deflection at the loading section 47 mm, corresponding to approximately 1/77 of span length. Both values matched those of beam PH2.

4.3.1.3 Bonded Beams PH3 (100 mm Overlap)

Beam PH3 showed load-deflection analogous to beams PH1, PH2 and PH4 in the first bilinear part up to approximately 120 kN. Stiffness was slightly lower than that of the other beams, as can be seen in Figure 57. In the load range up to approximately 10 kN load per jack, the initial stiffness decreased to 75%. Exceeding 120 kN, stiffness also began to decrease due to the onset of buckling in the compressed flanges and webs below the jacks at first and then at mid-support. At a load of 135 kN, however, the this beam's behavior changed distinctly from that of the others. One part of the adhesive joint in the upper flange failed, as can be seen in Figure 66(a). Failure occurred partially in the outer mat of the pultruded beam and partially in the interface between beam and adhesive. A small area failed in the interface between cover plate and adhesive. The load decreased slightly after this first failure due to the

displacement-controlled piloting. Subsequently, however, the load increased again with increasing deflection. The load-deflection path then progressed in parallel to the simple beams up to an ultimate failure load of 154 kN (see 4.4). Ultimate failure occurred below the North jacks, as was observed for the simple and other bonded beams. The webs buckled and the same horizontal cracks formed, as already described (Figure 66(b)).

Figure 60 shows the widening of the upper gap in the joint between the two beam parts: a) 20 mm at the beginning of the loading, and b) 27 mm at 118 kN load per jack. The shear deformation of the adhesive edges of the overlap can be seen. The visible shear angle is approximately 50° at 118 kN. From a proportional increase up to the failure load of 135 kN, an angle of 57° results.

The first and ultimate failure loads and corresponding maximum deflections at the loading section of beam PH3 are summarized in Table 15. The ultimate failure matched the average value of simple beams and maximum deflection reached 83%.

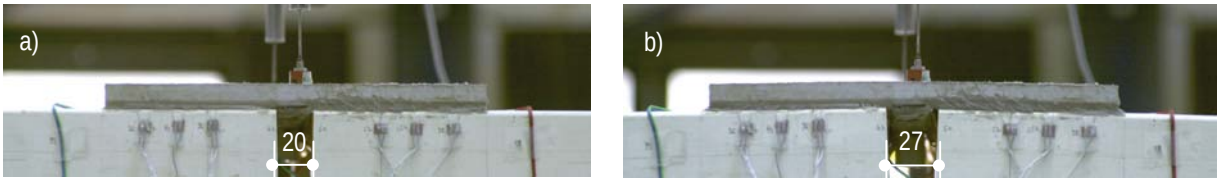

Figure 60 Widening of upper part of bonded joint of beam PH3 (a) initial position, (b) deformation at 118 kN

4.3.1.4 Generalities

Deflections were measured in the centerline with two displacement transducers, one per web, and an average value was calculated (Figures 61(a)-(d)). Displacements measured at mid-support and edge-supports were approximately 9-17% and 2-4% of displacements at load- application points respectively (Figure 62). Thus, they were considered for the actual deflection estimations as illustrated in Figure 49(c). As for beams PC1-3, displacement measured on the top flange at mid-support should be the same as displacement of the beam centerline. Figure 62 shows the support displacements of beam PH2. Comparison of Figures 61(b) and 62 shows that the displacement slope variation at mid-span and third points of beam PH2 corresponds to beam stiffness reduction due to local deformations at mid-support (see 4.2.2).

Displacement transducers of beams PH1-4 exhibited higher displacements in the East than in the West web. Span 1 (North span) was more affected than span 2 (South span) and the variation reached maximum values at the load-application point. These variations were 7% for PH1 and PH3, 9% for PH2 and 12% for PH4. This was probably due to eccentricity on the North loading point. The variation at mid-span and external third point of span 2 was lower than 4-5%. Displacements at mid-span and load application points were quite similar on both spans - variation was lower than 2-3% - but displacements at external third points were rather different; displacement on span 1 was higher than span 2 and variations reached 11% for PH1 and PH3, 12% for PH2 and 10% for PH4. This was also observed on

beams PC2 and PC3, having the same set-up as beams PH1-4. This could explain why failure occurred in three of the four beams, except beam PH1, in span 1. Variations between both webs and both spans indicated slight torsion of the beams.

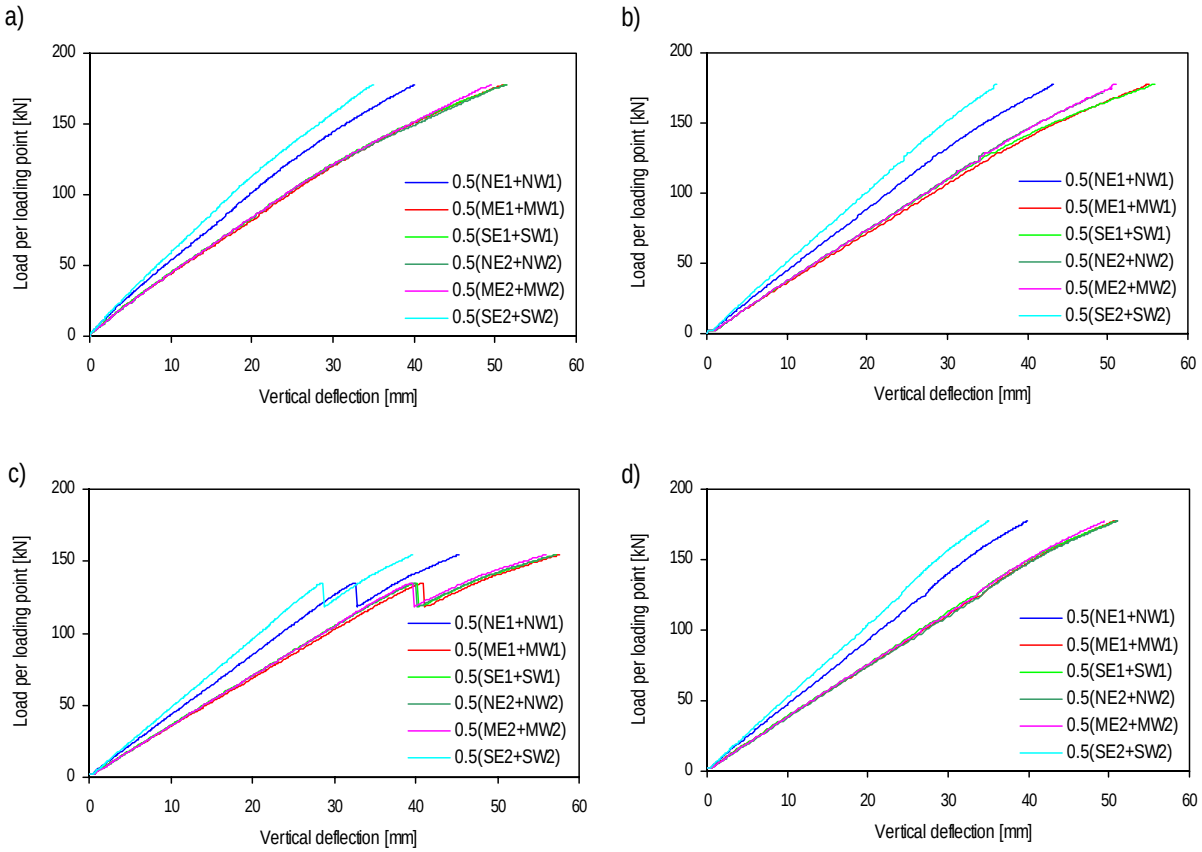

Figure 61 Load-deflection results at mid-span and third points for beams (a) PH1, (b) PH2, (c) PH3, (d) PH4

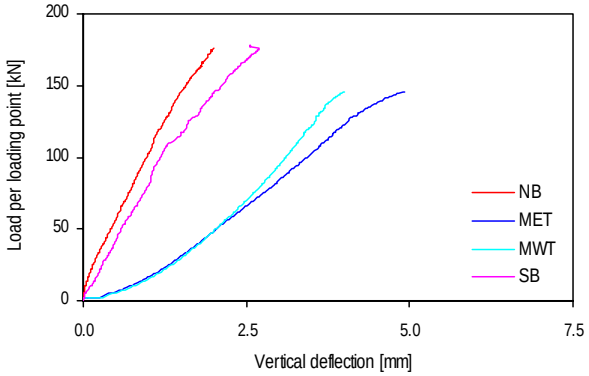

Figure 62 Load-deflection results at edge- and mid-supports for beam PH2

The load is the average value of the loads measured in the two jacks. Variations between jack loads and average values were at the most 2% for PH1 and 1% for PH2, PH3 and PH4. The load sensors installed on the supports confirmed the load measured on the jacks and indicated the asymmetry of the beam and

loading. Variation between the total load of load sensors and total load on jacks was at the most 4% for PH1, 1% for PH2 and 3% for PH3 and PH4 and tended to zero with increasing load. The load at edge-supports and mid-support changed with loading. Figure 63 shows the ratio of bending moment at mid-support to bending moment at loading point of beams PH1-4 from 10 kN up to failure. It also includes the ratio of beam PH2 before the creep experiment. Bending moments are determined from support reactions. The ratio decreased with increasing the load up to approximately 60 kN except for beam PH2 after the creep experiment. The bending moment at mid-support decreased and the bending moment at loading points increased due to the nonlinear behavior of the adhesively-bonded connection at mid-support caused by the highly nonlinear behavior of the adhesive. Subsequently the ratio remained almost constant, indicating a connection with constant stiffness (see 4.3.2). The ratio of beam PH2 after the creep experiment increased with increasing the load up to approximately 30 kN, contrary to the others. Due to creep deformations in the adhesively- bonded connection, the bending moment at mid-support was lower than before the creep experiment and consequently the bending moment at loading points was higher. Subsequently the ratio remained almost constant. Table 14 summarizes the average load at edge- supports and mid-support at the 50-100 kN load interval. Differences between beams PH1 and PH2 are due to the different connection stiffness observed in load-displacement curves. Comparing beams PH2, PH3 and PH4, which were loaded in the same environmental conditions, showed a higher load at mid-support when joint overlap length and therefore connection stiffness were increased. For PH3, load distribution changed after joint failure, i.e. with the static system change. Then the load distribution on supports was similar to simple-beam distribution. Figure 64 shows the evolution of the bending moment diagram of beam PH3. All beams indicated a higher load on the North support than the South support but the maximum variation was 5% for PH1, 2% for PH2 and PH4 and 3% for PH3. Load distribution between East and West load sensors was quite variable at edge-supports; the variation reached 50% of average value, but remained constant at mid-support. This was probably linked to beam torsion. All variations were determined in the 20-100 kN load interval.

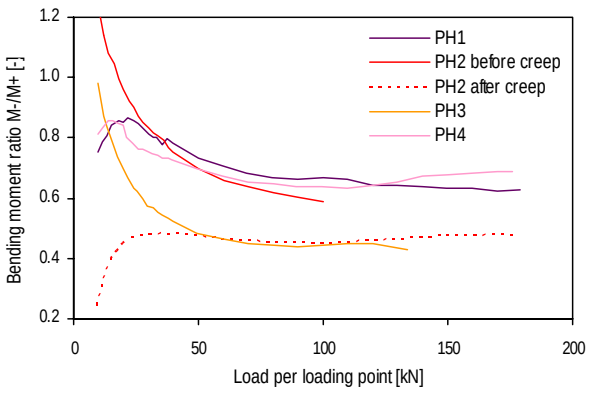

Figure 63 Ratio of bending moment at mid-support to bending moment at loading point of beams PH1-4

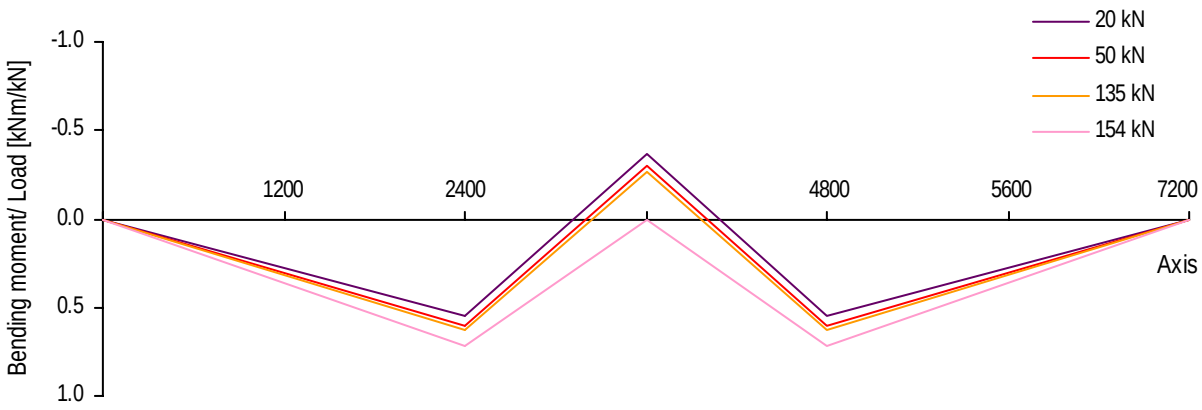

Figure 64 Bending moment diagram of beam PH3

Table 14 Load distribution at supports compared to jack load of beams PH1-4 (50-100 kN)

Beam	Edge supports (-)	Mid-support (-)
PH1	0.23	2×0.77
PH2	0.25	2×0.75
PH3 [1]	0.26	2×0.74
PH3 [2]	0.30	2×0.70
PH4	0.23	2×0.77

[1] before failure in joint
[2] after failure in joint

Table 15 summarizes the ultimate load at failure Q_u, bending moment at failure in the loading section M^+_u, bending moment at failure at the mid-support M^-_u, axial stress at failure in the loading-section σ^+_u, axial stress at failure at mid-support σ^+_u, rotation at failure at mid-supports $\theta_{M,u}$, loading-section deflection at failure $w_{F,u}$ and loading-section deflection to span ratio at failure $w_{F,u}$ /L. The bending moment is estimated from the support reactions at failure load. Axial stresses at flanges were obtained with the elastic flexure formula σ_x=M/I.y where I is the moment of inertia and y is the distance from the neutral axis.

Table 15 Experimental data for beams PH1-4

Beam	Q_u [kN])	M^+_u [kNm]	M^-_u [kNm]	σ^+_b [MPa]	σ^-_b [MPa]	$\theta_{M,u}$ [°]	$w_{F,u}$ [mm]	$w_{F,u}$ /L [-]
PH1	180	99	67	124	83	1.55	45	1/80
PH2	178	107	53	133	66	1.84	50	1/72
PH3 [1]	135	84	36	105	44	1.52	38	1/95
[2]	154	111	-	138	-	2.21	55	1/65
PH4	178	98	66	122	82	1.42	47	1/77

[1] at the joint failure
[2] at the span failure

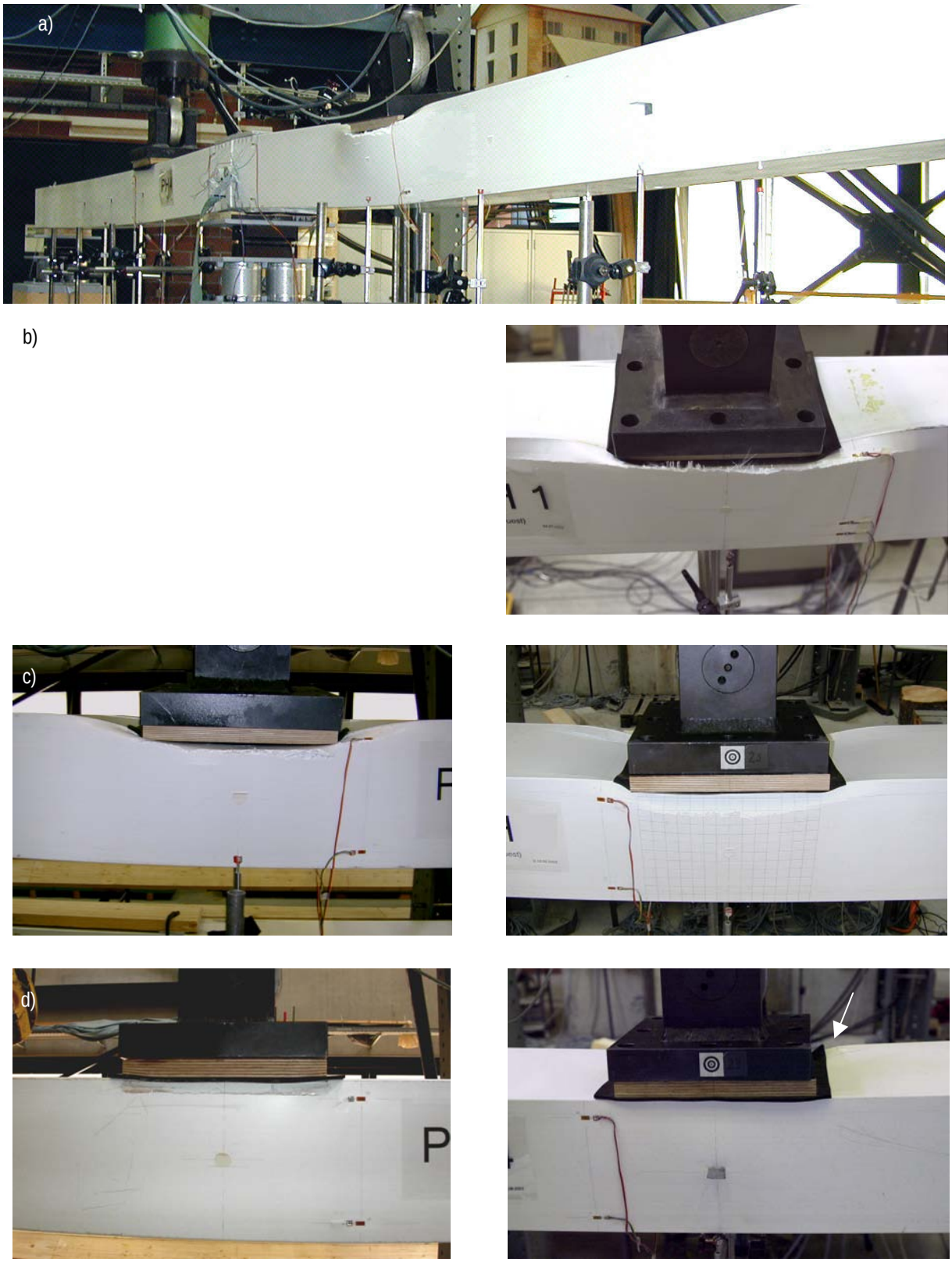

Figure 65 Failure of beams PH1, PH2 and PH4 (a) global view of PH2; East/West sides (b) PH1, (c) PH2, (d) PH4

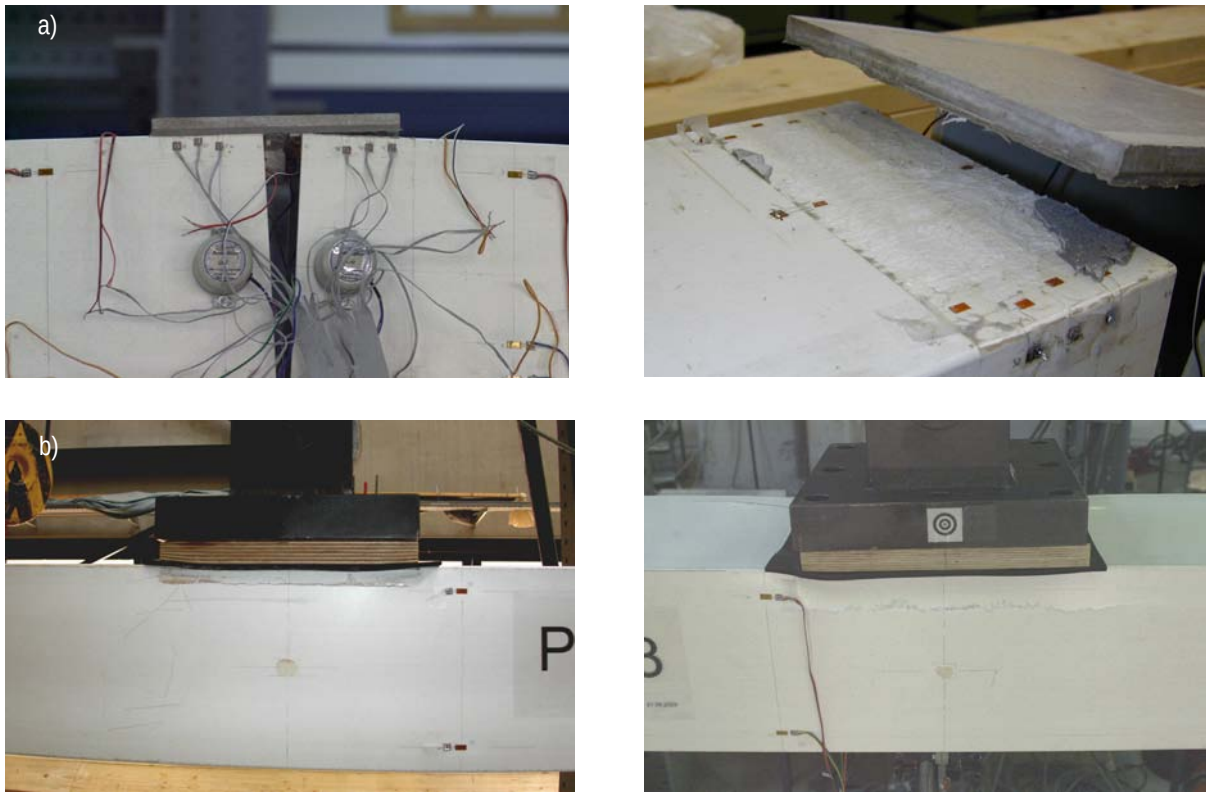

Figure 66 Failure of beam PH3 (a) joint failure, (b) East and West sides of span failure

4.3.2 Load-Rotation and Bending Moment-Rotations Relationships

Figure 67 shows the measured load-rotation behavior on both spans of beams PH1-4 at mid-support. The average values of the two jacks and the rotations in the two webs are indicated. The two sides of the connection had rotations which were quite similar but not as similar as for beams PC1-3, probably due to geometrical dissymmetry. The variation between East and West measurements up to 100 kN is considerable and reached 20% for PH1 whereas variation between North and South measurements is lower than 2% for PH1, 7% for PH2, 4% for PH3 and 10% for PH4.

Figure 68 compares the measured load-rotation behavior of beams PH1-4 at mid-support. The average values of the two jacks and the rotations in the two spans are indicated. The rotation curves of beams PH1, PH2 and PH3 showed the same bilinear behavior as the deflection curves in the first phase. However, no stiffness decrease in the second phase due to buckling was detected. As mentioned in 4.3.1, the rotations of beam PH3 matched those of PH1. The rotation curve of beam PH3 had the same shape as the deflection curve (Figure 58). After the first failure, the slope changed and the curve developed in parallel to the simple beams (see 4.4).

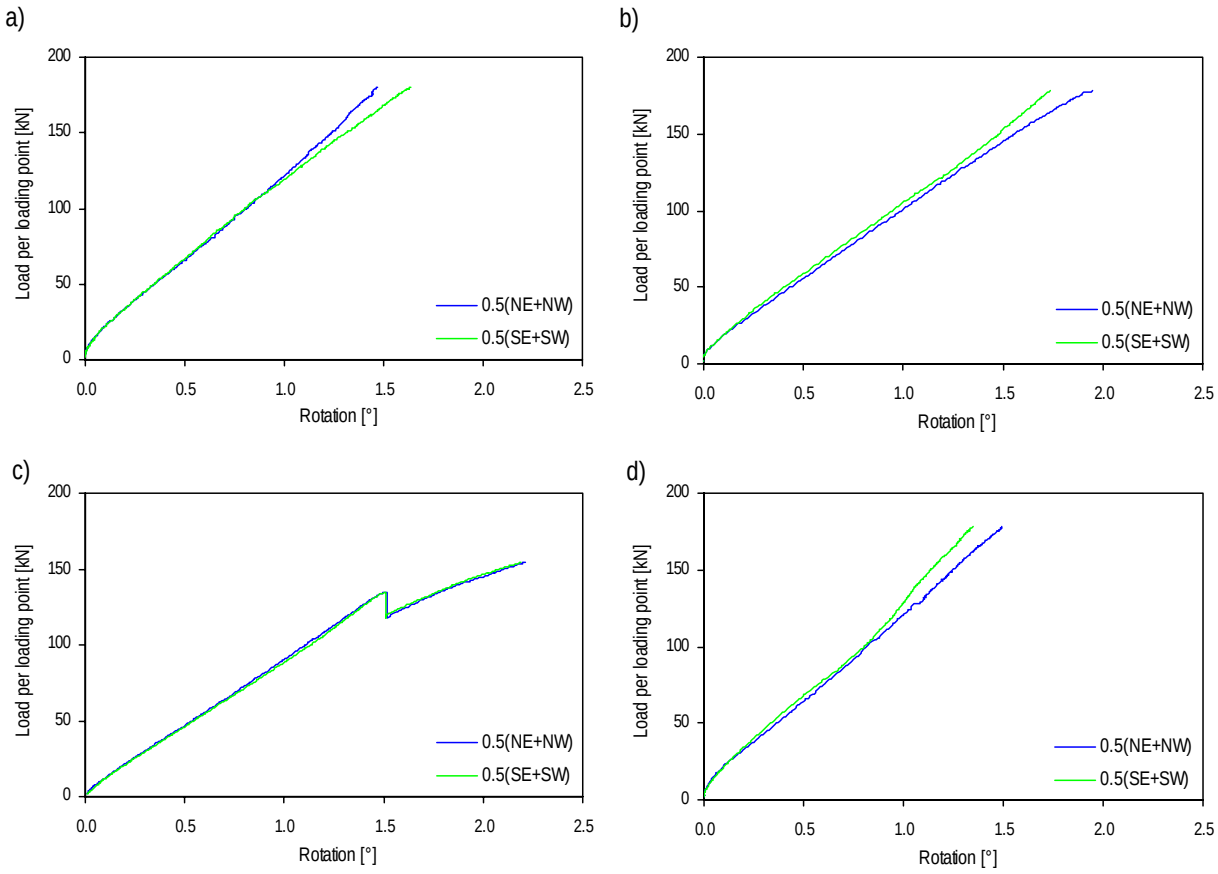

Figure 67 Load-rotation results at mid-support for beams (a) PH1,(b) PH2, (c) PH3, (d) PH4

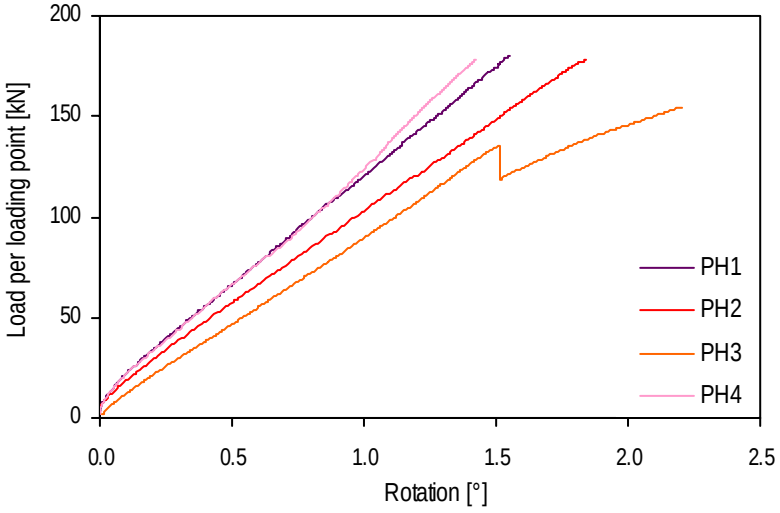

Figure 68 Load-rotation results at mid-support for beams PH1-4

Figure 69(a) compares the corresponding bending moment-rotation curves at mid-support of beams PH1-4. The bending moment at mid-support is computed as follows:

$$M = R \cdot 3.6 - Q \cdot 1.2 \tag{14}$$

R is the load at the edge-support (Table14) and F the load applied per jack. Connection stiffness is related to bending moment and rotation as follows:

$$k = \frac{M}{\theta} \tag{15}$$

The rotations of beams PH1, PH2 and PH4 were null for a bending-moment level up to M_1, then the slope of the bending moment-rotation curves decreased progressively before reaching a constant value at M_2. Connections were initially rigid, then exhibited gradual stiffness reduction until a constant stiffness was maintained. Beam PH3, with the smallest overlap length, did not exhibit the first step of no rotation but the slope of the bending moment-rotation curves also decreased gradually until reaching a constant value at M_2. A simplified curve is presented in Figure 69(b). It consists of three lines and is defined by two bending moments, M_1 and M_2, and two connection stiffnesses, k_1 and k_2. Values of connection stiffness k_1 are calculated from the secant through the bending-moment interval M_1-M_2. Values of connection stiffness k_2 re calculated from the secant through the bending-moment interval 10-30 kNm, where the curves are linear. Table 16 summarizes these four parameters and the corresponding applied loads.

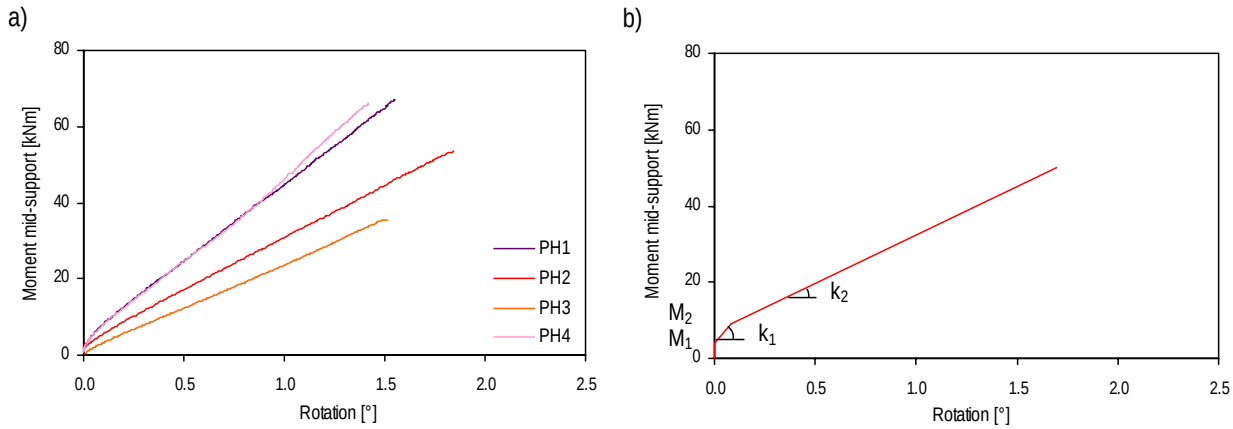

Figure 69 Bending moment-rotation curve at mid-support for beams PH1-4 (a) from experiments, (b) simplified model

Table 16 Parameters of the simplified bending moment-rotation model of beams PH1-4

Beam	Q_1 [kN]	Q_2 [kN]	M_1 [kNm]	M_2 [kNm]	k_1 [kNm/°]	k_2 [kNm/°]
PH1	5	24	1.9	8.9	62	40
PH2	5	25	1.5	7.5	38	33
PH3	0	16	0	4.2	28	23
PH4	4	23	1.5	8.6	61	40

Figure 70 illustrates deflections along mid-span and third points and mid-support rotations at 50 kN load level.

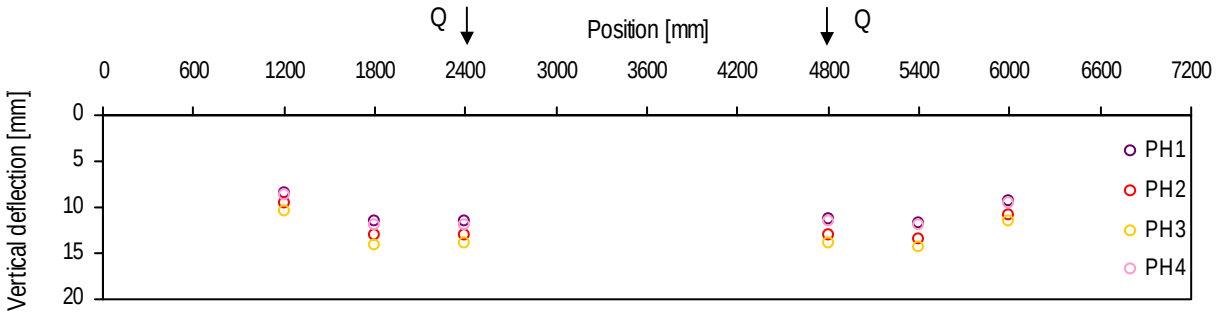

Figure 70 Deflections in longitudinal direction and rotation angles at 50 kN load level for beams PH1-4

4.3.3 Strain Measurements

Measurements from gages located at the same positions on different spans (North and South) and webs (East and West) were dissimilar due to torsion effects caused by the static indeterminate system, loading axis eccentricity and the geometrical dissymmetry of the beams. Variations were predominant at mid-supports. The strains measured in the compressive area of the webs were higher than those in the tensile area as previously noticed in beams PS1-3 and PC1-3.

Strain gages at 200 mm from mid-supports indicated irregular measurements caused by the load transfer from beam elements to laminates via the adhesively-bonded joints (Figures 71(a), (c), (e) and 72(a)). In this transition area measurement interpretation is not easy but provides some qualitative information. A slight variation in deformations was observed up to failure load due to buckling deformations. Variations were similar to those noticed on beams PC1-3 and lower than those noticed on beams PS1-3 where gages were located on the flange instead of the webs. Gages in the compressive area (bottom) indicated a strain increase whereas gages in the tensile area (top) indicated a strain reduction due to the concave buckled half-wavelength (Figure 74 section B-B). Figure 74 gives a schematic illustration of the local deformations observed on beams PH1-4.

Strain gages at 200 mm from mid-support of beam PH3 showed the change in the static system after joint failure (Figure 72(a)). The gages initially deformed in compression now deformed in tension and vice versa.

Strain gages at 200 mm from the loading axis showed the same tri-linear behavior as deflection curves (Figures 71(b), (d), (f) and 72(b)). As previously noticed, the second phase coincided with buckling of the web. Compression (top) strains increased while tension (bottom) strains decreased or remained constant as a result of the concave deformation.

The bending moment diagrams calculated from the support reactions (Figure 88(c)) indicated higher bending moments and therefore higher strains at loading points than mid-support. This agrees with strain measurements but the bending moment ratio at gage locations does not agree with the measured

strain ratio. Figure 73 shows strain distribution across the web height at 200 mm from the mid-support axis and loading axis at 50 kN of beams PH1-4 and estimated strain distribution using the beam theory. The strains close to mid-supports were lower than those estimated with the bending moment diagram and inversely for strains close to the loading patch. Thus, the bending moment at loading sections estimated from the measured supporting forces is slightly underestimated.

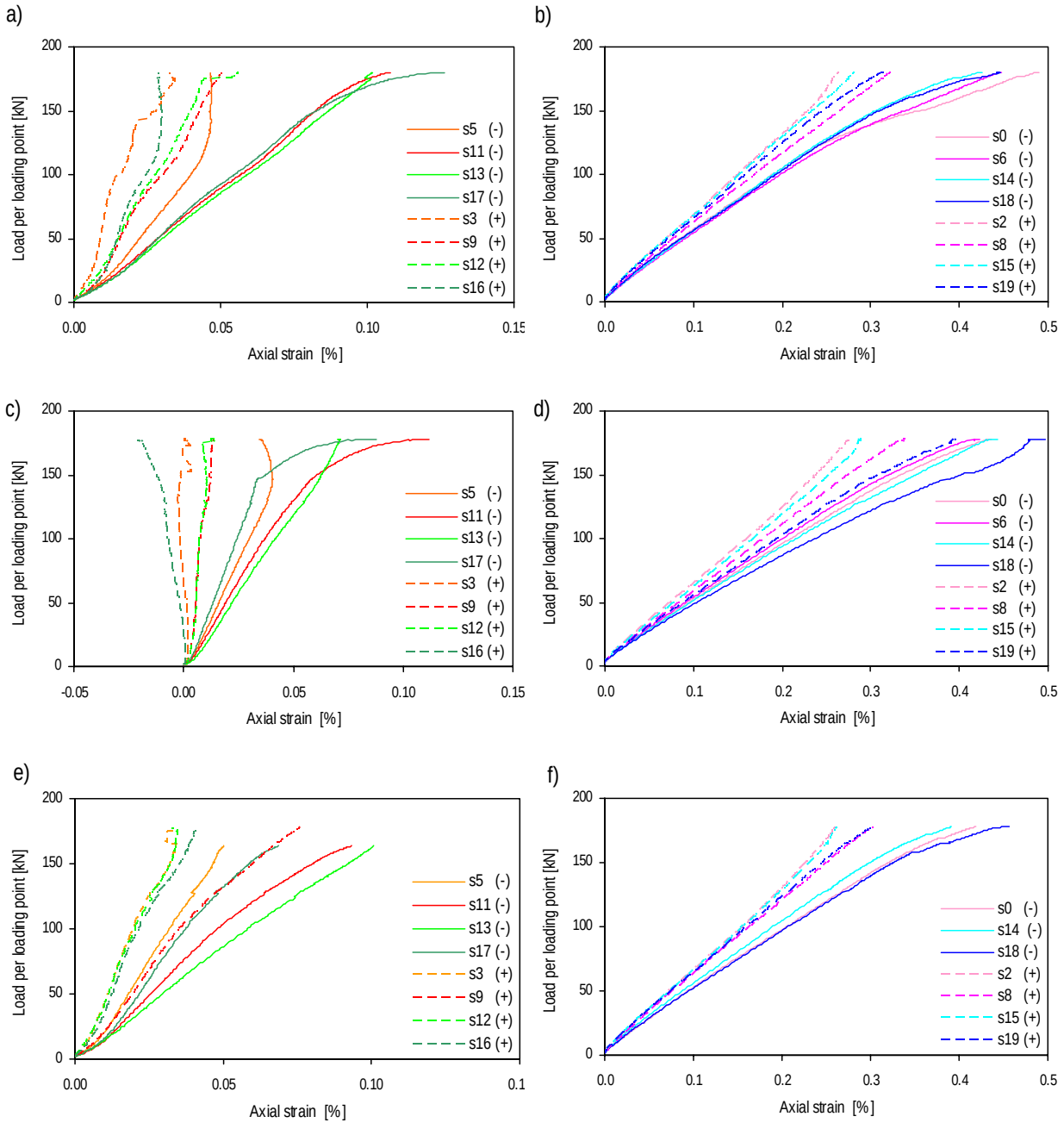

Figure 71 Load-axial strain curves of gages at 200 mm from mid-support axis (a) PH1, (c) PH2, (e) PH4; Load-axial strain curves of gages at 200 mm from loading axis (b) PH1, (d) PH2, (f) PH4

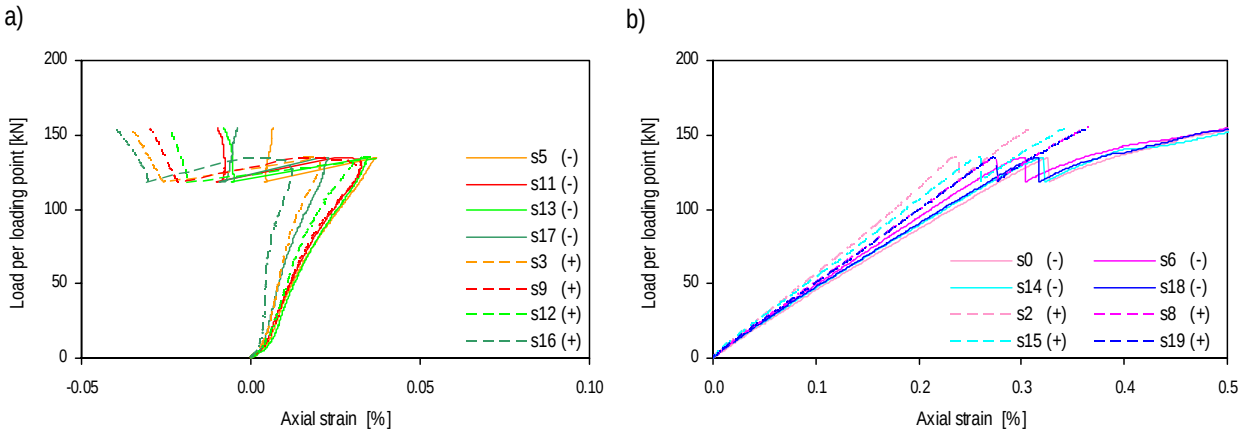

Figure 72 Load-axial strain curves of gages at 200 mm from mid-support axis, (b) loading axis beam PH3

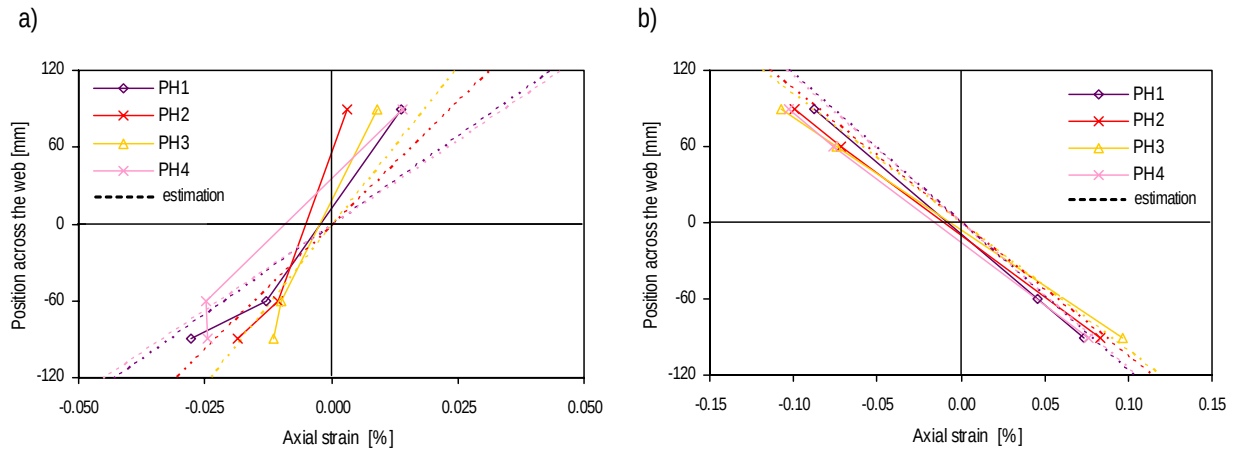

Figure 73 Axial strain distribution along web height at 50 kN for beams PH1-4 at 200 mm from mid-support axis, (b) loading axis

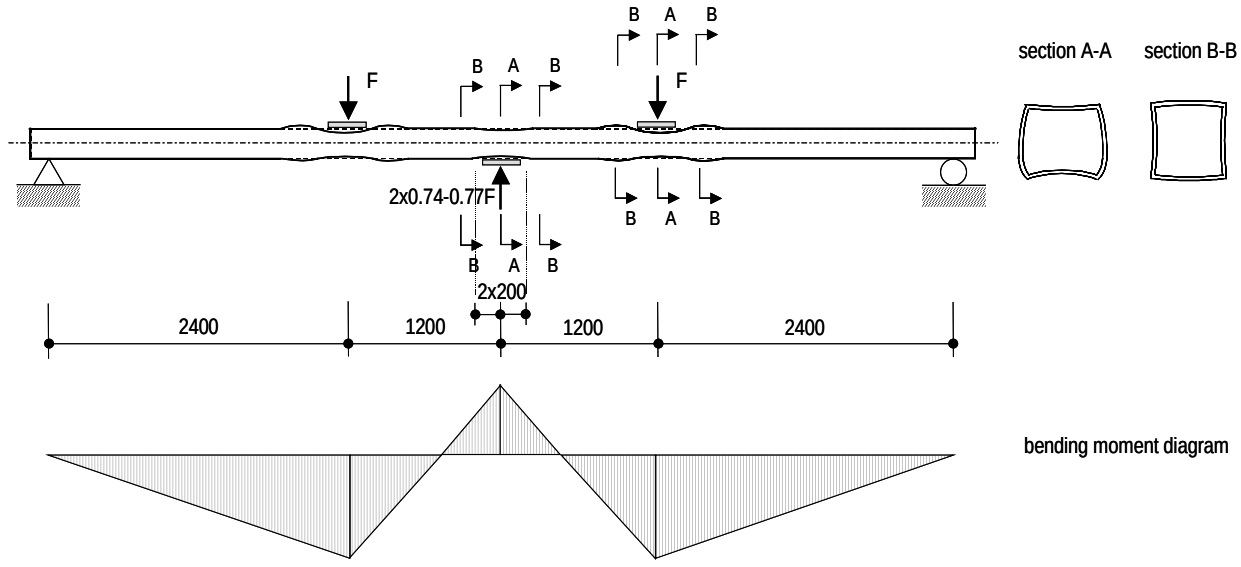

Figure 74 Schematic illustration of local deformations

4.3.4 Strain Measurements in the Adhesively Bonded Connection

Gages installed on the beam flanges measured axial strains along the overlap length and indicated load transfer in the joints (Figure 75). Figures 77-80 (a)-(d) show load-axial strain curves for beams PH1-4 respectively in the four joints that make up the connection. Some axial strain curves were bilinear while others were linear. The slopes changed at approximately 80 kN for PH1 and PH2, 70 kN for PH3 and 100 kN for PH4, so they coincided with stiffness reduction observed in deflection and rotations curves. Figures 77-80 (e)-(f) show axial strain along the upper (in tension) and bottom (in compression) strap joints for beams PH1-4 respectively. Since measurements in the lower joints were irregular due to the high compression stresses above mid-support they were not useful.

Figure 75 shows the treated measurements of axial strains along the two upper strap joints (in tension) of beams PH1-4. Symbols represent average values from the edge gages. Measurements of gages installed in the middle of the flanges were not taken into account since they were highly influenced by the flanges' concave deformations.

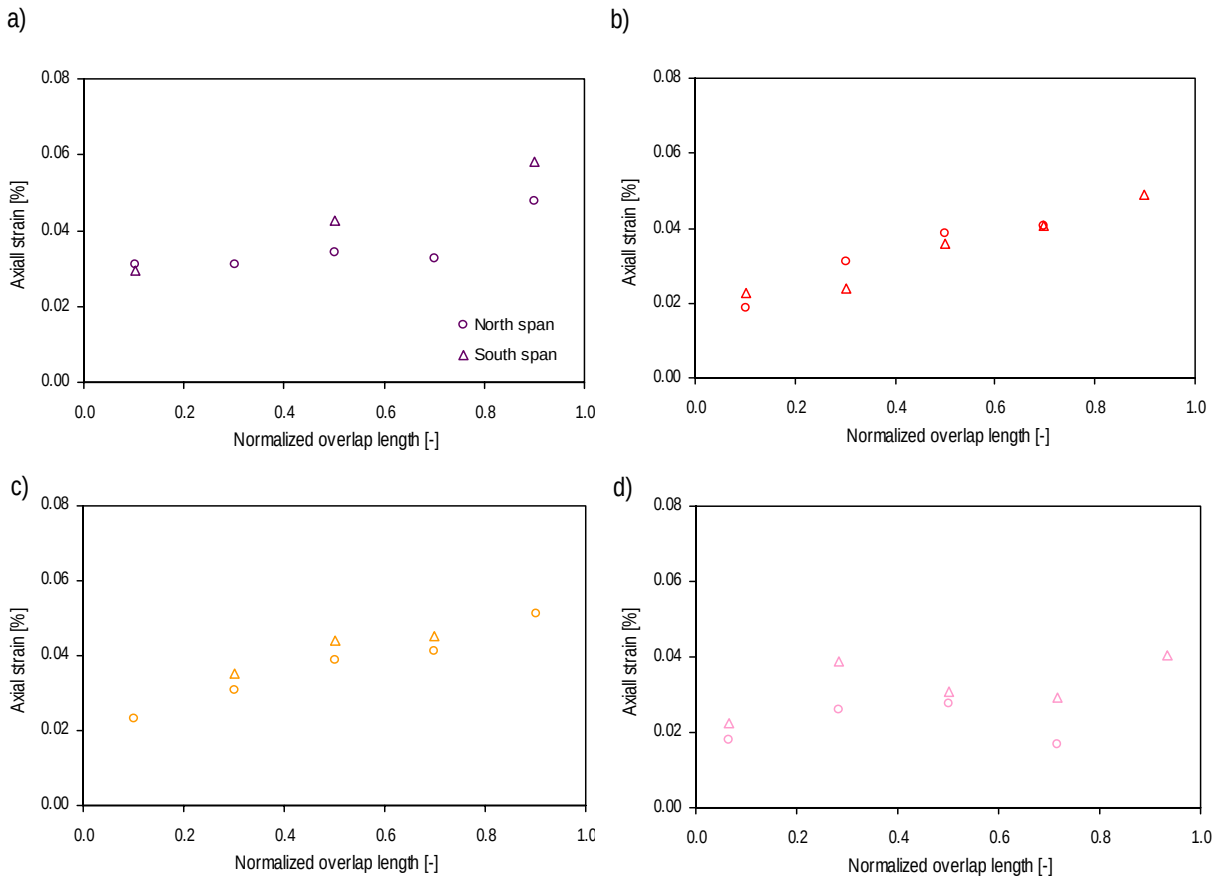

Figure 75 Axial strain distributions in upper adhesive joints in both spans of beams (a) PH1, (b) PH2, (c) PH3 and (d) PH4 at 50 kN per jack

Figure 76 shows the average values of axial strains along the two upper strap joints. Strain distribution was nearly linear along the major part of the overlap. Strains increased nonlinearly only in the first and last 20 mm for beams PH1, PH2 and PH4 and 10 mm for beam PH3. Linear least-square fits are also shown. A global fit is determined for beams PH1 and PH2. The slope of the fitted straight lines decreases with increasing overlap.

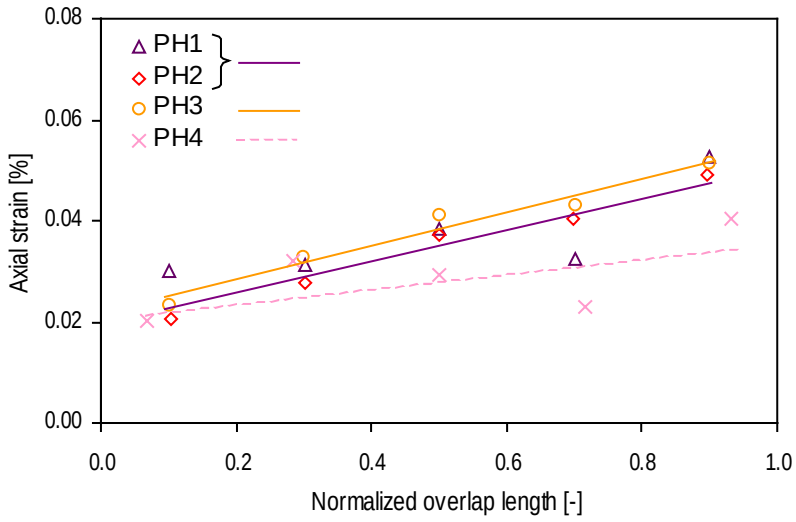

Figure 76 Axial strain distributions in upper adhesive joints of beams PH1-4 at load of 50 kN per jack

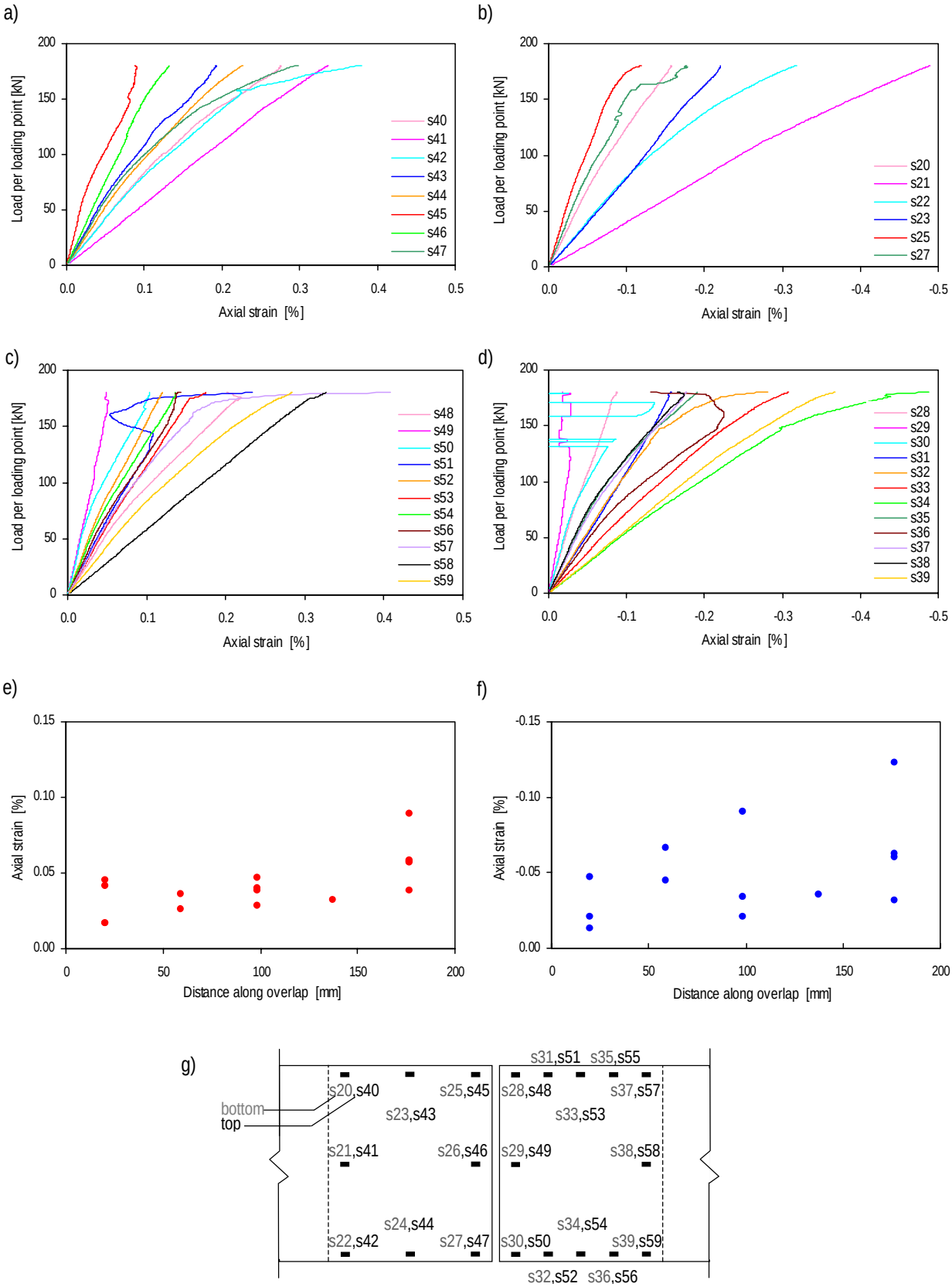

Figure 77 Load-axial strain curves for beam PH1 in top joint (a) North span, (c) South span; in bottom joint (b) North span, (d) South span; Axial strain along overlap length at 50 kN in (e) top joint, (f) bottom joint; (g) gage locations

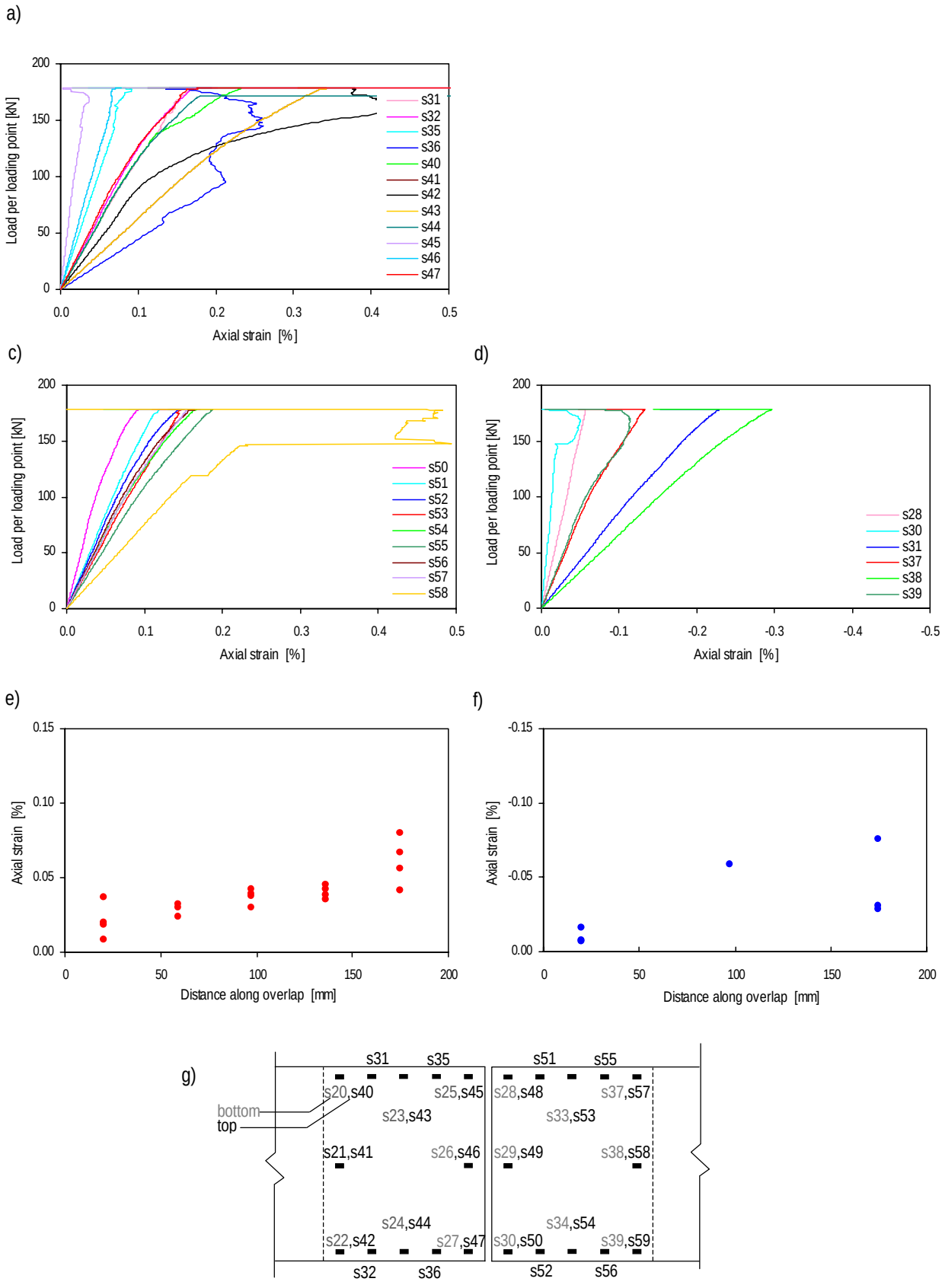

Figure 78 Load-axial strain curves for beam PH2 in top joint (a) North span, (c) South span; in bottom joint (d) South span; Axial strain along overlap length at 50 kN in (e) top joint, (f) bottom joint; (g) gage locations

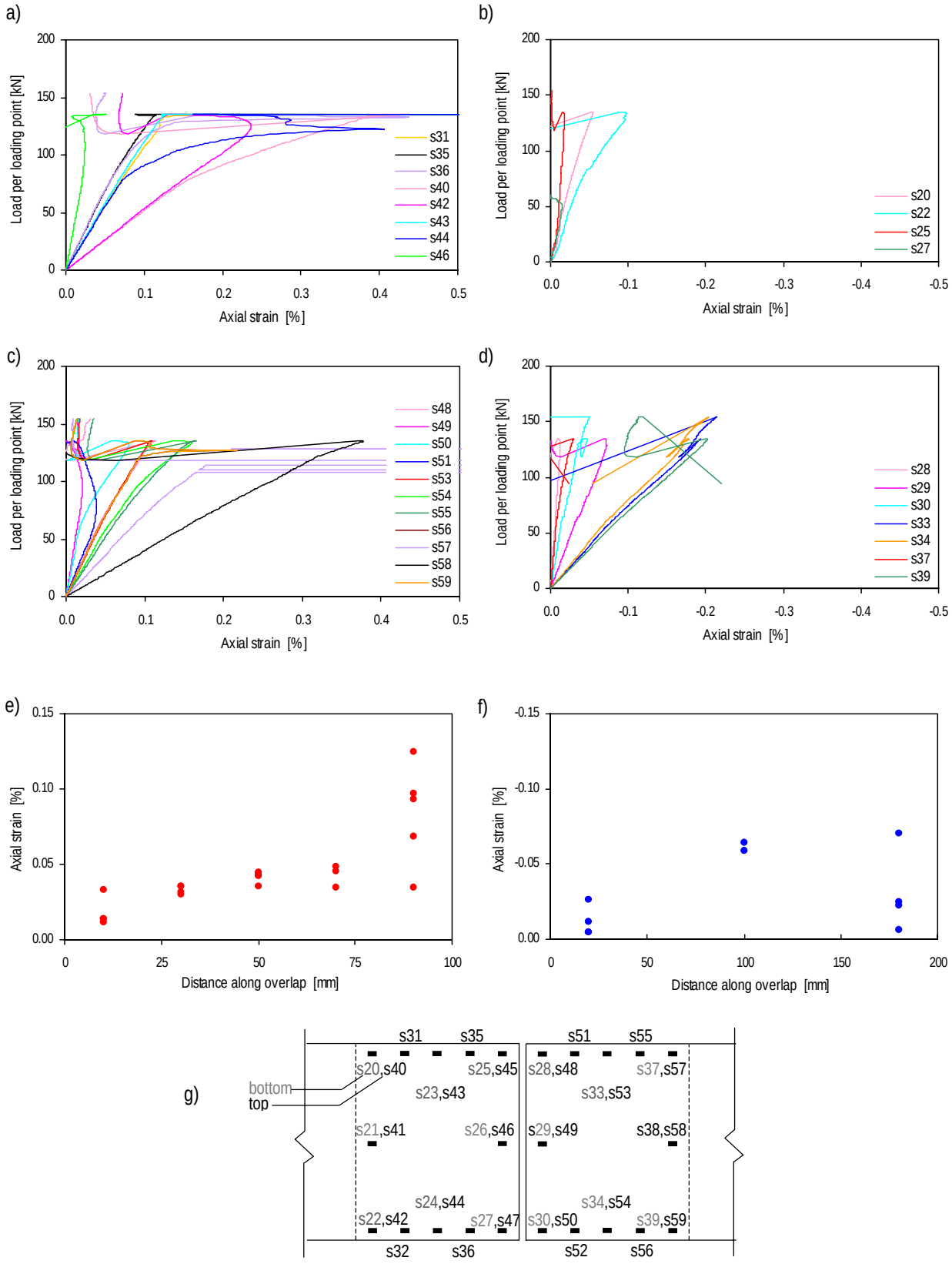

Figure 79 Load-axial strain curves for beam PH3 in top joint (a) North span,(c) South span; in bottom joint (b) North span,(d) South span; Axial strain along overlap length at 50 kN in (e) top joint, (f) bottom joint; (g) gage locations

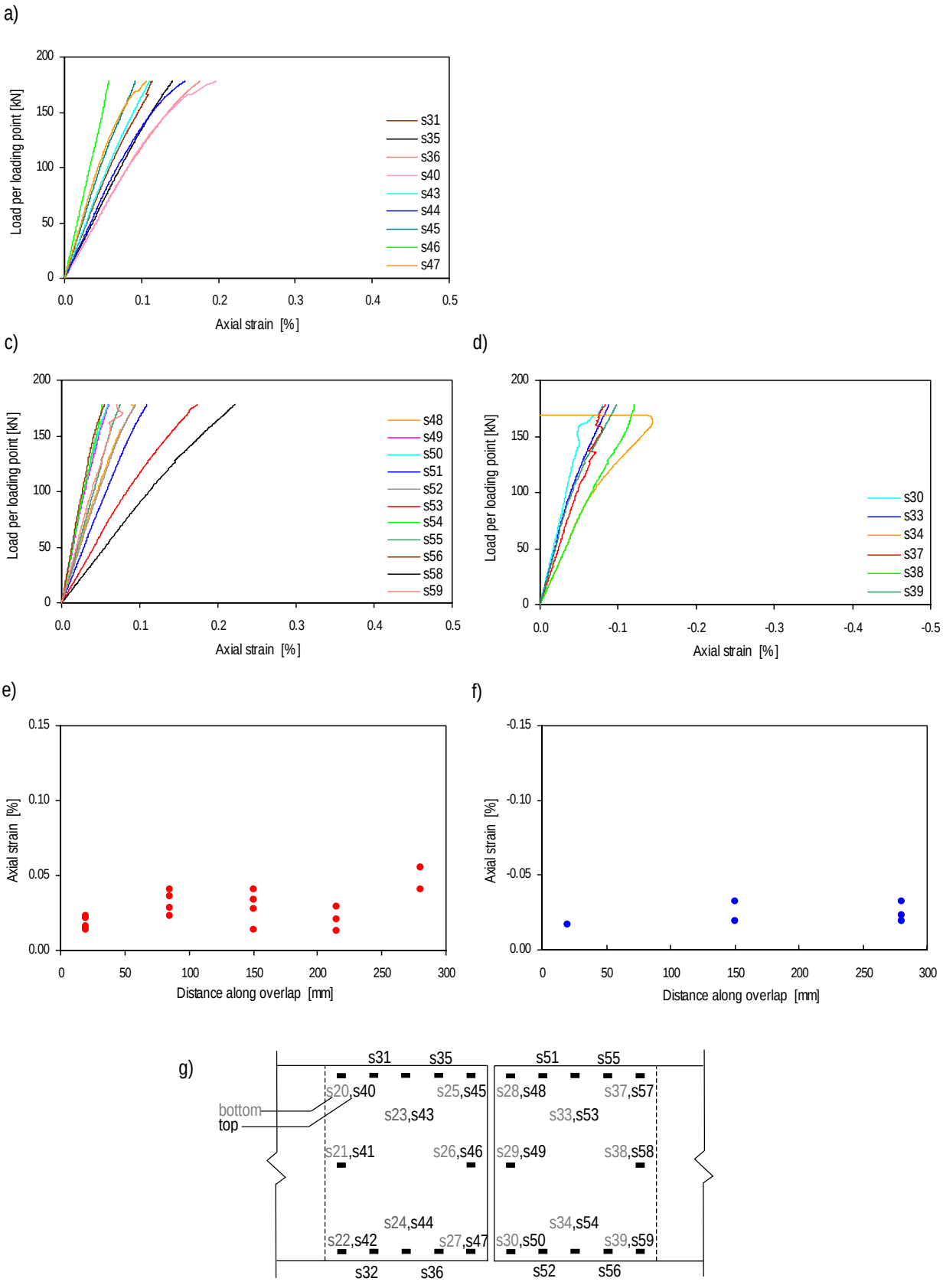

Figure 80 Load-axial strain curves for beam PH4 in the top joint (a) North span, (c) South span; in the bottom joint (d) South span; Axial strain along the overlap length at 50 kN in the (e) top joint, (f) bottom joint; (g) Gages locations

4.3.5 Creep Effect

Beam PH2 was subjected to 7 days of creep loading, as already described. Figure 82(a) and (b) illustrates the load history and deflection-time curve at loading points during the creep experiment. A zoom of the first hour and last two hours of the creep experiment is shown in Figure 82(c) and (d) and Figure 82(e) and (f) respectively. The loading curve up to 9 mm deflection is not totally linear due to manually-driven loading. Subjected to constant loads, maximum deflection increased from 9.1 mm to 11.6 mm (approximately 25%) during the 7 days. 70% of the increase occurred within the first 5 minutes. Table 17 summarizes deflections and corresponding variations compared to immediate deflections at 5 minutes and 7 days after the loading. Figure 81 shows the time-dependent deflection variation compared with initial deflection. Both curves are approximated with a linear least-square fit.

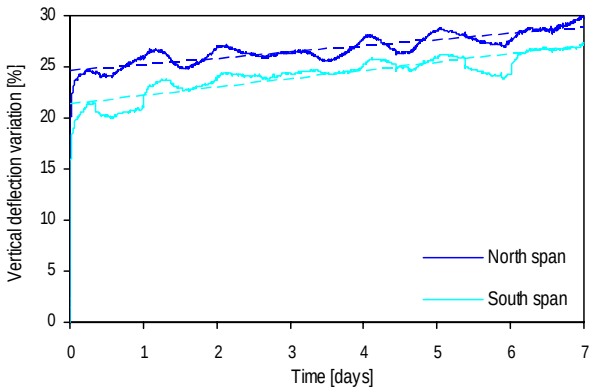

Figure 81 Creep experiment: Time-dependent deflection variation compared with initial deflection

Table 17 Deflection at loading sections and variation compared with initial deflection

Time	North span		South span		Average	
	Deflection (mm)	Variation (%)	Deflection (mm)	Variation (%)	Deflection (mm)	Variation (%)
0 min	9.1	-	9.1	-	9.1	-
5 min	11.0	+20.9	10.6	+16.5	10.8	+18.7
7 days	11.8	+28.8	11.6	+27.5	11.7	+28.6

At the end of the unloading phase, at approximately 3 kN per jack, the beam lifted and was not in contact with the mid-support as shown in Figure 83. At this time the static system changed and became a simple beam with a 7.2 m span length. The corresponding estimated deflection at loading sections, disregarding shear deformations, is approximately 6 mm. Since this value is lower than measurements, other effects must be taken in account. Deformations after the creep experiment are schematically illustrated in Figure 84.

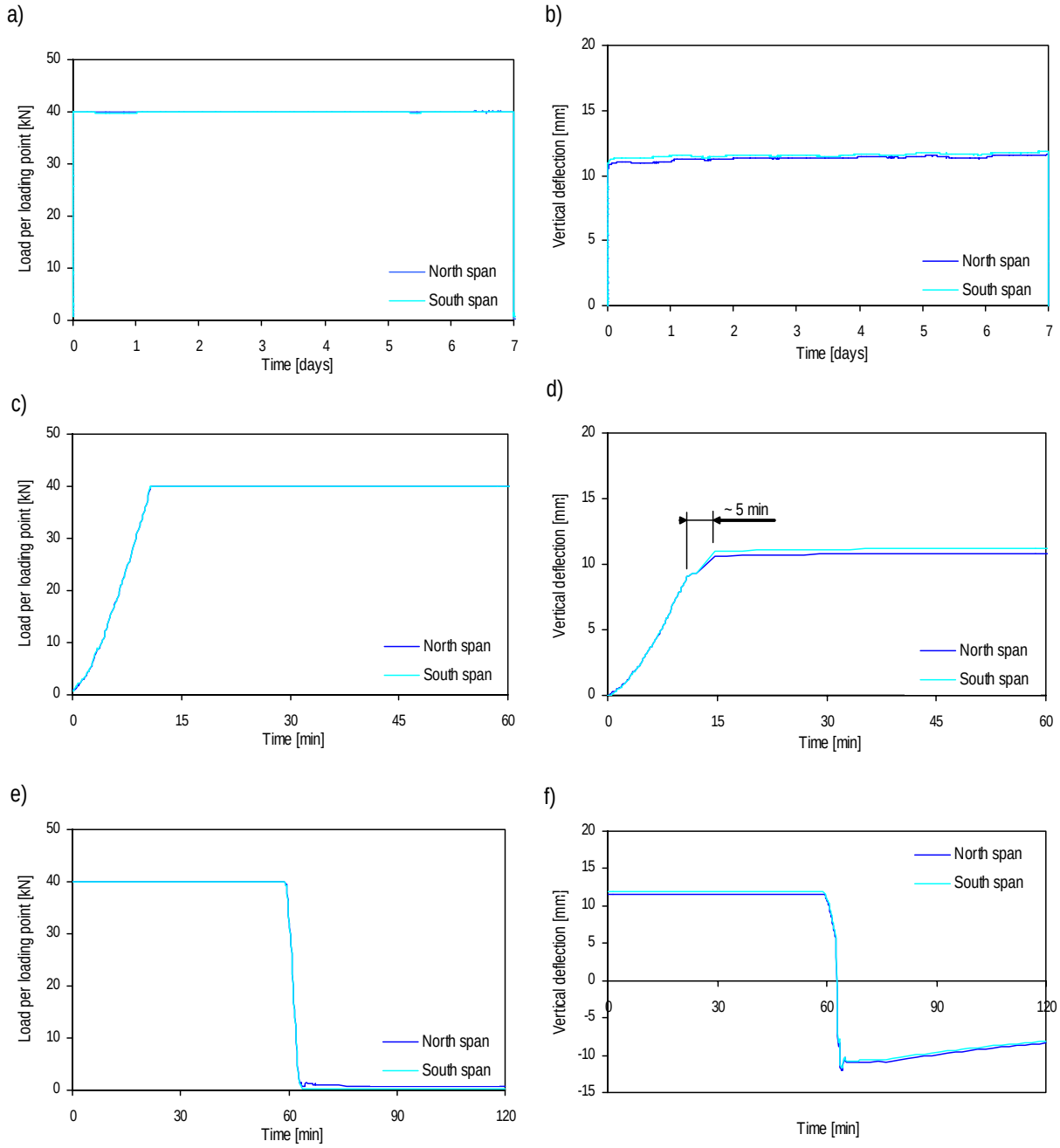

Figure 82 Creep experiment: Load history (a) global, (c) first hour, (e) last two hours; Time-dependent deflection behavior (b) global, (d) first hour, (f) last two hours

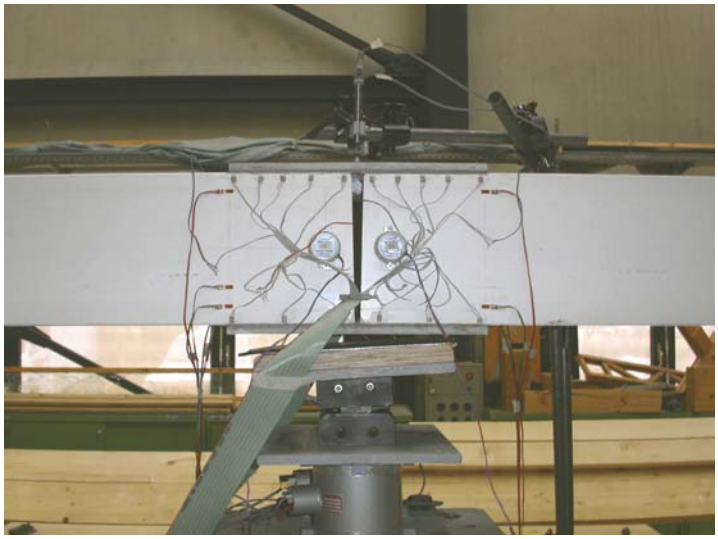

Figure 83 Mid-support position after creep experiment

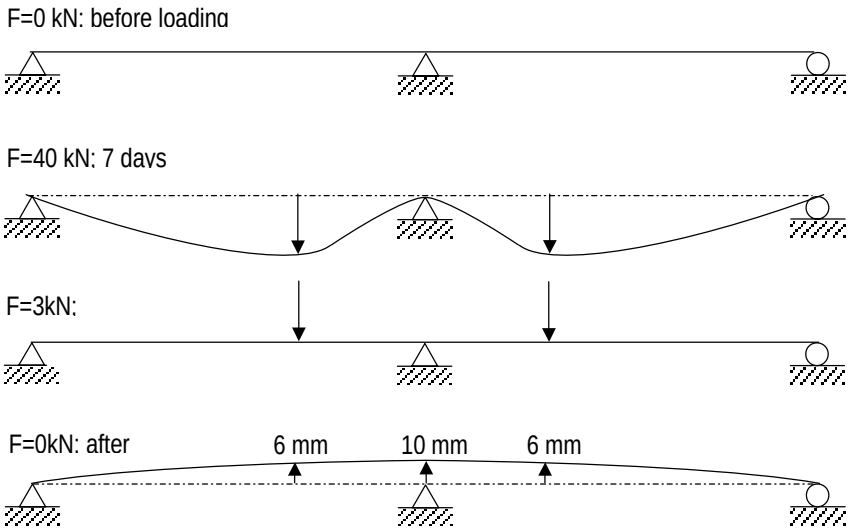

Figure 84 Schematic illustration of beam PH2 deformations after creep experiment

After the unloading of the creep experiment, a second loading cycle up to 100 kN was carried out in order to compare measurements with those before the creep experiment (see 3.3). The beam was first placed back into the initial position, in contact with the mid-support, and then loaded as usual. Figure 85(a) and (b) and Figures 85(c) and (d) show load-deflection and load-rotation respectively up to 100 kN before and after the creep experiment. No differences were observed, indicating some creep effects.

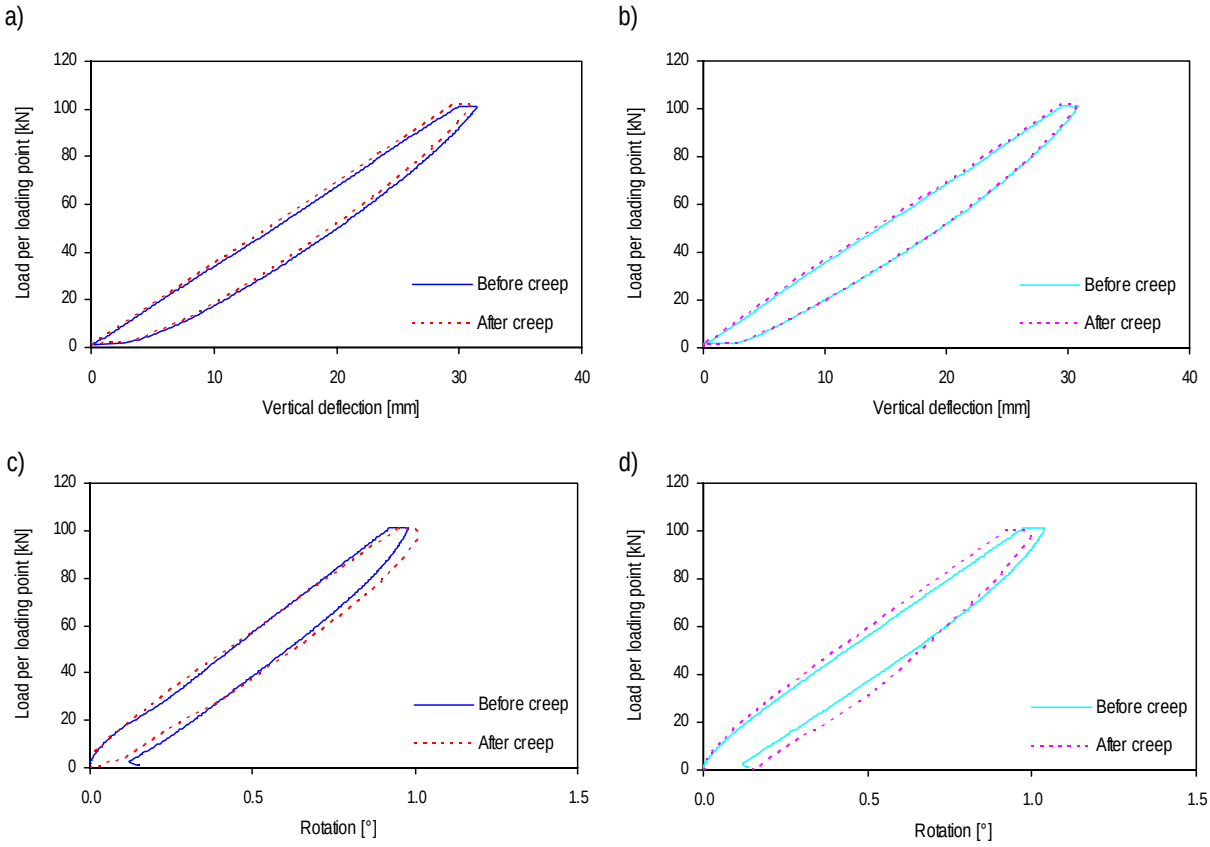

Figure 85 Load-deflection results at (a) North loading-section, (b) South loading-section; Load-rotation results at mid-support (c) North span (span 1), (d) South span (span 2) for beam PH2 before and after creep experiment

4.4 Discussion

As expected, the deflections of the bonded beams and the rotations at mid-support were between the values of the simple beams and continuous beams, as it can be seen in Figures 86 and 87 and in the Table 18. The bonded beams showed a tri-linear behavior with a first stiffness loss due to the bilinear behavior of the adhesive and a second loss due to the onset of buckling deformations in the compressed regions. Beam PH3 showed an additional stiffness loss due to the failure of the bonded joint. Therefore, the bonded beams exhibited system ductility with a ductile behavior in the first part (ductile joint) and a deformability in the second part (local buckling) (de Castro 2005 b). The additional stiffness loss of beam PH3 can be considered as an additional pseudo-ductility due to the hyperstatic system configuration.

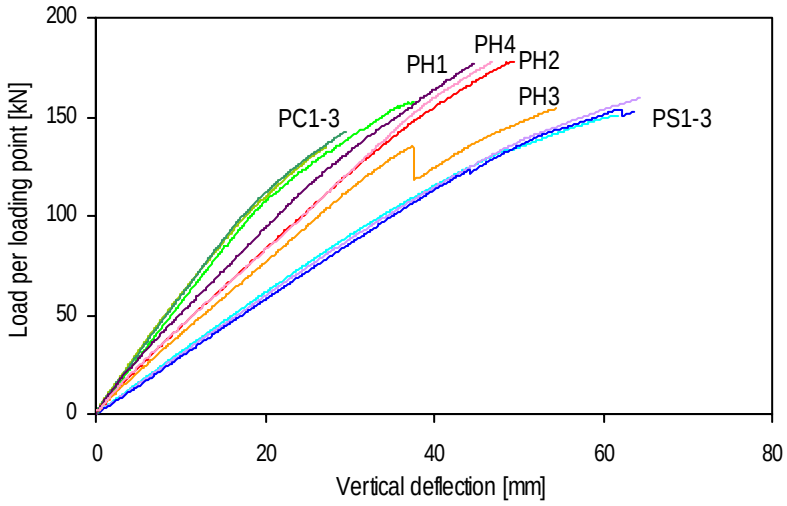

Figure 86 Load-deflection results at the North loading section for beams PS1-3, PC1-3 and PH1-4

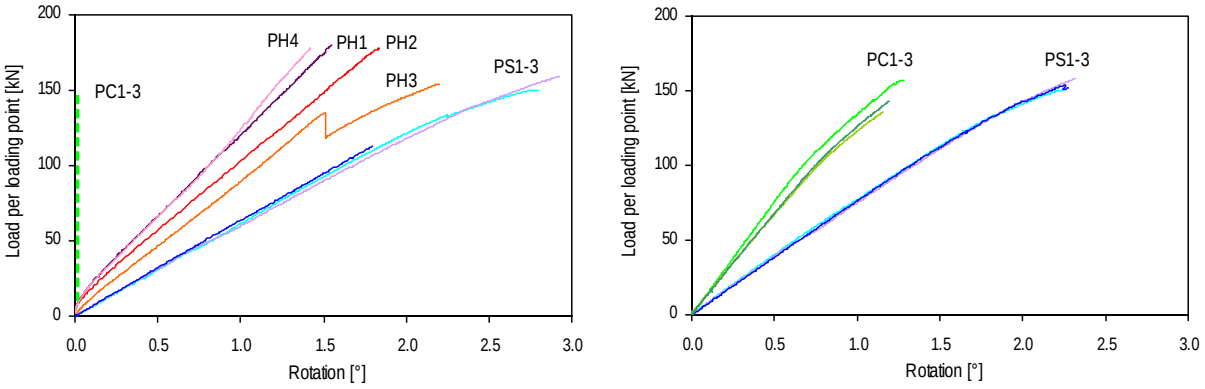

Figure 87 Load-rotation results at (a) the mid-supports for beams PS1-3, PC1-3 and PH1-4, (b) the edge supports for beams PS1-3and PC1-3

Table 18 Overview experimental beams PS1-3, PC1-3 and PH1-4 and results at failure

Beam	Q_u [kN])	M^+_u [kNm]	M^-_u [kNm]	$\theta_{M,u}$ [°]	$\theta_{E,u}$ [°]	$w_{F,u}$ [mm]	$w_{F,u}$ /L [-]	Failure location
PS1-3	155±5	124±4	0	2.85±0.07	2.30±0.08	66±3	1/55	Loading point
PC1-3	146±11	63±5	81±6	0.00	1.21±0.06	32±6	1/116	Mid-support
PH1	180	99	67	1.55	-	45	1/80	Loading point
PH2	178	107	53	1.84	-	50	1/73	Loading point
PH3 [1]	135	84	36	1.52	-	38	1/65	Mid-support joint
PH3[2]	154	111	-	2.21		55	1/95	Loading point
PH4	178	98	66	1.42	-	47	1/77	Loading point

[1] at the joint failure
[2] at the span failure

Table 19 Comparison of beams with adhesive joints and simple/continuous beams

Beam	Q_u		$\theta_{M,u}$	$w_{F,u}$	
	PS1-3	PC1-3	PS1-3	PS1-3	PC1-3
PH1 (l=200 mm)	+16%	+23%	-46%	-32%	+42%
PH2 (l=200 mm)	+15%	+22%	-35%	-24%	+58%
PH3 (l=100 mm)	-1%	+5%	-22%	-17%	+74%
PH4 (l=300 mm)	+15%	+22%	-50%	-29%	+48%
Average (w/o PH3)	15.3±0.6%	22.3±0.6%	-28.3±4.0%	-28.3±4.0%	49.3±8.1%

Figure 88(c) shows the bending moment diagrams of all beams at 50 kN per jack. The moments were calculated from the measured support reactions (Table 20). Compared to the simple and continuous beams, the flexible adhesive joints led to a better distribution of the moments and support reactions. The maximum moments and the support reactions at the mid-support were reduced compared to the continuous beam, which failed at this location. On the other hand, the sections below the jacks were less loaded due to the partial fixation at the mid-support so that the loads could be increased beyond the failure loads of the simple beams. As listed in Table 19, the ultimate failure loads were increased by 15% compared to the simple beams and 22 % compared to the continuous beams (average values without PH3). In the beams with 200 and 300 mm overlaps, the failures occurred in the spans below the hydraulic jacks. The adhesively bonded joints remained undamaged. Only in beam PH3 with the shortest overlaps of 2x100 mm did premature failure occur in the adhesive joint. This beam, however, showed a redundant behavior due to the hyperstatic system and the load could be increased again by 14% up to ultimate failure.

The demonstration of the full potential of the proposed new concept by means of the experiments performed was partially affected by two reasons. First, the local buckling failures of the compressed flanges or webs in the loading or support sections were expected, but at higher loads. Failure in compressed flanges or webs at load introduction points is the normally observed failure mode of pultruded thin-walled sections (Barbero et al. 1991). However, the maximum stresses at failure were only approximately -153 N/mm^2 (Table 10) and, therefore, far below the -240 N/mm^2 indicated in the design manual of the pultruder. The short overlap of the combined fiber mats, 2x30 mm from the section edges,

proved to be a week area in the beams. As a result of the experiments, the fiber architecture was improved by the pultruder. Second, the adhesive available behaved not exactly as wished. An ideal adhesive should be stiffer at the beginning (comparable to an epoxy adhesive) and then should behave more plastically. With the improved beams and with a ductile adhesive, the enhanced load-carrying behavior should be much more pronounced, compared to the single and continuous beams.

Table 20 Support reactions, bending moment ratio and null bending moment location (50 kN)

Beam	R_E/Q	R_M/Q	M^-/M^+	x/L
PS1-3	0.33	2×0.67	-	-
PC1-3	0.16	2×0.84	1.63	0.21
PH1	0.23	2×0.77	0.67	0.13
PH2	0.25	2×0.75	0.50	0.11
PH3 [1]	0.26	2×0.74	0.42	0.10
PH3 [2]	0.30	2×0.70	-	-
PH4	0.23	2×0.77	0.67	0.13

[1] at the joint failure
[2] at the span failure

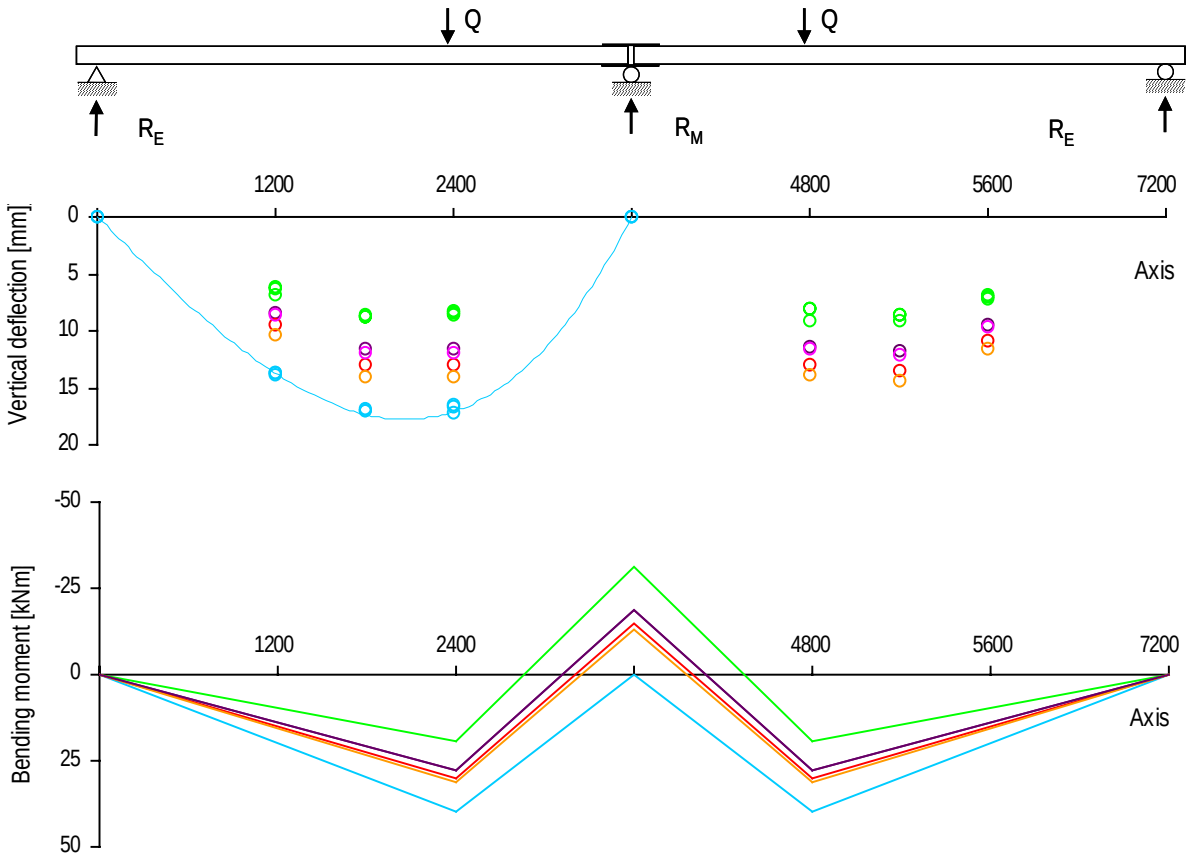

Figure 88 (a) Support reactions; (b) Deformation; (c) Bending moment diagram (Q=50 kN) for beams PS1-3, PC1-3 and PH1-4

5 Conclusions

Quasi-static and creep experiments on brittle GFRP beams connected with flexible adhesive joints were performed and were compared to quasi-static experiments on simple and continuous beams. The adhesively connected beams showed a system ductility with the following characteristics:

- The flexible joints with highly nonlinear adhesives provided a favorable distribution of the internal (bending moments) and external forces (support forces) in the hyperstatic system and thereby increased the load-carrying capacity and the structural safety when compared to the simple (15-16%) and continuous (22-23%) beams.
- In the case of adhesive joint failure, a structural collapse could be prevented due to the redundancy of the hyperstatic system. After joint failure, the load could be increased by 14% up to the ultimate failure load.
- Due to the stiffness-governing design of the GFRP beams, the stresses in flexible adhesive joints were small and creep deformations in the joints could be controlled.
- The results of this research confirmed the feasibility of the proposed concept for structures composed of brittle FRP components. The concept includes the use of redundant structural systems and ductile or flexible adhesive joints to provide system ductility that compensates for the lacking material ductility inherent to FRP structures.

6 Acknowledgements

The author wishes to acknowledge the support of the Swiss Innovation Promotion Agency CTI (Contract N° 4676.1), Fiberline Composites A/S, Denmark (supplier of the pultruded profiles) and Sika AG, Zurich, Switzerland (supplier of the adhesives). Special thanks to Mr Venetz of SIKA AG for his assistance with the bonded joint manufacture.

7 Appendix

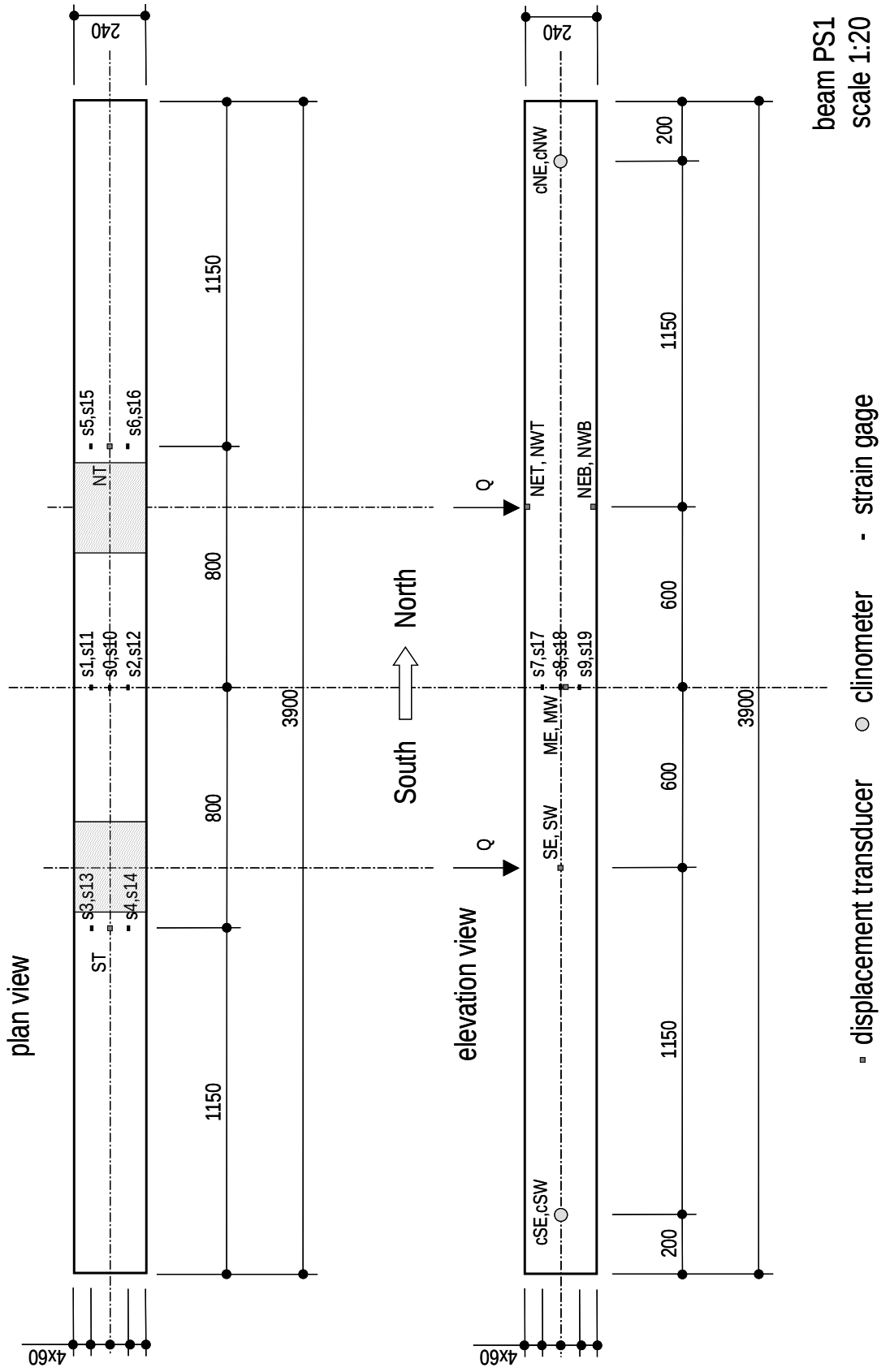

Figure 89 Arrangement of displacement transducers, clinometers and strain gages in beam PS1

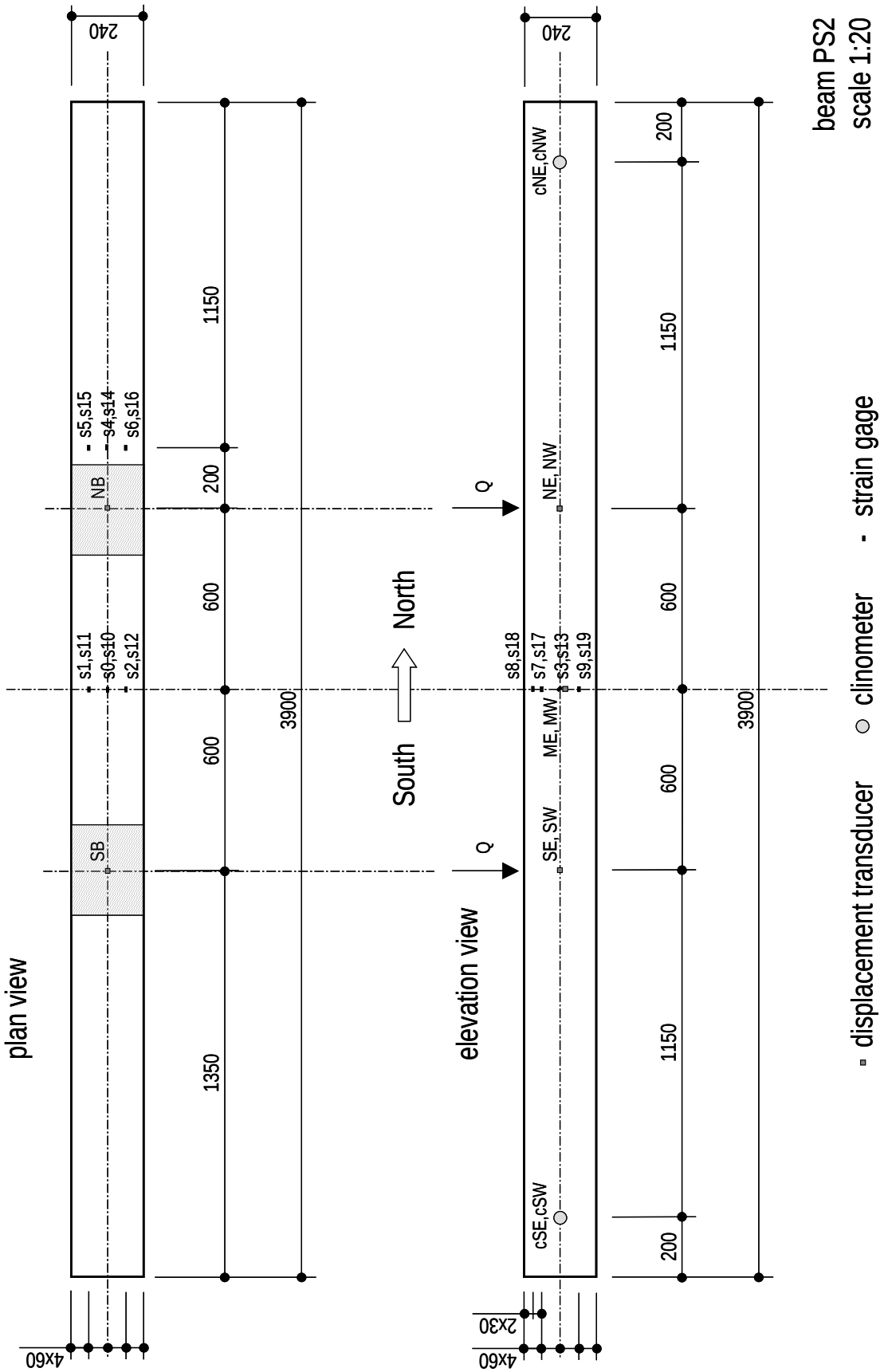

Figure 90 Arrangement of displacement transducers, clinometers and strain gages in beam PS2

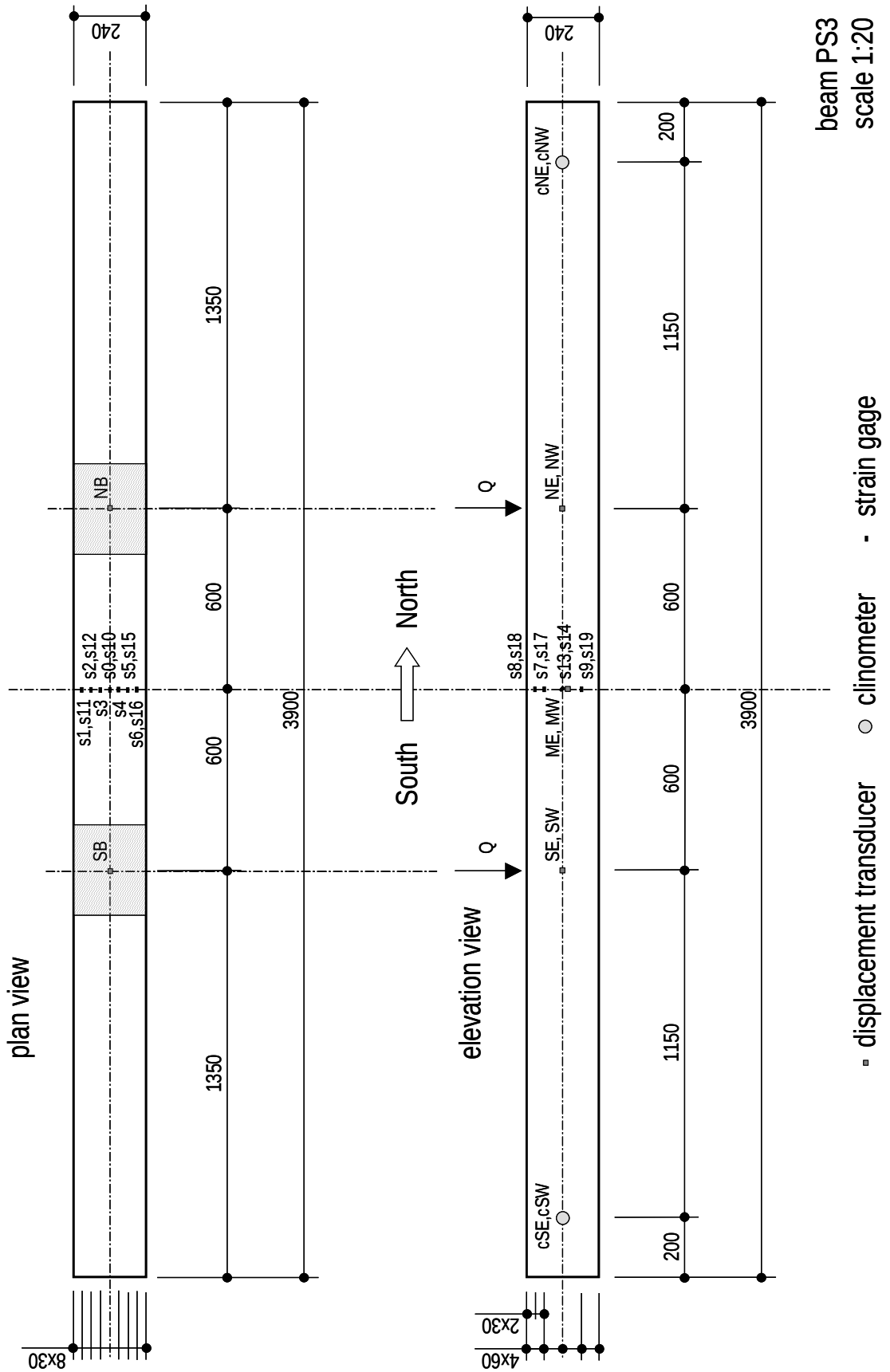

Figure 91 Arrangement of displacement transducers, clinometers and strain gages in beam PS3

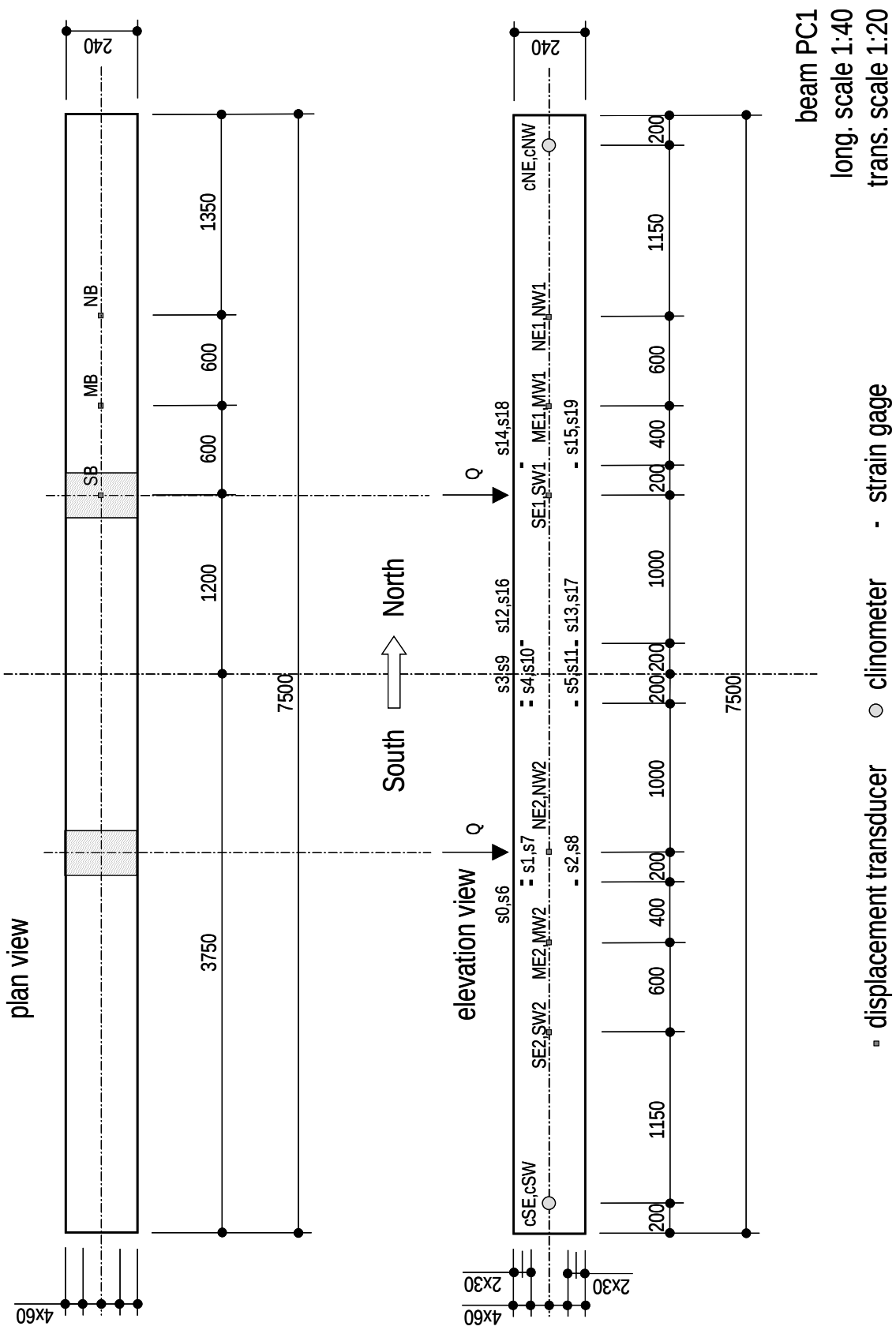

Figure 92 Arrangement of displacement transducers, clinometers and strain gages in beam PC1

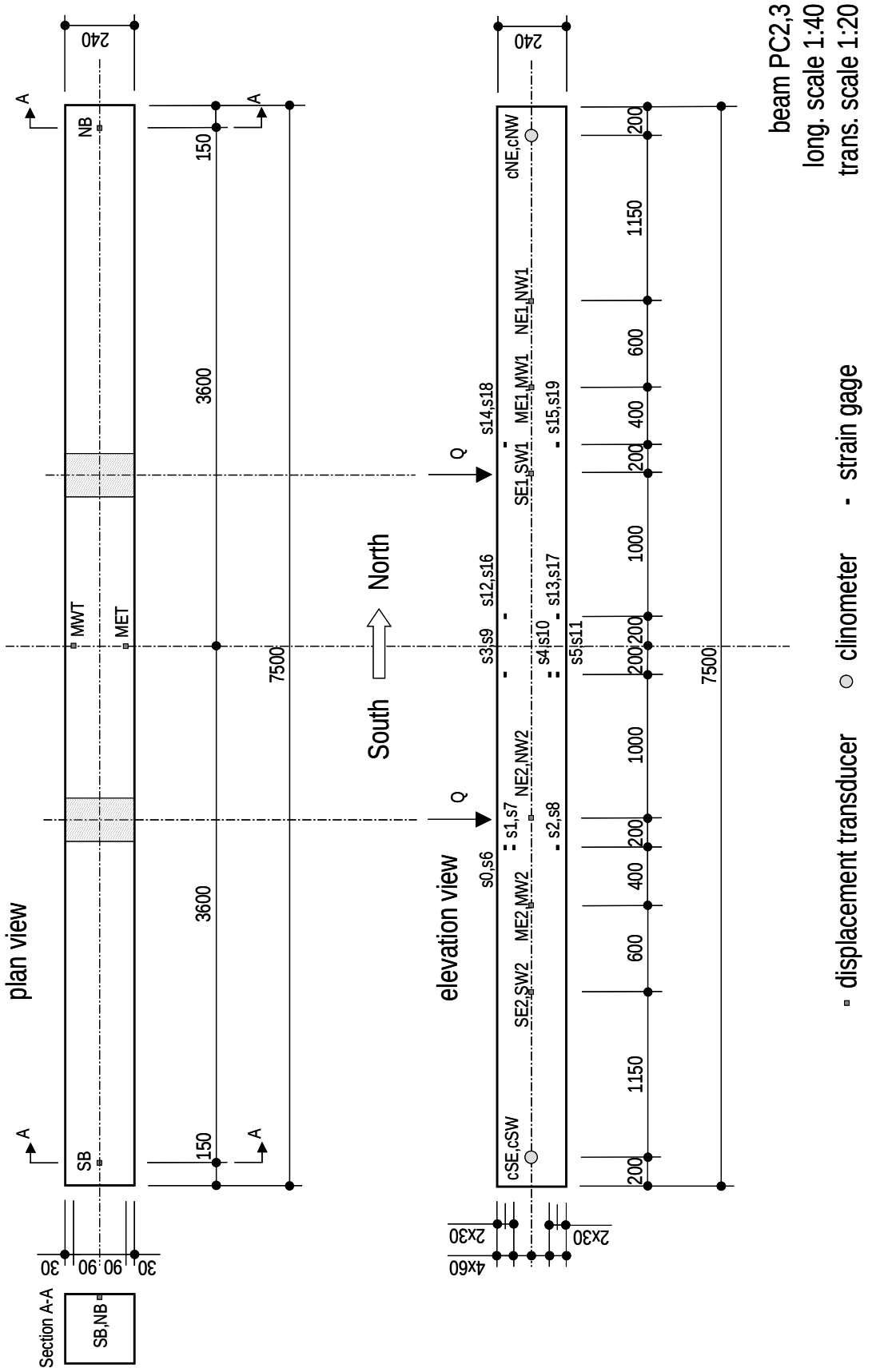

Figure 93 Arrangement of displacement transducers, clinometers and strain gages in beams PC2 and PC3

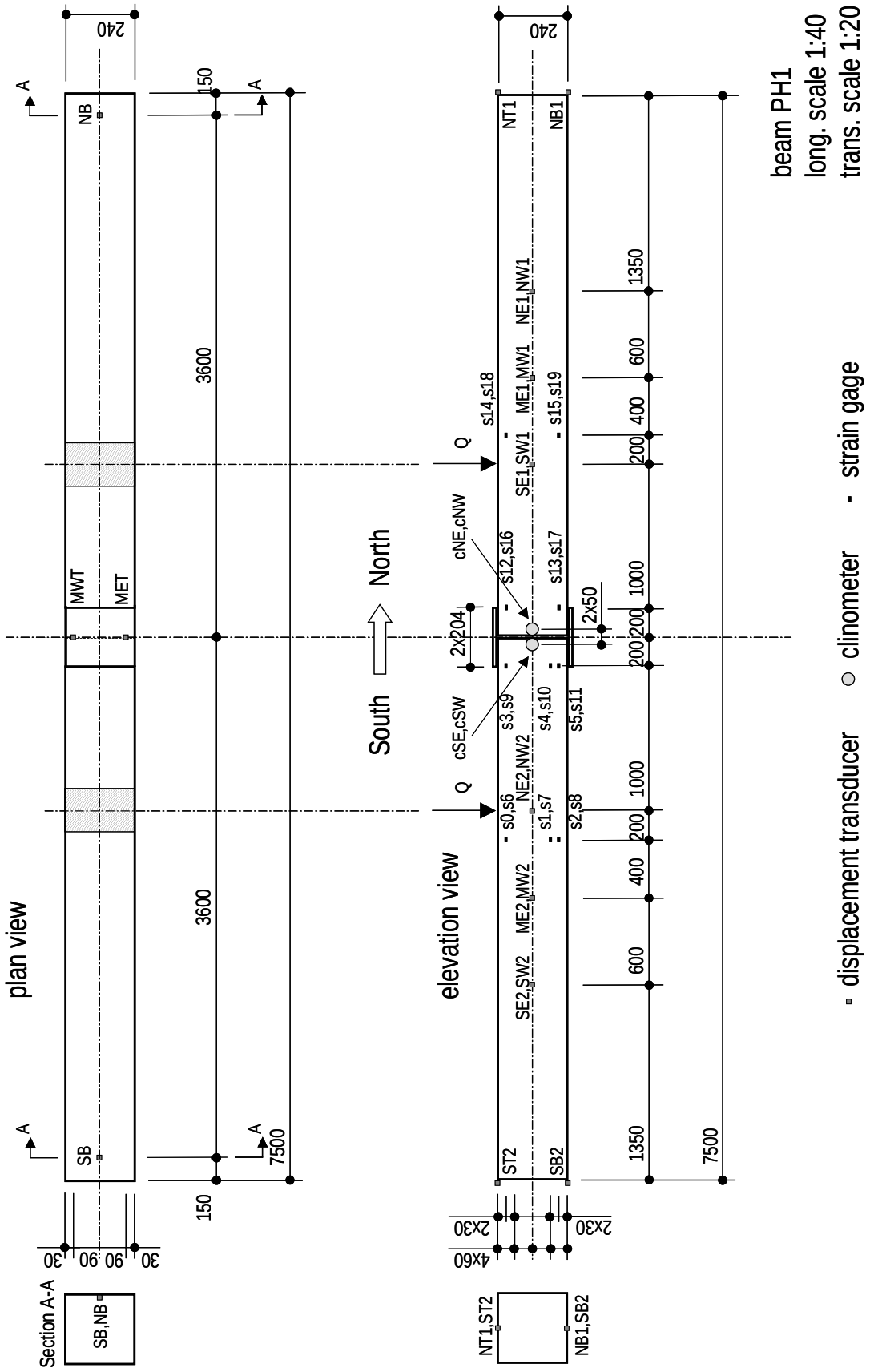

Figure 94 Arrangement of displacement transducers, clinometers and strain gages in beam PH1

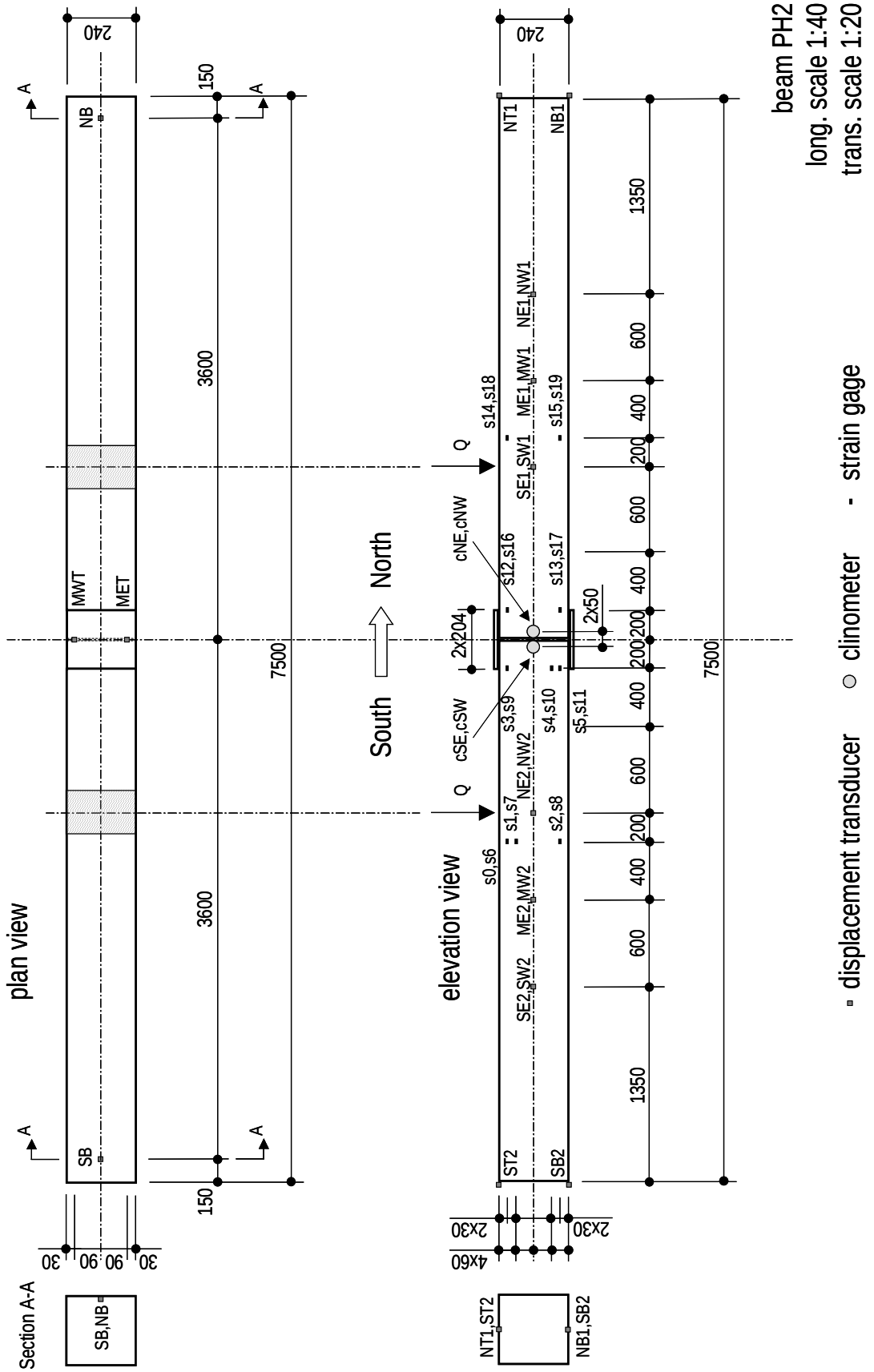

Figure 95 Arrangement of displacement transducers, clinometers and strain gages in beam PH2

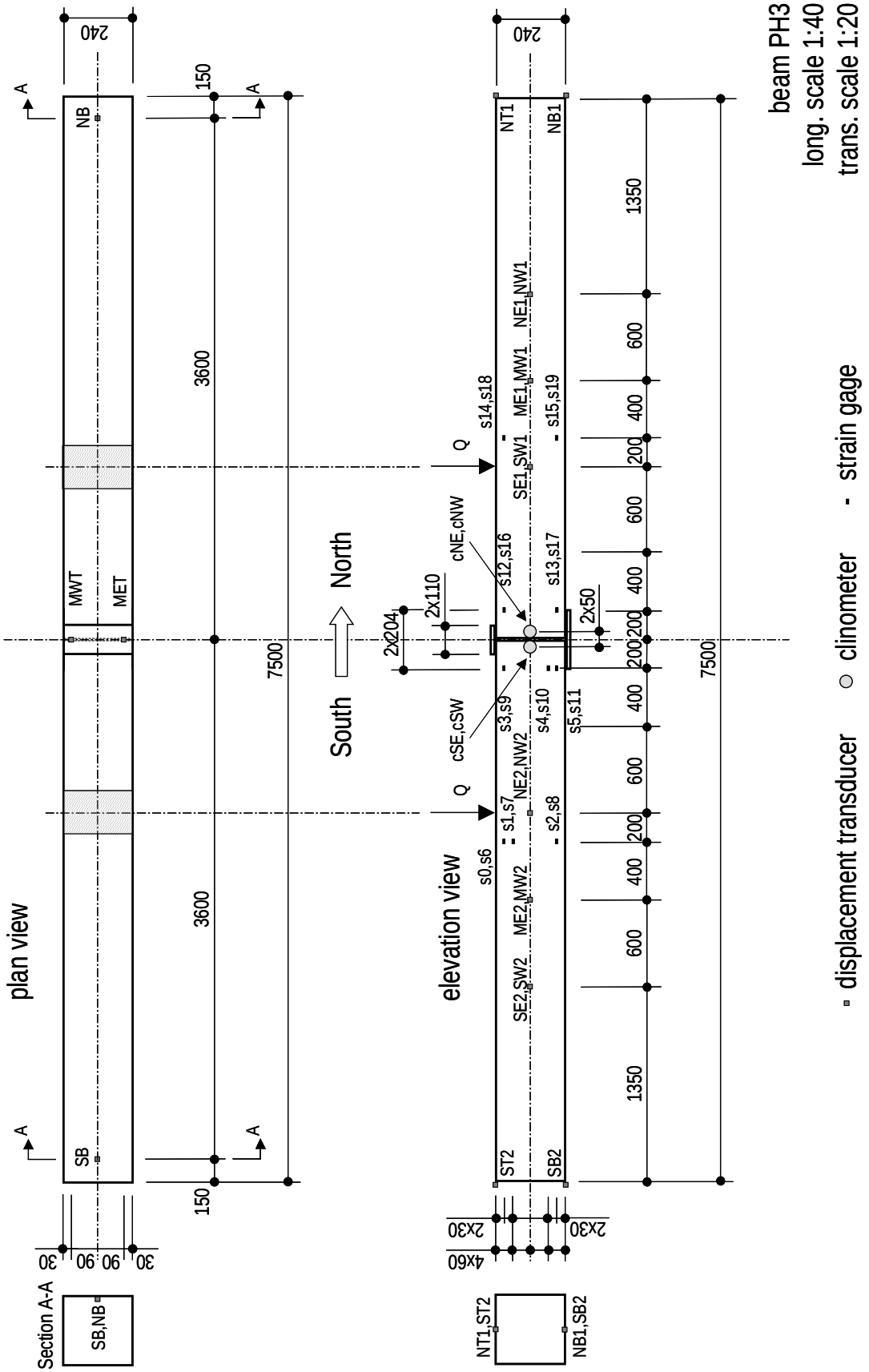

Figure 96 Arrangement of displacement transducers, clinometers and strain gages in beam PH3

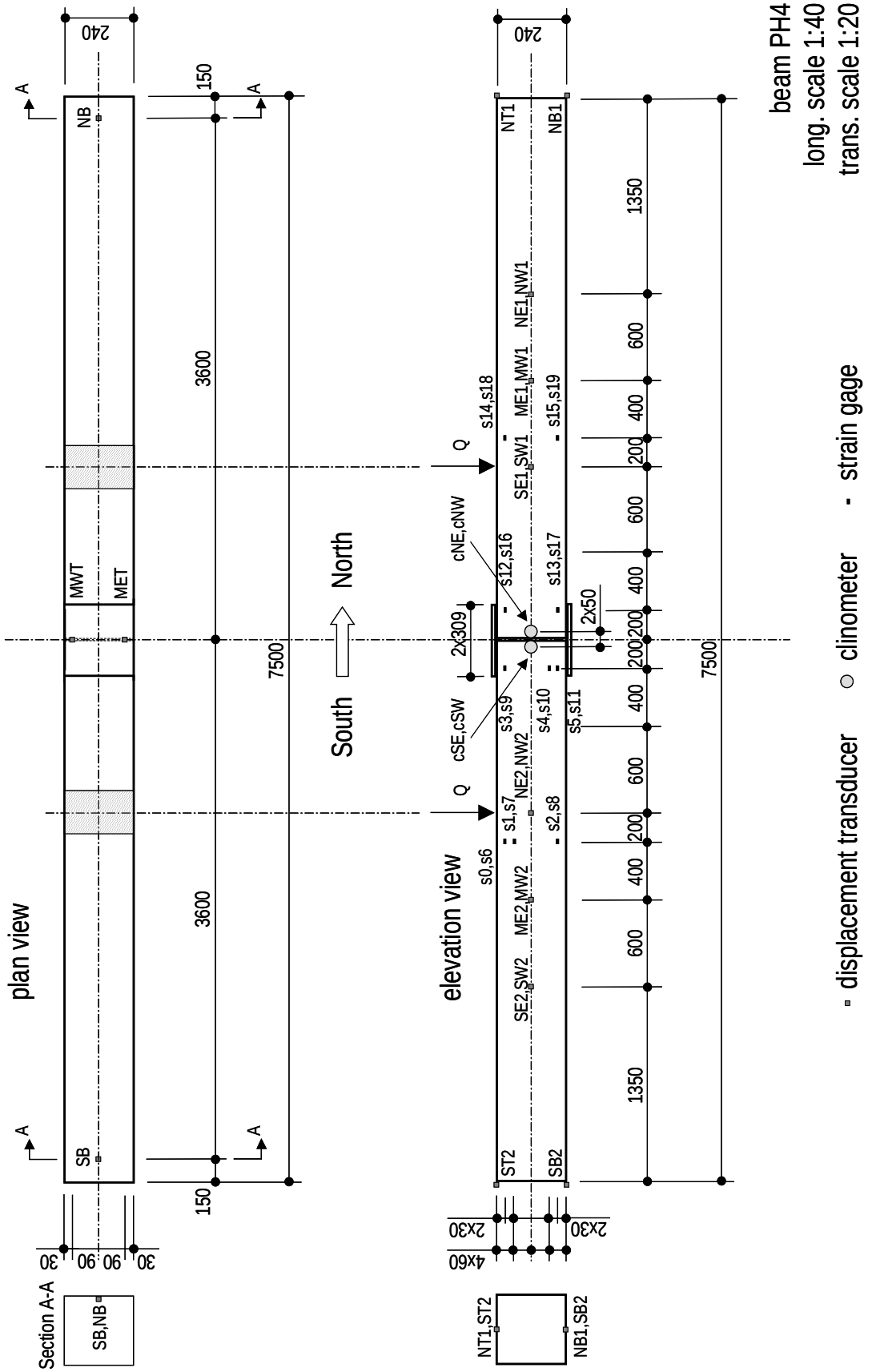

Figure 97 Arrangement of displacement transducers, clinometers and strain gages in beam PH4

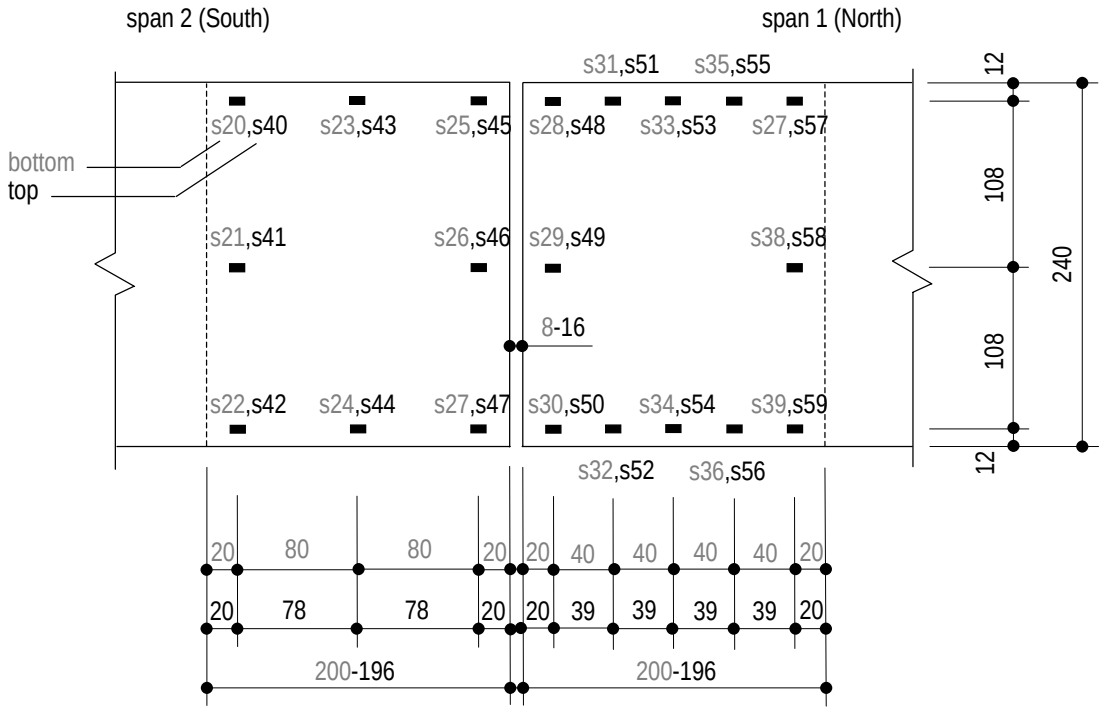

Figure 98 Gage locations in beam PH1

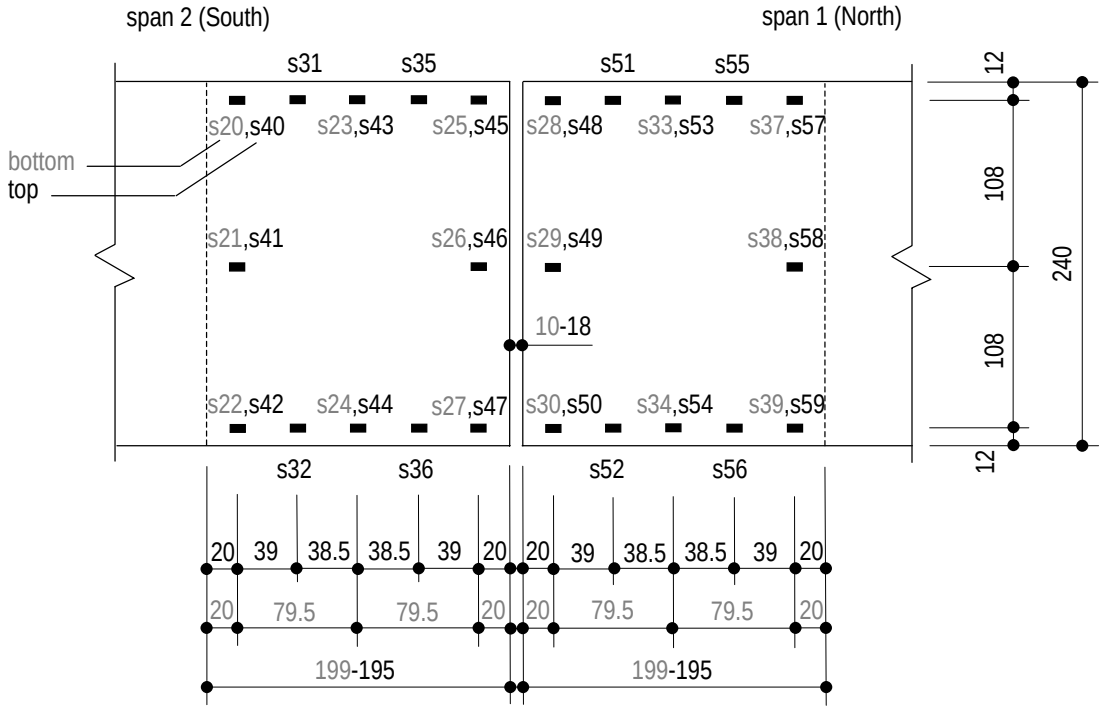

Figure 99 Gage locations in beam PH2

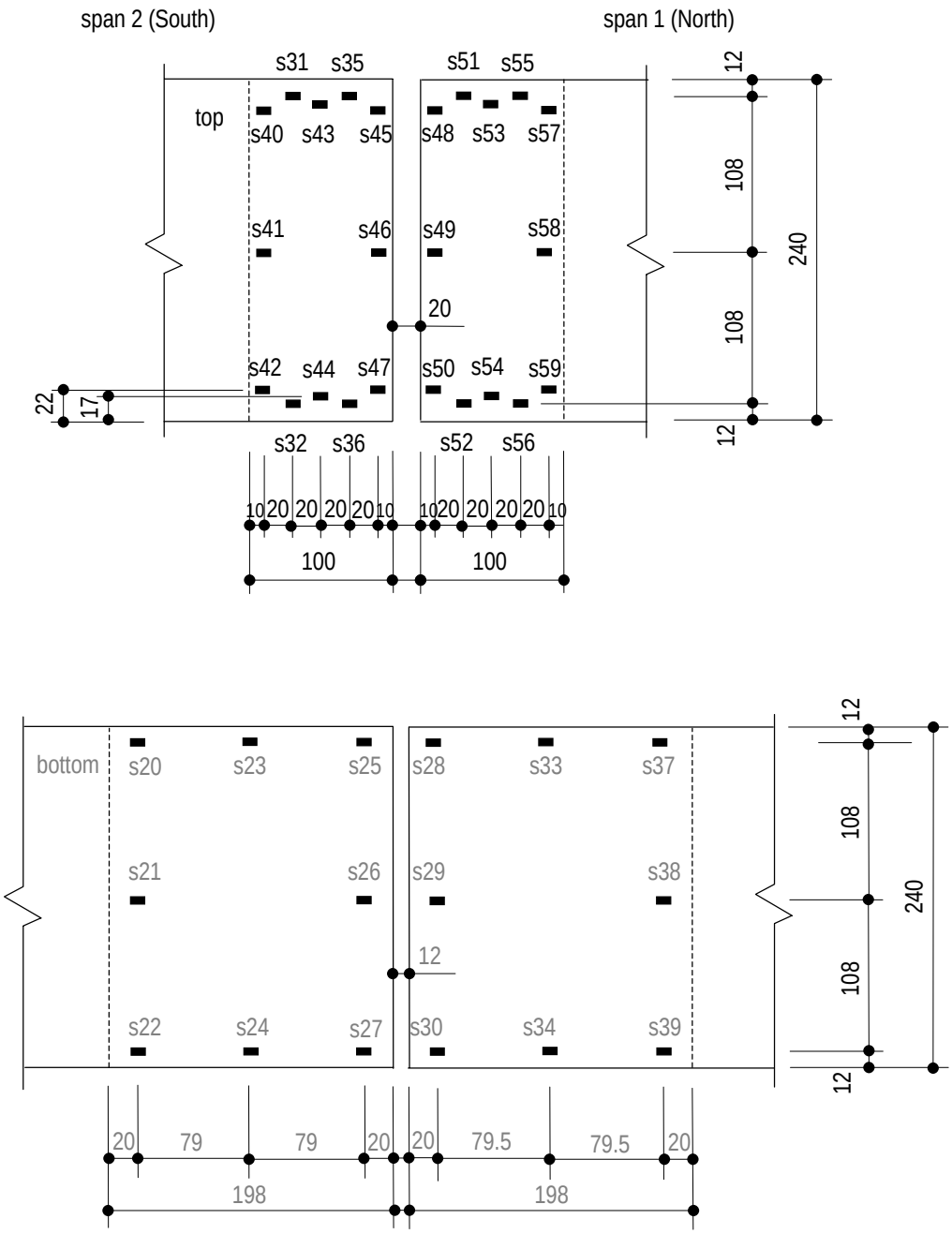

Figure 100 Gage locations in beam PH3

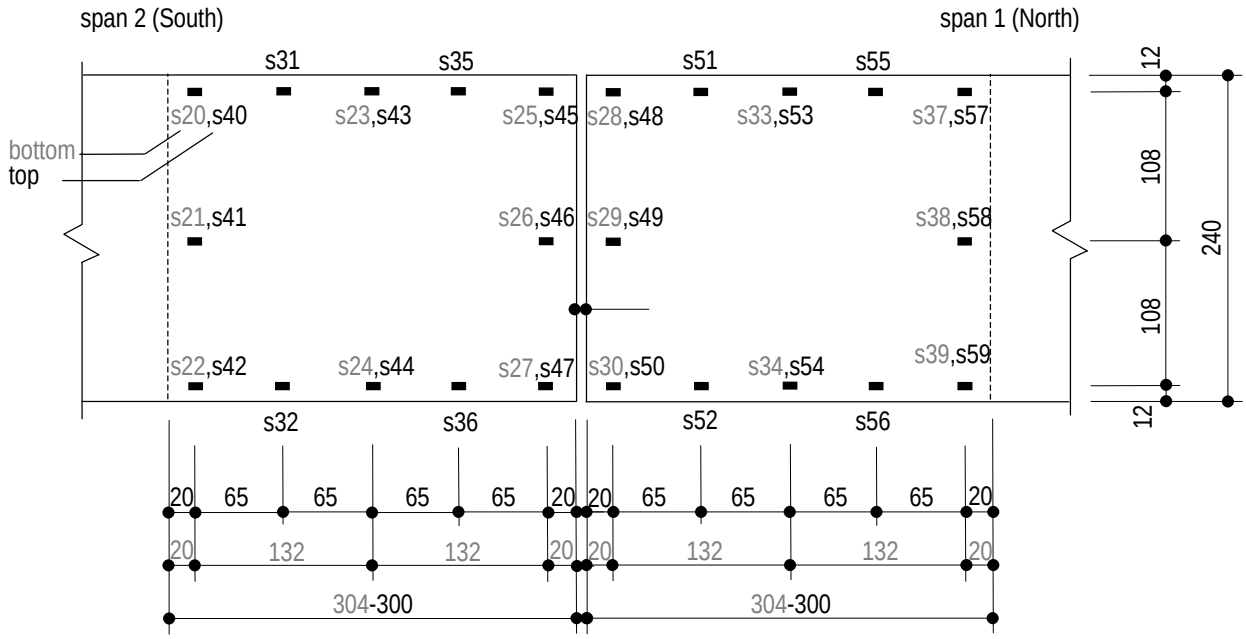

Figure 101 Gage locations in beam PH4

8 List of Figures

9 List of Tables

10 References

ANON (2003), *Fiberline Design Manual*, Internet -http:/www.fiberline.com/gb/home/index.asp, July 6, 2004.

ASHBY M.F. (1991), Materials and Shapes, *Acta Metallurgica Materialia*, Vol.39, No. 6, pp 1025-1039.

ASTM D 638-96 (1996), Standard Test Method for Tensile Properties of Plastics, *Annual Book of ASTM Standards*, United States of America.

BARBERO E.J., FU S.H., RAFTOYIANNIS I. (1991), Ultimate Bending Strength of Composite Beams, *Journal of Materials in Civil Engineering*, Vol. 3, No. 4, pp 292-306.

DHARMARAJAN S., MCCUTHEN JR.H. (1973), Shear Coefficients for Orthotropic Beams, *Journal of Composite Materials*, Vol. 7, pp 530-535.

DE CASTRO J. (2005 a), *Experiments on Epoxy, Polyurethane and Acrylic Adhesives*, Technical Report CCLab2000.1b/1, CCLab-EPFL, Lausanne, Switzerland.

DE CASTRO J. (2005 b), *Experiments on Double-lap Joints with Epoxy, Polyurethane and Acrylic Adhesives*, Technical Report CCLab2000.1b/2, CCLab-EPFL, Lausanne, Switzerland.

EN ISO 527-2 (1996), Determination of Tensile Properties - Part 2: Test Conditions for Moulding and Extrusion Plastics, European Standard, Brussels, Belgium.

EN ISO 11003-1 (1996), Determination of Shear Behaviour of Structural Adhesives - Part 1: Torsion test method using butt-bonded hollow cylinders, European Standard, Brussels, Belgium.

EUREKA Project EU716 (1998), *Quality Assurance in Adhesive Technology*, Abington Publishing, Cambridge, United Kingdom.

FREY F. (1994), *Analyse des structures et milieux continus : mécanique des structures*, Traité de Génie Civil Vol. 2, PPUR, Lausanne, Switzerland.

FREY F. (1998), *Analyse des structures et milieux continus : mécanique des solides*, Traité de Génie Civil Vol. 3, PPUR, Lausanne, Switzerland.

GERE J.M., TIMOSHENKO S.P. (1984), Deflection of Beams, *Mechanics of Materials*, 2nd edition, Brooks/Cole Engineering Division, Monterey, California, pp 351-428.

KELLER T. (2003), *Use of Fibre Reinforced Polymers in Bridge Construction*, Structural Engineering Documents No. 7, International Association for Bridge and Structural Engineering, Zürich, Switzerland, 131 pages.

KELLER T., DE CASTRO J., SCHOLLMAYER M. (2004), Adhesively Bonded and Translucent Glass Fiber Reinforced Polymer Sandwich Girders, *Journal of Composites for Constructions*, Vol. 8, No. 5, pp 461-470.

MOTTRAM J.T. (1991), Structural Properties of a Pultruded E-Glass Fiber-Reinforced Polymeric I-Beam, *Composite Structures Vol. 6*, I.H. Marshall ed., Elsevier Applied Science, London and New York, pp 1-28.

NAGARAJ V., GANGARAO V.S. (1997), *Static* Behavior of Pultruded GFRP Beams, *Journal of Composites for Construction*, Vol. 1, No. 3, pp.120-129.

OMIDVAR B. (1998), Shear Coefficient in Orthotropic Thin-Walled Composite Beams, *Journal of Composite for Construction*, Vol. 2, No. 1, pp 46-55.

TIRELLI T. (2003), *Static and Fatigue Behavior of Pultruded GFRP Laminates*, Technical Report CCLab2000.1c/2, CCLab-EPFL, Lausanne, Switzerland.

SCHMID M., KIESELBACH R. (2001), Adhesive Bonding - a Challenge for Design, *J. of the Engineering Integrity Society*, 10, 24-33.

SIEBRECHT J, VALLEE T. (2001), *Shear Test on Bonded Double Lap FRP-Joints*, Diploma dissertation, Chapter 7, CCLab-EPFL, Lausanne, Switzerland.

YOUNG W.C. (1989), *Roark's Formulas for Stress and Strain*, 6th edition , Seventh ed., New York: McGraw-Hill, 852 pages.

ZUREICK A., KAHN L.F., BANDY B.J. (1994), Test on deep I-Shapes Pultruded Beams, *Composites Institute's 49th Annual* Conference, The Society of the Plastic Industry, New York, Session 8-C.

ZUREICK A., SHIH B. (1998), Local Buckling of Fiber-Reinforced Polymeric Structural Members under Linearly-Varing Edge loading – Part 1: Theoretical Formulation, *Composite Structures*, Vol. 41, No. 1, pp 79-86.